

DEVELOPMENT OF NICKEL SUBSTITUTED MANGANESE
COBALT SULFIDE / REDUCED GRAPHENE OXIDE AS A
SYNERGISTIC COMPOSITE CATALYST FOR OXYGEN
EVOLUTION REACTION

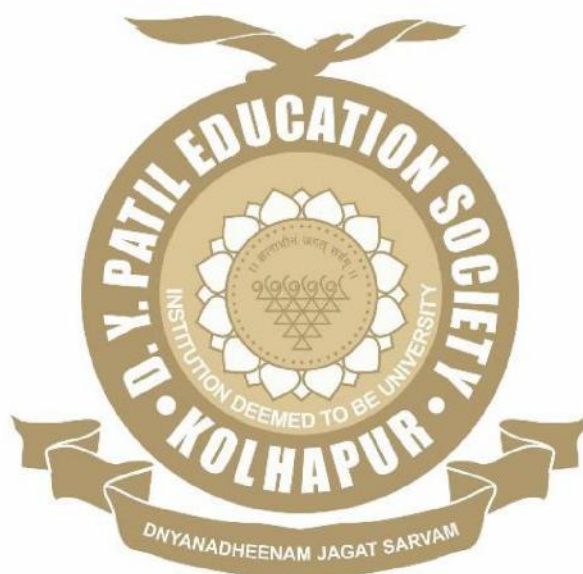
By

Ms. SHITAL B. KALE

Under the Supervision of

PROF. C. D. LOKHANDE

Thesis Submitted to



For the Degree of

Doctor of Philosophy

2021

**DEVELOPMENT OF NICKEL SUBSTITUTED
MANGANESE COBALT SULFIDE/REDUCED GRAPHENE
OXIDE AS A SYNERGISTIC COMPOSITE CATALYST FOR
OXYGEN EVOLUTION REACTION**

A Thesis Submitted to
**D. Y. PATIL EDUCATION SOCIETY
(DEEMED TO BE UNIVERSITY)**

For the Degree of
DOCTOR OF PHILOSOPHY
In
PHYSICS

By
Ms. SHITAL B. KALE
M. Sc.

Under the Supervision of
Prof. C. D. LOKHANDE
M. Sc., Ph. D.

CENTRE FOR INTERDISCIPLINARY RESEARCH,
D. Y. PATIL EDUCATION SOCIETY
(DEEMED TO BE UNIVERSITY),
KOLHAPUR- 416 006.

2021

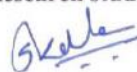
DECLARATION

I hereby declare that the work containing in this thesis has not been previously submitted to meet requirements for an award at this or any other higher education institute in India or any other country. To the best of my knowledge and belief, the thesis contains no material previously published or written by another person except where due reference is made. Further I declare that I have not violated any of the provisions under Copyright and Piracy/ Cyber/ IPR Act amended from time to time.

Place: Kolhapur

Research student

Date: 12/03/2021



Ms. Shital Bhaskar Kale

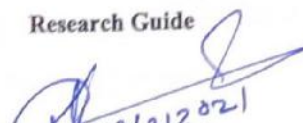
CERTIFICATE OF GUIDE

This is to certify that the present thesis which is being submitted herewith for the award of doctor of philosophy in Physics under the faculty of center for interdisciplinary research (CIR) of D. Y. Patil education society, Kolhapur is the result of original research work completed by Miss Shital Bhaskar Kale under my supervision and guidance and the best of my knowledge and belief, the work embodied in this thesis has not formed earlier the basis for the award of any degree or similar title of this or any other University or examining body.

Place: Kolhapur

Research Guide

Date: 12/03/2021


Prof. C. D. Lokhande

ACKNOWLEDGMENT

This was a beautiful journey, a journey of expanding the boundaries of knowledge, a journey of finding your strengths and weaknesses, a journey of becoming mentally and emotionally strong. It became more beautiful and interesting because of the people I met along the way. I would like to take this opportunity to acknowledge those fascinating people.

*Foremost, I would express my deepest gratitude to my genius mentor, **Prof. C. D. Lokhande**, Research Director, D. Y. Patil Education Society, for his guidance, support and many fruitful discussions during the course of this work. I am always amazed by his enthusiasm for science and how effectively he has shaped the young minds of two generations. I am very thankful to him for choosing me as his PhD student and I feel very fortunate to be part of CDL group.*

*I am very thankful to **Prof. J. H. Kim**, Dean, College of engineering, Chonnam National University, South Korea, for being my host professor during my Overseas Visiting Doctoral fellowship tenure and allowing me to work in his renowned laboratory.*

*I am thankful to **Dr. V. V. Bhosale**, Registrar, D. Y. Patil Education Society as well as **Dr. Gulbake**, **Mrs. Namrata**, **Mr. Ramdas** and other staff of the center for interdisciplinary research (CIR) and D. Y. Patil Education Society for co-operation in many ways during my PhD.*

*A special thanks to **Dr. J. L. Gunjkar** for the leisurely chats we had related to research as well as different topics. I also thank **Dr. U. M. Patil** and **Dr. D. P. Dubal** for valuable discussions regarding research. All of you and other CDL group members always inspire me to work hard.*

*Big thanks to the past and present members of CIR. Specially, **Dr. Jagruti** (thank you for making my days memorable at Kolhapur), **Satyajeet, Supriya, Rohini, Dhanaji, Akash, Shrikant, Shivaji, Vikas, Trupti, Swapnali, Navnath** and **Kasturi**.*

*I am thankful to the **science and engineering research board (SERB)**, Government of India for awarding me Overseas Visiting Doctoral Fellowship to pursue my research from an overseas university. I am grateful to **Pooja di, Vaibhav sir, Rahul sir, Komal madam** for helping me to get settle in Gwangju and making me feel homely in foreign. I am thankful to **Vijay, Dong-Min, Dr. Kuldeep, In-Jae, Byeong Hoon, Dr. Pravin**, and all other members of Photonic and Electronic Thin Film Laboratory, Chonnam National University.*

*To the amazing guys **Aman, Lakshya, Aqsa, Dooti, Dr. Aniket**, and **Umesh** thank you for making my expat life happening. To Aman, thank you for being my friend. To my dear friends **Hardik** and **Neha** thank you for always being there for me in any situation and supporting and helping me.*

*Special thanks are reserved for my uncle, **Dr. S. S. Kale**, whose support, encouragement and love have been a constant source of stimulation throughout my academic career. To my parents and other family members for their love.*

~Shital

Place: Kolhapur

LIST OF PUBLICATIONS AND CONFERENCES

PUBLICATIONS:

1. **Shital B. Kale**, Abhishek C. Lokhande, Rahul B. Pujari, Chandrakant D. Lokhande, "Cobalt sulfide thin films for electrocatalytic oxygen evolution reaction and supercapacitor applications", Journal of Colloid and Interface Science, 532 (2018), 491- 499 (*I. F.* 7.49).
2. **Shital B. Kale**, Abhishek C. Lokhande, Rahul B. Pujari, Chandrakant D. Lokhande, "Effect of pretreatment on catalytic activity of cobalt sulfide thin film for oxygen evolution reaction", Materials Letters, 228 (2018), 418-420 (*I. F.* 3.2).
3. **Shital B. Kale**, Vaibhav C. Lokhande, Supriya J. Marje, Umakant M. Patil, Jin Hyeok Kim, Chandrakant D. Lokhande, "Chemically deposited Co_3S_4 thin film: morphology dependant electrocatalytic oxygen evolution reaction", Applied Physics A, 126 (2020), Article number 206 (*I. F.* 1.81).
4. **Shital B. Kale**, Pravin T. Babar, Jin-Hyeok Kim, Chandrakant D. Lokhande, "Synthesis of one dimensional Cu_2S nanorods using a self-grown sacrificial template for the electrocatalytic oxygen evolution reaction (OER)", New Journal of Chemistry, 44 (2020), 8771-8777 (*I. F.* 3.28).
5. **Shital B. Kale**, Aman Bhardwaj, Vaibhav C. Lokhande, Dong-Min Lee, Soon-Hyung Kang, Jin-Hyeok Kim, Chandrakant D. Lokhande, "Amorphous cobalt-manganese sulfide electrode for efficient water oxidation: Meeting the fundamental requirements of an electrocatalyst", Chemical Engineering Journal, 405 (2021), Article number 126993 (*I. F.* 10.56).
6. Rahul B. Pujari, Abhishek C. Lokhande, Trupti T. Ghogre, **Shital B. Kale**, Chandrakant D. Lokhande, "Hydrothermally synthesized monoclinic Yb_2S_3 thin films for supercapacitive application", Journal of Materials Science: Materials in Electronics, 29 (2018), 14116-14121 (*I. F.* 2.22).
7. Pranav K. Katkar, Supriya J. Marje, **Shital B. Kale**, Abhishek C. Lokhande, Chandrakant D. Lokhande, Umakant M. Patil, "Synthesis of hydrous cobalt phosphate electrocatalysts by a facile hydrothermal method for enhanced oxygen evolution reaction: effect of urea variation", Crystal Engineering Communication, 21 (2019), 884-893 (*I. F.* 3.12).
8. Supriya J. Marje, Pranav K. Katkar, **Shital B. Kale**, Abhishek C. Lokhande, Chandrakant D. Lokhande, Umakant M. Patil, "Effect of phosphate variation on morphology and electrocatalytic activity (OER) of hydrous nickel

pyrophosphate thin films”, Journal of Alloys and Compounds, 779 (2019), 49-58 (*I. F. 4.65*).

9. Dhanaji B. Malavckar, Vaibhav C. Lokhande, Vikas J. Mane, **Shital B. Kale**, Ravindra N. Bulakhe, Umakant M. Patil, Insik In, Chandrakant D. Lokhande, “Facile synthesis of layered reduced graphene oxide-copper sulfide (rGO-CuS) hybrid electrode for all solid-state symmetric supercapacitor”, Journal of Solid State Electrochemistry, 24 (2020), 2963-2974 (*I. F. 2.64*).
10. Rahul B. Pujari, Abhishek C. Lokhande, Abhijeet R. Shelke, **Shital B. Kale**, Dong-W Lee, Chandrakant D. Lokhande, “MnS₂/carbon nanotube electrode for improved supercapacitor performance”, Solid State Sciences, 111 (2021), Article number 106449 (*I. F. 2.43*).
11. Dhanaji B. Malavekar, **Shital B. Kale**, Vaibhav C. Lokhande, Umakant M. Patil, Jin-Hyeok Kim, Chandrakant D. Lokhande, “Chemically synthesized Cu₃Se₂ film based flexible solid-state symmetric supercapacitor: effect of reaction bath temperature”, The Journal of Physical Chemistry C, 124 (2020), 28395-28406 (*I. F. 4.19*).
12. Dhanaji B. Malavekar, Ravindra N. Bulakhe, **Shital B. Kale**, Umakant M. Patil, In-sik In, Chandrakant D. Lokhande, “Synthesis of layered copper selenide on reduced graphene oxide sheets via SILAR method for flexible asymmetric solid-state supercapacitor”, Journal of Alloys and Compounds, (2021)
13. Vikas J. Mane, **Shital B. Kale**, Shivaji B. Ubale, Vaibhav C. Lokhande, Chandrakant D. Lokhande, “Enhanced energy density silver doped-manganese oxide / graphene oxide composite electrodes for flexible solid-state symmetric supercapacitor” (Submitted).

CONFERENCES:

1. **Shital B. Kale**, Jin-Hyeok Kim, Chandrakant D. Lokhande, “Self-grown nanostructure of copper sulfide for energy conversion purpose” Korea Photovoltaic Society (KPVS) 2019 Fall Conference, Yeosu, South Korea, oral presentation.
2. **Shital B. Kale**, Chandrakant D. Lokhande, “Amorphous cobalt sulfide thin film electrocatalyst for oxygen evolution reaction” Anvenshan (Students’ research convention) 2019, Udaipur, Poster presentation.

CONTENTS

Candidate's Declaration.....	ii
Certificate of Guide.....	iii
Acknowledgement.....	iv
Research papers published in international journals.....	vi
National/international conferences attended.....	vii
Contents.....	viii
List of figures.....	ix
List of tables.....	xiv
List of Abbreviations.....	xv
Chapter 1: Introduction and literature survey.....	1
Chapter 2: Behind the method and characterization techniques used.....	29
Chapter 3: Synthesis, characterization and electrocatalytic OER performance of cobalt sulfide thin film electrode.....	67
Chapter 4: Synthesis, characterization and electrocatalytic OER performance of manganese cobalt sulfide thin film electrode.....	89
Chapter 5: Synthesis, characterization and electrocatalytic OER performance of nickel manganese cobalt sulfide/rGO thin film electrode.....	113
Chapter 6: Conclusions and future work.....	143

LIST OF FIGURES

Figure 1.1	Energy consumption for selected regions.....	2
Figure 1.2	Schematic of the electrolysis of water	4
Figure 2.1	Classification of thin film deposition methods.....	31
Figure 2.2	Schematic representation of SILAR method.....	33
Figure 2.3	Schematic of formation of Helmholtz double layer during 1 st step of SILAR.....	34
Figure 2.4	Schematic of rinsing of excess ions during 2 nd step of SILAR.....	35
Figure 2.5	Schematic of formation of water insoluble solid compound during 3 rd step of SILAR.....	36
Figure 2.6	Schematic of formation of monolayer of targeted material during 4 th step of SILAR.....	37
Figure 2.7	Photograph of SILAR machine used to deposit thin film electrodes in the present study	38
Figure 2.8	Schematic of substrate surface with different types of nucleation centers.....	39
Figure 2.9	Schematic of three growth mechanisms.....	40
Figure 2.10	Bragg's diffraction.....	45
Figure 2.11	The schematic of the x-ray diffractometer.....	46
Figure 2.12	Schematic of the x-ray tube.....	47
Figure 2.13	Schematic of FESEM instrument.....	49
Figure 2.14	Ray diagram for the emission of different types of electrons after the interaction of primary electrons from source with sample.....	50
Figure 2.15	Schematic of HR-TEM.....	52
Figure 2.16	Photographs of a) TEM grid holder and b) copper grid.....	53
Figure 2.17	Atomic model of the working principle of XPS.....	55

Figure 2.18	Energy-level diagram showing the states involved in Raman spectroscopy.....	56
Figure 2.19	Photograph of three electrodes experimental set up for electrochemical techniques used for this study.....	58
Figure 2.20	Cyclic voltammetry.....	59
Figure 2.21	a) Potential sweep between V_1 and V_2 with time in LSV and b) corresponding current response as a function of voltage.....	61
Figure 2.22	A typical Nyquist plot obtained from electrochemical impedance spectroscopy.....	64
Figure 3.1	Graphical representation of weight deposited of cobalt sulfide on SS substrate at 20 (CS-20), 40 (CS-40), 60 (CS-60) and 80 (CS-80) SILAR deposition cycles	72
Figure 3.2	Photograph of cobalt sulfide thin film electrodes prepared at different SILAR deposition cycles.....	72
Figure 3.3	The XRD patterns of bare SS substrate and cobalt sulfide thin film electrodes prepared at different deposition cycles	73
Figure 3.4	The FESEM images of Co_3S_4 thin film electrodes deposited at different SILAR cycles, (a, b) CS-20, (c, d) CS-40, (e, f) CS-60 and (g, h) CS-80 at 300X and 600X magnifications. (i) FESEM image of CS-80 at 50kX magnification.....	75
Figure 3.5	a) TEM image, b) (i) HAADF-STEM and (ii, iii) EDX elemental mapping and c) HR-TEM image of CS-80.....	76
Figure 3.6	a) Linear sweep voltammetry (LSV) curves at a scan rate of 2 mV s^{-1} and b) Tafel plots extracted from LSV curves of Co_3S_4 thin film electrocatalysts prepared at different deposition cycles.....	78
Figure 3.7	The cyclic voltammetry curves in a potential window of +0.1 to +0.3 V vs SCE for a) CS-20, b) CS-40, c) CS-60 and d) CS-80. e) Current density (at +0.2 V vs. SCE) vs. scan rate plots obtained from CV curves for all electrocatalysts.....	81
Figure 3.8	Nyquist plots (obtained from EIS) of Co_3S_4 thin film electrocatalysts prepared at different deposition cycles. The inset i) shows equivalent circuit model (ECM) and ii) shows magnified view of Nyquist plot in higher frequency region.....	82

Figure 3.9	a) 13 h stability test of CS-80 thin film electrocatalyst at 10 mA cm ⁻² , b) The LSV curves measured before and after stability study and c) Tafel plots extracted from LSV curves of CS-80 thin film electrocatalysts before and after stability study.....	84
Figure 4.1	XRD patterns of manganese cobalt sulfide thin film electrodes with different Co/Mn ratios	92
Figure 4.2	Raman spectra of (Co _x Mn _y)S thin film electrodes with different Co/Mn ratios.....	94
Figure 4.3	a) XPS survey spectrum of (Co ₃ Mn ₂)S thin film electrode. High resolution spectra of b) Co 2p, c) Mn 2p and d) S 2p	96
Figure 4.4	FESEM images of (Co _x Mn _y)S thin film electrodes with different Co/Mn ratios, a) (Co ₁ Mn ₀)S, b) (Co ₄ Mn ₁)S, c) (Co ₃ Mn ₂)S, d) (Co ₂ Mn ₃)S, e) (Co ₁ Mn ₄)S, and f) (Co ₀ Mn ₁)S at 100kX magnification.....	98
Figure 4.5	EDX elemental mapping of (Co _x Mn _y)S thin film electrodes with different Co/Mn ratios, a) (Co ₁ Mn ₀)S, b) (Co ₄ Mn ₁)S, c) (Co ₃ Mn ₂)S, d) (Co ₂ Mn ₃)S, e) (Co ₁ Mn ₄)S, and f) (Co ₀ Mn ₁)S.....	100
Figure 4.6	a) HR-TEM image, b) SAED pattern and c) (i) HAADF-STEM and (ii, iii iv) EDX elemental mapping of (Co ₃ Mn ₂)S thin film electrode	101
Figure 4.7	Electrochemical OER performance of (Co _x Mn _y)S thin film electrocatalysts with different Co/Mn ratios, a) LSV curves with the magnified view shown inset, b) overpotential required to reach 10 mA cm ⁻² current density and c) Tafel slope.....	102
Figure 4.8	Cyclic voltammetry curves in the potential window of 0.00 to +0.15 V vs. SCE for a) (Co ₁ Mn ₀)S, b) (Co ₄ Mn ₁)S, c) (Co ₃ Mn ₂)S, d) (Co ₂ Mn ₃)S, e) (Co ₁ Mn ₄)S, and f) (Co ₀ Mn ₁)S thin film electrocatalysts with corresponding current density (at +0.12 V vs. SCE) vs. scan rate plots shown in insets	104
Figure 4.9	Electrochemical active surface area of (Co _x Mn _y)S thin film electrocatalysts with different Co/Mn ratios	105
Figure 4.10	Electrochemical impedance spectroscopy study of (Co _x Mn _y)S thin film electrocatalysts prepared at different Co/Mn ratios, a)	

	Nyquist plots, b) equivalent circuit model (ECM), c) and d) polarization resistances obtained by ECM fitting.....	106
Figure 4.11	Long term durability performance of (Co ₃ Mn ₂)S thin film electrocatalyst at 10 mA cm ⁻²	107
Figure 5.1	a) XRD patterns and b) EDX spectra of NMC sulfide thin film electrodes with different Ni:Mn:Co ratios.....	116
Figure 5.2	a) XPS survey spectrum of NMC-212. High resolution spectra of b) Co 2p, c) Mn 2p, d) Ni 2p and e) S 2p.....	118
Figure 5.3	FESEM images of NMC sulfide thin film electrodes with different Ni:Mn:Co ratios, a-c) NMC-311, d-f) NMC-113, g-i) NMC-131 and j-l) NMC-212 at different magnifications of 25kX, 50kX and 70kX.....	119
Figure 5.4	EDX elemental mapping of NMC-212 thin film electrode.....	120
Figure 5.5	a) TEM image and b) SAED pattern of NMC-212 thin film electrode.....	121
Figure 5.6	Electrochemical OER performance of NMC sulfide thin film electrocatalysts with different Ni:Mn:Co ratios, a) LSV curves, b) overpotential required to achieve 10, 50 and 100 mA cm ⁻² current density and c) Tafel slope.....	122
Figure 5.7	Electrochemical impedance spectra of NMC sulfide thin film electrocatalysts with different Ni:Mn:Co ratios. Inset shows obtained values of R _s and R _{ct} represented in tabular form	123
Figure 5.8	XRD patterns of GO and rGO.....	126
Figure 5.9	XRD patterns of NMC/rGO composite thin film electrodes with different rGO cycles.....	127
Figure 5.10	Raman spectra of GO and rGO.....	129
Figure 5.11	The XPS survey spectra of a) GO and b) rGO. XPS high-resolution spectra of C 1s of c) GO, d) rGO and O 1s of e) GO and f) rGO.....	130
Figure 5.12	FESEM images of GO (a) at 30 X and (b) at 30k X magnifications and rGO (c) at 30 X and (d) at 30k X magnifications.....	132

Figure 5.13	FESEM images of (a and b) NMC/rGO-1, (c and d) NMC/rGO-20 and (e and f) NMC/rGO-40 with 25kX and 70kX magnifications	133
Figure 5.14	Electrochemical OER performance of NMC/rGO composite thin film electrocatalysts with different rGO cycles, a) LSV curves and b) Tafel slope.....	135
Figure 5.15	Cyclic voltammetry curves in non-faradic region for a) NMC/rGO-1, b) NMC/rGO-20 and c) NMC/rGO-40. d) Corresponding current density vs. scan rate plots for all electrocatalysts	136
Figure 5.16	a) Nyquist plots obtained from electrochemical impedance spectroscopy of NMC/rGO composite electrocatalysts (Inset shows corresponding values of R_s and R_{ct}) and b) Long term durability of NMC/rGO-20 thin film electrocatalyst at 10 mA cm ⁻² constant current density.....	137
Figure 5.17	a) LSV curves before and after stability study and b) XRD spectrum of NMC/rGO-20 thin film electrocatalyst after stability test.....	138
Figure 6.1	Comparison of the overpotential of thin film electrocatalysts obtained in the present study with overpotentials of cobalt, nickel and manganese containing single, binary and ternary sulfides reported in the literature.....	146

LIST OF TABLES

Table 1.1	The electrocatalytic OER performance of cobalt, nickel and manganese containing metal, binary and ternary sulfides in terms of overpotential and Tafel slope.....	12
Table 3.1	Electrochemical parameters obtained for Co_3S_4 thin film electrocatalysts prepared at different SILAR deposition cycles...	70
Table 4.1	Sample coding according to the Co/Mn ratio used.....	91
Table 4.2	Atomic percentage of Co, Mn and S in $(\text{Co}_x\text{Mn}_y)\text{S}$ thin film electrodes with different Co/Mn ratios obtained from EDX spectroscopy.....	93
Table 5.1	Atomic percentage of NMC sulfides thin film electrodes with different Ni:Mn:Co ratios.....	116
Table 5.2	Atomic percentage of NMC/rGO thin film electrodes with different rGO cycles.....	128
Table 6.1	Comparative summary of thin film electrodes deposited by SILAR method for the application of electrocatalytic OER in present study.....	147

LIST OF ABBREVIATIONS

CBD	Chemical Bath Deposition
CC	Carbon Cloth
C_{dl}	Double Layer Capacitance
CNT	Carbon Nanotube
CV	Cyclic Voltammetry
CVD	Chemical Vapor Deposition
DDW	Double Distilled Water
DES	Deep Eutectic Solvent
DFT	Density Functional Theory
ECM	Equivalent Circuit Model
ECSA	Electrochemical Active Surface Area
EDX	Energy-Dispersive X-Ray Spectroscopy
EIA	Energy Information Administration
EIS	Electrochemical Impedance Spectroscopy
FE-SEM	Field Emission Scanning Electron Microscopy
GCE	Glassy Carbon Electrode
GGE	Gasoline Gallon Equivalent
GO	Graphene Oxide
HAADF	High-Angle Annular Dark-Field Imaging
HER	Hydrogen Evolution Reaction
HR-TEM	High-Resolution Transmission Electron Microscopy
IHP	Inner Helmholtz plane
KOH	Potassium Hydroxide

LCVD	Laser Chemical Vapor Deposition
LSV	Linear Sweep Voltammetry
MOCVD	Metal-Organic Chemical Vapor Deposition
MWCNT	Multiwalled Carbon Nanotube
NF	Nickel Foam
OER	Oxygen Evolution Reaction
OHP	Outer Helmholtz plane
PEG	Polyethylene Glycol
R_{ct}	Charge Transfer Resistance
RDE	Rotating Disk Electrode
RF	Radiofrequency
rGO	Reduced Graphene Oxide
RHE	Reversible Hydrogen Electrode
R_s	Solution Resistance
SAED	Selected Area Diffraction
SCE	Saturated Calomel Electrode
SILAR	Successive Ionic Layer Adsorption and Reaction
SS	Stainless Steel
XAFS	X-Ray Absorption Fine Structure
XANES	X-Ray Absorption Near Edge Structure
XPS	X-ray Photoelectron Spectroscopy
XRD	X-ray Diffraction

CHAPTER 1

Introduction and literature survey

Chapter 1: Introduction and literature survey

1.1. Background.....	1
1.2. Electrochemical water splitting.....	3
1.3. OER and measurement parameters.....	5
1.4. Oxygen evolution electrocatalysts.....	7
1.5. Orientation and purpose of the thesis.....	18
1.6 References.....	19

1.1. Background

About 1.5 million years ago a spark lead to the first human-made fire and ignited a great revolution for species, a revolution of energy. Since that, energy is one of the main drivers of the economic and social development of humankind. Our ancestors were producing energy by burning biomass. With the special ability to think human civilization evolved through the bronze and iron age using this source of energy. In 300 B. C. E. humans started to harness energy from various sources and also started to search for new ones. In the 1800s mankind has the second energy revolution, the use of fossil fuels. By burning fossil fuels, the world has transformed with industrial machinery and communication. Fossil fuels, including coal, oil and natural gas, are currently the world's primary energy source. Fossil fuels are hydrocarbons formed from the remains of dead plants and animals by exposure to heat and pressure over the course of millions of years in the earth's crust. To fulfill the energy need we dig or drill this stuff out for a long time. Along with the increasing world population, we are becoming more and more digitalized civilization due to which the energy demand is also increasing. According to the international energy outlook prepared by the U.S. Energy Information Administration (EIA) in September 2019 (with projection to 2050), the world energy consumption will grow by nearly 50% between 2018 and 2050 (Figure 1.1 shows energy consumption for selected regions) [1].

Right now, fossil fuels supply 80% of that energy. As we know that the stock of fossil fuels under the earth's crust is limited and going to be exhausted soon. Because of their origins, fossil fuels have high carbon content, hence burning them releases carbon dioxide (CO_2) in the atmosphere which causes the greenhouse effect [2,3]. Due to this, it is widely agreed that fossil fuels cannot be the major energy

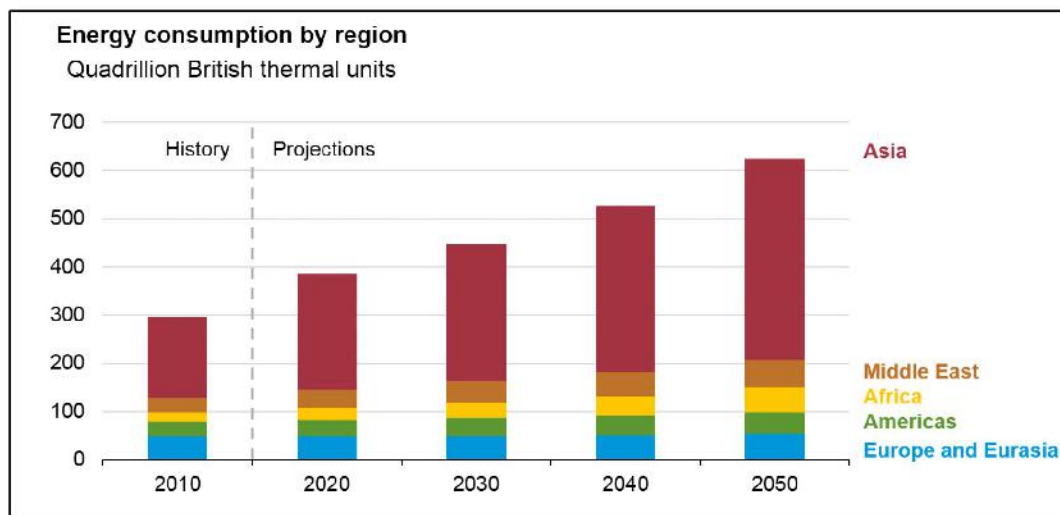


Figure 1.1: Energy consumption for selected regions

supplier. This motivated intense research into the pursuit and utilization of clean and sustainable alternative energy sources [4,5].

The answer to the question ‘Is there any alternative to fossil fuels?’ is yes, hydrogen fuel (H_2). Hydrogen has been proposed as possibly the main carrier for the new wave of a renewable form of energy and has been termed as the hydrogen economy or more recently transitioning to a hydrogen society [6–10]. Hydrogen is zero-emission fuel burned with oxygen. Hydrogen has high energy content, when compared on the scale of gasoline gallon equivalent (GGE) it takes only 1 kg of hydrogen fuel to equal the energy output of 1 gallon of gasoline [11]. Due to high energy output and carbon-free combustion hydrogen is considered an ideal alternative to fossil fuels [12]. As pure hydrogen does not occur naturally, primary energy input is used to produce it on an industrial scale. Steam reforming of natural gases, coal gasification and electrolysis of water are widely known methods for hydrogen production. Steam reforming is the major contributing method in hydrogen production. Natural gas such as methane is mixed with water vapor under high pressure in a reformer vessel. The hydrogen is produced via a strongly endothermic reaction $CH_4 + H_2O \rightarrow CO + 3H_2$

$2\text{H}_2\text{O} \rightleftharpoons \text{CO}_2 + 4\text{H}_2$. To produce hydrogen from coal, coal gasification is used.

The drawback of both above mentioned methods is the requirement of fossil fuels for hydrogen production. Also, a large amount of CO_2 is produced during these methods, which is very harmful to the environment. Water electrolysis is the only method to produce hydrogen without the use of fossil fuels. In which water is decomposed into molecular oxygen (O_2) and hydrogen (H_2) by passing an electric current. It is also a carbon-free way of hydrogen generation. But as of 2018, 95% of the world's hydrogen is produced from fossil fuels by steam reforming and coal gasification and only a small quantity by electrolysis of water [13]. Also, the electricity required for water splitting can be generated from any renewable source such as wind or solar farms. Hence it will be an indirect approach to use renewable energy sources.

1.2. Electrochemical water splitting

Electrochemical water splitting or electrolysis of water is the most feasible hydrogen production method at the time being. Electrolysis is the process by which a compound is break-down into its constituent molecules using electricity. The reaction of electrochemical water splitting can be written as



This overall water splitting reaction is consisting of two half-reactions, Hydrogen evolution reaction (HER) at cathode and oxygen evolution reaction (OER) at the anode. Figure 1.2 shows the simple setup of the electrolysis of water.

During OER at the anode, oxidation of water takes place as follow



while during IIER at the cathode, hydrogen ions get reduced to form molecular hydrogen as follow:



The standard water oxidation potential is 1.23 V and reduction potential is 0 V versus reversible hydrogen electrode (RHE) at standard temperature and pressure. Hence theoretically, a voltage difference of 1.23 V must be applied between anode and cathode in order to perform water splitting reaction.

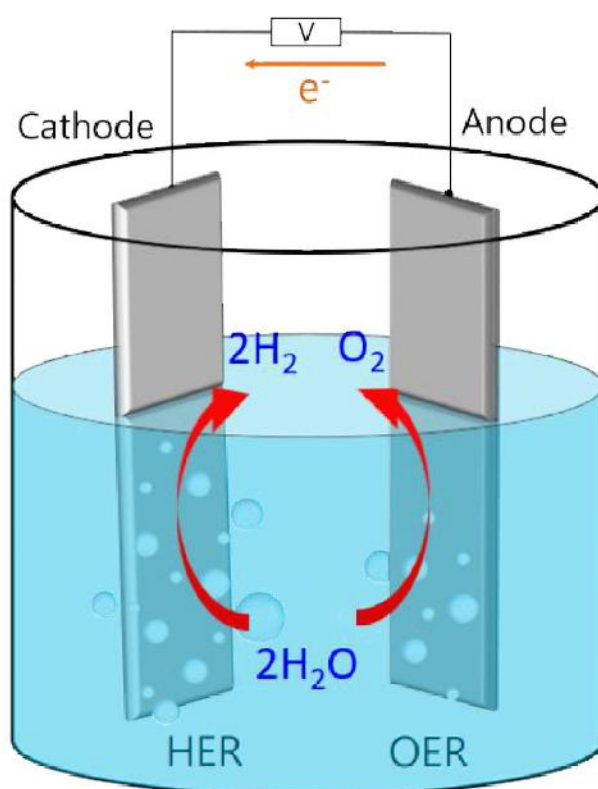


Figure 1.2: Schematic of the electrolysis of water

However, in practice, some extra potential in addition to standard one is necessary to overcome kinetic barriers at electrodes, which results in low efficiency of water splitting. This extra potential is called overpotential (η). To minimize energy loss, we need to minimize this overpotential. In this situation, electrocatalyst plays an

important role by increasing the rate of electrochemical reaction via participating in it [14]. Even though electrochemical water splitting is known since the 19th century, its practical applications are limited due to the OER. Among the HER and OER, OER is sluggish and complicated [15,16]. Also, it demands high overpotential which affects the overall water splitting process. For these reasons, OER has been studied intensively for decades to minimize overpotential.

As work in the present study has focused on OER, therefore the next sections of this chapter cover OER, different parameters used to examine good OER electrocatalyst and a literature survey of recent electrocatalysts for OER.

1.3. Oxygen evolution reaction (OER) and measurement parameters

As seen in the above section, OER is the half reaction of water splitting that takes place at the cathode. Many research groups have proposed possible mechanisms for OER [17,18]. Typically, all these mechanisms involve the formation of intermediates, for example, E=O, E-OH, and E-OOH (where E represents the electrocatalysts).

OER mechanism:



Hence, to produce one molecule of oxygen four electrons must be transferred at each step of the multi-step OER reaction. Thus, the accumulation of energy at each step

makes OER kinetics very sluggish and results in large overpotential. Therefore, an electrocatalyst with high activity towards OER to overcome the energy barrier by accelerating the charge transfer at the electrode and electrolyte interface is highly desirable [19,20]. To date, oxides of ruthenium (RuO_2) and iridium (IrO_2) exhibit the most attractive electrocatalytic properties for OER [21,22]. However, due to the pre-existing instability under OER operation, they oxidize from RuO_2 and IrO_2 to RuO_4 and IrO_3 , respectively [23,24]. Besides, Ru and Ir are highly precious due to their scarcity, which limits their wide-spread application. Thus, it is well desirable to investigate and develop novel low-cost and efficient materials as alternative electrocatalysts for OER, which can realize large-scale water electrolysis.

Catalyst material for OER is the most important element for the good performance of the reaction. Therefore, different parameters used to evaluate an electrocatalyst are important.

Overpotential (η)

As seen above, the extra potential required for an electrochemical reaction than its standard potential is called overpotential. Therefore, it is a most significant factor to evaluate the performance of OER catalysts. The overpotential required by an electrocatalyst to reach any current density j can be calculated by equation (2.5), given in the next chapter. However, 10 mA cm^{-2} is a benchmarking current density most widely accepted for evaluating electrochemical OER performances, because it is nearly equivalent to the current density likely to be obtained from a photovoltaic cell subjected towards 1 sun illumination. A Good OER electrocatalyst should reach a fixed current density with minimum overpotential.

Tafel slope (b)

Tafel slope is an important parameter to understand the reaction kinetics as

well as to compare the catalytic activity of different catalysts. The Tafel slope can be calculated by equation (2.6), given in the next chapter. A Good OER electrocatalyst should possess a low Tafel slope.

Stability

The stability of a catalyst is a very important factor for practical applications. A catalyst needs to be stable to have any real application. The stability of electrocatalyst for OER is normally demonstrated by maintaining either a current density of at least 10 mA cm^{-2} or potential at least required for 10 mA cm^{-2} current density for several hours.

1.4 Oxygen evolution electrocatalysts

As seen in the above section, the formation of different intermediates takes place with the extraction of four electrons during OER. Given this, the electrocatalyst material becomes critically eminent. Indeed, it must overcome significant challenges to be considered an effective electrocatalyst for oxygen evolution. A suitable catalyst must bind the reactants (intermediate species) neither too strongly nor too feebly, because, according to Sabatier's principle strong or feeble binding leads to either poor adsorption of reactants or difficulty in removing final products, respectively, [25]. The state-of-the-art OER catalysts have intermediate bonding strengths, which is one of the reasons for their excellent activity. The electrochemical water oxidation reaction takes place only on active sites existed at the surface of catalyst material; hence, an efficient electrocatalyst must possess a larger quantity of active sites [26]. During OER an electron is generated at each intermediate step. These electrons must be conducted to another half part of the water splitting reaction (or to anode) through an external circuit. For this, the electrocatalyst must be an electrically good conductor

[27]. Therefore, the catalyst materials which can overcome these obstacles are highly appreciable in the field of electrochemical water splitting.

In the past decades, considerable efforts have been devoted to the development of an efficient electrocatalyst for OER. As the state-of-the-art catalysts for oxygen evolution reaction are expensive and rare, there has been considerable interest in oxygen evolution electrocatalysts that use more abundant elements. An extensive literature survey suggests that the first row (3d) transition metals have long been known to be effective OER catalysts because of their low cost, high activity and long term stability under oxidation conditions. Among them, cobalt nickel and manganese are at the top of the hierarchy of transition metal based electrocatalysts [28]. There have reports demonstrating impressive performances for electrochemical water splitting with electrocatalysts based upon single, binary or even ternary transition metals.

Metal oxides as OER catalysts

Up to now, numerous investigations have been reported while examining transition metal oxides in the thirst for identifying suitable electrocatalyst for water oxidation. Among the transition metal based oxide catalysts, cobalt oxide is one of the earlier used oxides as an OER catalyst in an alkaline medium due to its high stability and special 3d electronic configuration [29-31]. Although cobalt oxides have good stability and good catalytic activity, it is still inferior to noble metal oxides. It is found that binary, as well as ternary metal oxides, show better electrocatalytic OER performance than corresponding single metal oxide [32-40]. More than one transition metals produce synergistic effects that can effectively regulate the physicochemical properties of oxides and further improve catalytic activity. Most of the above-mentioned metal oxides show the excellent electrocatalytic ability for OER, still, their

usage is constrained due to the poor intrinsic electronic conductivity.

Metal sulfides as OER catalysts

Compared to metal oxides, metal sulfides are a more prominent class of materials for OER. Most of the metal sulfides have strong and highly covalent M-S (M is metal site) and S-S bonds [41]. Different sulfide minerals exist in nature such as chalcocite (Cu_2S), pyrite (FeS_2) and so on [42]. Along with these, the most important property of metal sulfides is their intrinsic electronic conductivity. In metal sulfides, the energy gap between metal and sulfide 3p6 level is smaller as compared to the metal and oxygen 2p6 level in the corresponding metal oxide. This gives a higher intrinsic conductivity to metal sulfides than corresponding oxides. Due to all these favorable properties, nanostructured transition metal sulfides have emerged as a new class of electrocatalyst material for OER. Nickel sulfide and cobalt sulfide are widely studied single metal sulfides for OER application and have also shown good catalytic performance [61-77]. In the case of metal sulfides, it is found that the active sites are located at the metal site. Therefore, the sulfides containing more than one transition metal have more activity than single metal sulfides. Hence, nickel and cobalt containing binary or ternary metal sulfides possibly show excellent OER activity.

Different compositions of nickel-cobalt sulfides are reported upto now from which spinel structure (NiCo_2S_4) has attended more research interest due to the presence of octahedrally coordinated cations [43]. The phase pure pentlandite $\text{Ni}_{4.3}\text{Co}_{4.7}\text{S}_8$ reported by Tang et. al. [44] required only 134 mV overpotential to reach 20 mA cm^{-2} current density. Nearest metal-metal bonds are favorable for the adsorption of reactants and intermediates [45,46]. From the periodic table, nickel and cobalt have slightly high electronegativity (~ 1.9) which results in much stronger bonding between the metal atoms and intermediates, which is not favorable for a good

electrocatalyst [41]. The stoichiometric tailoring of moderate electronegative transition metal atom (such as Mn) with one of these highly electronegative transition metals can modify the electronic structure of resultant material, which may fulfill the criteria suggested by Sabatier principle for an excellent catalyst resulting in characteristics resembling those of noble materials. From the literature survey, it can be observed that till now manganese based sulfides are not that much explored in the field of OER. Manganese-cobalt sulfide is one of the trending materials in the field of energy storage [47–52]. Li et. al. [53] and Zhang et. al. [54] reported binder free manganese-cobalt sulfide for electrocatalytic application. In both reports, manganese-cobalt sulfide exhibited excellent activity with high current density.

Ternary metal sulfides are nowadays being proposed as promising materials for energy storage as well as conversion applications. The co-existence of multi metal atoms in an optimum stoichiometry can modify the electronic structure of the overall material, given that they possess different d-orbital structures [55]. Sahoo et. al. [56] electrodeposited nickel cobalt manganese sulfide on nickel foam and studied its supercapacitive performance. Also, Wang et. al. [57] studied supercapacitive performance of porous manganese nickel cobalt sulfide. Nanosheets of cobalt manganese nickel sulfide grown on nickel foam by Verma et. al. [58] show battery-like behavior. Hence, irrespective of composition the ternary metal sulfides based on nickel, manganese and cobalt elements give an excellent electrochemical performance. There is no report available on the electrocatalytic performance of this material. Another interesting material that has changed the trends in materials science is a two-dimensional hexagonal lattice of carbon i.e. graphene [59]. Graphene is only one atom thick two-dimensional carbon structure, with excellent electronic, mechanical, optical and thermal properties. It has a high specific surface area (theoretically $2630 \text{ m}^2\text{g}^{-1}$)

and good chemical stability. Therefore, it has been widely explored for applications in electronics, catalysis, sensors, energy conversion and storage. Due to the high electronic conductivity, reduced graphene (rGO) oxide has attracted considerable interest. The composites of electrocatalyst with rGO show drastic enhancement in its original performance. By simple electrodeposition method Evariste et. al. [60] deposited manganese-nickel-cobalt sulfide-rGO composite on nickel foam which shows excellent supercapacitor performance. But this material is yet not studied for electrochemical OER performance. Hence it will be more interesting to report such novel material through the present study.

Table 1.1 The electrocatalytic OER performance of cobalt, nickel and manganese containing metal, binary and ternary sulfides in terms of overpotential and Tafel slope.

Sr. No.	Material	Electrolyte	Substrate	Overpotential @ 10 mA cm ⁻² (mV)	Tafel slope (mV/decade)	Stability (h)	Remark	Ref.
1.	CoS	1M KOH	Ti mesh	361	64	20	Deposited cobalt-sulfide nanosheets film on Ti mesh (Co-S/Ti mesh) via electrodeposition and used as novel oxygen evolution anode in basic medium.	[61]
2.	Co ₃ S ₄	1M KOH	GCE	360	84.7	10	Hydrophilic Co ₃ S ₄ shows better performance than hydrophobic the surface hydrophilicity is very important.	[62]
3.	Co-nanoparticles	0.1M KOH	GCE	390	-	6	Better electron-conductivity of the metallic core gives an enhanced electrochemical performance.	[63]
4.	Co ₉ S ₈ /Co _{1-x} S	1M KOH	GCE	275	30	10	Morphology controlled by ratio of ethylene glycol and water (Solvent). Good performance due to adequate exposed-edge planes.	[64]
5.	Co ₉ S ₈	1M KOH	GCE	278	53	20	Hollow architecture, nanosheet units and high Co ³⁺ content.	[65]
6.	CoS _x	1M KOH	Gold-NF	271	48.8	300	Developed a new strategy to obtain amorphous CoS _x nanosheets.	[66]
7.	Co ₉ S ₈	1M KOH	GCE	285	58	10	Co ₉ S ₈ hollow spheres impart large surface area and luxuriant active sites.	[67]
8.	CoS	1M KOH	Ti foil	310	55	20	Time controlled electrosynthesis of CoS nanosheets which further evolved to a 3D flower like nanostructure, using potassium thiocyanate (KSCN) as sulfur source. Electrolyte accessing the reaction surface and the produced oxygen bubble escaping out for fast electrode kinetics.	[68]
9.	Co-S	1M KOH	GCE	312	-	36	Molecular amine mediated strategy for the one-step synthesis and surface modulation of thin cobalt-sulfide	[69]

							nanosheets. Favorable surface chemical environment including amounts of highly active Co(III) species, easy transform of Co(II) to Co(III), richness of defects, and higher electrochemical surface area.	
10.	NiS	1M KOH	NF	335 @50 mA cm ⁻²	89	35	NiS microspheres film was in situ grown on Ni foam (NiS/Ni foam) via sulfurization reaction.	[70]
11.	Ni ₃ S ₂	0.1M KOH	NF	217	163	1000 CV Cycles	Ni ₃ S ₂ nanorod arrays on acid treated Ni foam show better performance than non treated Ni foam. Highlights critical importance of pre-treatment of the pristine Ni foam with HCl for the successful preparation of the desired structure and morphology.	[71]
12.	NiS	0.1M KOH	SS mesh	297	47	10	Unique architecture providing direct contact between the active NiS and the highly conductive stainless steel substrate, which grants a highly efficient electron transfer pathway also sheet-like nanostructure gives a correct exposure of catalytic nickel centers.	[72]
13.	NiS _x	1M KOH	GCE	353	41	20	The ALD process temperature was shown to have an appreciable effect on various film properties, such as crystallinity, composition, density, and morphology. The atomic layer deposited NiS _x found to convert to nickel (oxy)hydrate after electrochemical aging, and the aged product shows a remarkable electrocatalytic activity.	[73]
14.	Ni ₃ S ₄	1M KOH	NF	257	67	300	The outstanding OER performance is due to the high concentration of Ni ³⁺ and the meso-macro hierarchical porous structure. Ni ³⁺ enhances the chemisorption of OH ⁻ , which facilitates electron transfer to the surface during OER.	[74]
15.	Ni _x S _y	1M KOH	NF	~220	106	1000 CV Cycles	Different crystal phases OF Ni _x S _y achieved successfully on different surface-treated (acidification and oxidation) nickel foam (NF). Discussed mechanisms of sulfurization paths of different surface-treated NF.	[75]
16.	Ni ₃ S ₂	1M KOH	NF	310	63	25	Deposited uniform spider web-like Ni nanosheets-Ni ₃ S ₂	[76]

							and honeycomb-like Ni ₃ S ₂ structures on nickel foam. Electrocatalytic performance of the metal sulfide fine-tuned and optimized with morphological controls.	
17.	Ni ₃ S ₂	1M KOH	NF	157	159	10	Obtained single-crystal Ni ₃ S ₂ nanorod decorated Ni foam by a simple hydrothermal reaction. The synergetic chemical coupling effects among hydrated Ni ₃ S ₂ nanorods, the nickel oxide layer and the Ni foam support resulted in an enhancement in OER performance.	[77]
18.	α -MnS	1M KOH	SS	292	70	10	Polymorphic thin films of MnS ₂ , γ -MnS, and α -MnS prepared from manganese carbonate through anion exchange and controlled reaction kinetics via a hydrothermal method. α -MnS exhibited lowest overpotential due to the lowest charge-transfer resistance, edge sharing MnS ₆ octahedra structure and highest electrochemical active surface area.	[78]
19.	Ni _{4.3} Co _{4.7} S ₈	1M KOH	NF	134 @20 mA cm ⁻²	194	8	Active metallic nickel source and chelating agent ethylenediamine play important roles in the formation of phase-pure pentlandite Ni _{4.3} Co _{4.7} S ₈ binary sulfide. Metallic characteristics of pentlandite phase with next-neighbor metal-metal bonds, a synergistic effect between Ni and Co ions endow higher catalytic activity for OER to Ni _{4.3} Co _{4.7} S ₈ electrocatalyst.	[44]
20.	Co _x Ni _{1-x} S	1M KOH	RDE	320	52	10	Developed cobalt nickel sulfide (Co _x Ni _{1-x} S ₂) (CNS) with a high density of crystalline and amorphous phase boundaries. High density crystalline/amorphous interfaces combined with unsaturated electronic configurations of Ni and Co atoms responsible for the excellent OER properties.	[79]
21.	Ni _{3.5} Co _{5.5} S ₈	1M KOH	GCE	333	48.5	5	Synthesized hollow nanocage of Ni _{3.5} Co _{5.5} S ₈ with thin nanosheets grown on the surface.	[80]
22.	NiCoS	1M KOH	GCE	320	59	10	Synthesized porous hollow nickel cobalt sulfide (NiCoS) using zeolitic imidazolate framework-67 (ZIF-67) as a sacrificial template.	[81]

							Hollow porous architecture facilitates mass transport and desirable composition for exposing more catalytic active and favorable OER kinetics.	
23.	(Ni,Co)S ₂	0.1M KOH	Carbon cloth	270	58	8	Single-phase bimetallic (Ni,Co)S ₂ nanosheets successfully synthesized by a hydrothermal route followed by thermal conversion to sulfide. Purposely tuned nanosheet morphology, electronic structure, enhanced electrical conductivity, and active sites in the bimetallic sulfides, the (Ni,Co)S ₂ nanosheets demonstrated a superior electrocatalytic performance for oxygen evolution.	[82]
24.	NiCo ₂ S ₄	1M KOH	NF	293	95	16	Needle grass array of nanostructured nickel cobalt sulfide (NiCo ₂ S ₄) synthesized using a hydrothermal process. Mixed transition metals provide promising synergistic electrochemical properties.	[83]
25.	CoS _x /Ni ₃ S ₂	1M KOH	NF	280 @20mA cm ⁻²	106	10	Cobalt sulfide/nickel sulfide heterostructure supported by Ni foam synthesized by one pot hydrothermal method. Ni foam acted as source of Ni for Ni ₃ S ₂ . Prepared electrocatalyst showed an excellent activity because of the (a) elimination of the binder on electrode fabrication, (b) better charge-transfer efficiency because of Co-S-Ni moiety formation, (c) increment in the number of active sites, and (d) decrease in H- and O-containing species adsorption-free energy at the active sites.	[84]
26.	NiCo ₂ S ₄	1M KOH	GCE	337	64	30	Structure and composition of the as-synthesized sulfides tuned by adjustment of the ratio of the reactants in solvothermal method. PEGylated DES used as a solvent, a shape-control agent, and a sulfur source in the synthesis. High surface area and multi porous structure of the sulfides increased the catalytic surface area and improved the transport property of the electrons throughout the electrode.	[85]

27.	NiCo ₂ S ₄	1M KOH	Carbon cloth	260	72	160	Hierarchical spinel bimetallic sulfide nanostructures in situ grown on the CC were investigated for their electrochemical properties in different pH media.	[86]
28.	Ni _{2.3%} -CoS ₂	1M KOH	Carbon cloth	370 @100mV cm ⁻²	119	12	Development of nickel promoted cobalt disulfide nanowires array supported on carbon cloth using two step hydrothermal protocol.	[87]
29.	CMS	1M KOH	NF	298 @100mA cm ⁻²	44	10	Synthesized bimetallic cobalt–manganese sulfide supported on Ni foam (CMS/Ni) via a solvothermal method the morphology of CMS/Ni modulated after combining with the pure Co ₉ S ₈ and MnS. Due to the synergistic effect of Co and Mn, CMS/Ni electrode shows good performance than pure Co ₉ S ₈ /Ni and MnS/Ni electrodes.	[53]
30.	MnCo ₂ S ₄	1M KOH	Ti mesh	325 @50mA cm ⁻²	115	100	MnCo ₂ S ₄ nanowire array successfully developed on TM through sulfurization of the corresponding MnCo ₂ O ₄ nanowire array precursor.	[54]
31.	Co ₉ S ₈ -N doped C	0.1M KOH	RDE	570 @ 5 mA cm ⁻²	75	27	Designed and fabricated Co ₉ S ₈ embedded in porous nitrogen-doped carbon (N-C) matrix. Synergistic effect of the covalent coupling between Co ₉ S ₈ and N-C and the porous structure of N-C responsible for the enhanced catalytic activity and durability of Co ₉ S ₈ /N-C hybrid.	[88]
32.	Co ₉ S ₈ -S doped C	1M KOH	GCE	340	64	1000 CV Cycles	Cobalt sulfide/sulfur doped carbon composites (Co ₉ S ₈ /S-C) synthesized by calcining a rationally designed sulfur-containing cobalt coordination. Excellent electrocatalytic activity of Co ₉ S ₈ /S-C mainly attributed to the synergistic effect between the Co ₉ S ₈ catalyst which contributed to the oxygen evolution reaction and the sulfur doped carbon layer which served as the electrically conductive binder between each component.	[89]
33.	CoS ₂ /NS-GO	0.1M KOH	RDE	390	75	5000 CV Cycles	Cobalt sulfide nanoparticles dispersed on graphene oxide hybrids with different particle size and phase synthesized at various temperatures. The strong coupling between CoS ₂ and N,S-GO	[90]

							prepared at 400 ^o shows enhanced electrochemical performance.	
34.	CoS/CNT	1M KOH	GCE	347 @15 mA cm ⁻²	142	600 s	Nanocomposite of CoS with functionalized multiwalled carbon nanotubes (MWCNTs) prepared using ultrasonication and complexation. The low charge transfer resistance and high double layer capacitance result in good electrochemical performance.	[91]
35.	N-GO/Ni ₇ S ₆	0.1M KOH	RDE	380	45	12	Demonstrated the fabrication of a nanoporous composite NGO and a Ni-containing metal organic framework (MOF-74) which further successfully converted multisheet 2D nanocomposite (NGO/Ni ₇ S ₆) by treatment with thiourea as a sulfur source. Excellent catalytic activity attributed to the synergistic effect between the Ni ₇ S ₆ and NGO in terms of hierarchical porous behavior facilitating fast mass transport, significant textural parameters, the amount of nitrogen, accessible nickel active sites for high electrical conductivity, and mass transfer.	[92]

GCE-Glassy carbon electrode; NF-Nickel foam; SS-Stainless steel; RDE-Rotating disk electrode

1.5. Orientation and purpose of the thesis

It has been well documented that to store intermittent energy from renewable sources, we need an efficient energy carrier. In this scenario hydrogen economy is one of the promising solutions. But due to the sluggish kinetics, OER becomes a bottleneck for large scale hydrogen production. To increase the efficiency of water splitting, anodic half reaction (OER) must be accelerated. The high cost and low abundance of state-of-the-art OER catalyst materials kept them away from industrial applications. The presence of unfilled d-orbital in the 3d transition elements makes them a center of attraction in the field of electrochemical water splitting. Upto now, numerous materials containing these elements have been reported. Initially, oxides of these transition metals are considered promising OER catalysts due to their ability to form intermediate bonds with reactants easily. But the low value of their intrinsic conductivity makes them less compatible with practical application. On the other side, the sufficiently high conductivity of transition metal sulfides makes them promising candidates. It is observed that the binary and ternary metal sulfides are more active than primary metal sulfides. The recent trend suggests that the composites of these multimetal sulfides with 3-D carbon structure (graphene oxide) enhances the mass and charge transport efficiency. This helps to improve catalytic activity via increasing electronic conductivity, surface area and mechanical strength.

Nickel cobalt sulfide and manganese cobalt sulfide are widely studied materials in the field of supercapacitor but are rarely explored for electrochemical water splitting. Individual cobalt, manganese and nickel have shown moderate OER performance. Therefore, a ternary metal sulfide of nickel, manganese and cobalt will give excellent OER performance, which can be further enhanced by compositing it with reduced graphene oxide. The preparation of catalyst material in the form of thin

film is more admirable than the bulk form in the view of practical application. The physical methods of thin film deposition are expensive and put limitations on substrates. Therefore, the simple successive ionic layer adsorption and reaction (SILAR) method is more appreciable for the deposition of thin films of various materials. Hence the present study is focused on the synthesis of nickel manganese cobalt sulfide / rGO composite thin films using SILAR method on stainless steel substrates. To minimize the overpotential required for OER is the main intention of the present study.

A composite thin film electrocatalyst of nickel manganese cobalt sulfide with reduced graphene oxide is synthesized by SILAR method. The physicochemical properties of material greatly influence its catalytic activity. Therefore, various characterization techniques such as X-ray diffraction (XRD), Raman, field emission scanning electron microscopy (FE-SEM) and transmission electron microscopy (TEM) are used to study material properties. The electrochemical performance of electrocatalysts towards OER is tested in three electrode system. Linear sweep voltammetry (LSV), cyclic voltammetry (CV), chronopotentiometry and electrochemical impedance spectroscopy (EIS) techniques are used to evaluate different electrocatalysts.

1.6. References

- [1] International Energy Outlook 2019, 2019. <https://www.eia.gov/ieo>.
- [2] G. A. Olah, G. K. S. Prakash, A. Goeppert, Anthropogenic chemical carbon cycle for a sustainable future, *J. Am. Chem. Soc.* 133 (2011) 12881–12898. <https://doi.org/10.1021/ja202642y>.
- [3] A. Woodward, K. R. Smith, D. Campbell-Lendrum, D. D. Chadee, Y. Honda, Q. Liu, J. Olwoch, B. Revich, R. Sauerborn, Z. Chafe, U. Confalonieri, A. Haines, Climate change and health: On the latest IPCC report, *Lancet.* 383 (2014) 1185–1189. [https://doi.org/10.1016/S0140-6736\(14\)60576-6](https://doi.org/10.1016/S0140-6736(14)60576-6).

- [4] T. R. Cook, D. K. Dogutan, S. Y. Reece, Y. Surendranath, T. S. Teets, D. G. Nocera, Solar energy supply and storage for the legacy and nonlegacy worlds, *Chem. Rev.* 110 (2010) 6474–6502. <https://doi.org/10.1021/cr100246c>.
- [5] P. Zhang, J. Zhang, J. Gong, Tantalum-based semiconductors for solar water splitting, *Chem. Soc. Rev.* 43 (2014) 4395–4422. <https://doi.org/10.1039/c3cs60438a>.
- [6] D. Rand and R. M. Dell, Chapter 8. Hydrogen energy: The future?, in: *Hydrog. Energy Challenges Prospect.*, The Royal Society of Chemistry (2008) 275–295. <https://doi.org/10.1039/9781847558022>.
- [7] C. Acar, I. Dincer, 1.13 Hydrogen energy, Volume 1: Energy Fundamentals, *Comprehensive Energy Systems*, Elsevier (2018) 568–605. <https://doi.org/10.1016/B978-0-12-809597-3.00113-9>.
- [8] P2G System technology development aiming at building a CO₂-free hydrogen society, ECS Meet. Abstr. (2019). <https://doi.org/10.1149/ma2019-02/37/1703>.
- [9] T. Yoshida, K. Kojima, Toyota MIRAI fuel cell vehicle and progress toward a future hydrogen society, *Electrochem. Soc. Interface.* 24 (2015) 45–49. <https://doi.org/10.1149/2.F03152if>.
- [10] S. Chu, A. Majumdar, Opportunities and challenges for a sustainable energy future, *Nature.* 488 (2012) 294–303. <https://doi.org/10.1038/nature11475>.
- [11] Fuel specifications subcommittee, national institute of standards and technology (NIST), June 19 (2008).
- [12] R. F. Service, Hydrogen cars: Fad or the future?, *Science* 324 (2009) 1257–1259. https://doi.org/10.1126/science.324_1257.
- [13] https://en.wikipedia.org/wiki/Hydrogen_fuel.
- [14] Z. Lv, N. Mahmood, M. Tahir, L. Pan, X. Zhang, J. J. Zou, Fabrication of zero to three dimensional nanostructured molybdenum sulfides and their electrochemical and photocatalytic applications, *Nanoscale.* 8 (2016) 18250–18269. <https://doi.org/10.1039/c6nr06836g>.
- [15] P. Li, H. C. Zeng, Advanced oxygen evolution catalysis by bimetallic Ni-Fe phosphide nanoparticles encapsulated in nitrogen, phosphorus, and sulphur tri-doped porous carbon, *Chem. Commun.* 53 (2017) 6025–6028. <https://doi.org/10.1039/c7cc03005c>.
- [16] Z. L. Wang, D. Xu, J. J. Xu, X. B. Zhang, Oxygen electrocatalysts in metal-air batteries: From aqueous to nonaqueous electrolytes, *Chem. Soc. Rev.* 43 (2014) 7746–7786. <https://doi.org/10.1039/c3cs60248f>.
- [17] N. T. Suen, S. F. Hung, Q. Quan, N. Zhang, Y. J. Xu, H. M. Chen, Electrocatalysis for the oxygen evolution reaction: Recent development and future perspectives, *Chem. Soc. Rev.* 46 (2017) 337–365. <https://doi.org/10.1039/c6cs00328a>.

-
- [18] M. Fang, G. Dong, R. Wei, J. C. Ho, Hierarchical nanostructures: Design for sustainable water splitting, *Adv. Energy Mater.* 7 (2017) 1700559 (1-25). <https://doi.org/10.1002/aenm.201700559>.
- [19] M. Gong, Y. Li, H. Wang, Y. Liang, J. Z. Wu, J. Zhou, J. Wang, T. Regier, F. Wei, H. Dai, An advanced Ni-Fe layered double hydroxide electrocatalyst for water oxidation, *J. Am. Chem. Soc.* 135 (2013) 8452–8455. <https://doi.org/10.1021/ja4027715>.
- [20] M. Tahir, N. Mahmood, J. Zhu, A. Mahmood, F. K. Butt, S. Rizwan, I. Aslam, M. Tanveer, F. Idrees, I. Shakir, C. Cao, Y. Hou, One dimensional graphitic carbon nitrides as effective metal-free oxygen reduction catalysts, *Sci. Rep.* 5 (2015) 12389 (1-10). <https://doi.org/10.1038/srep12389>.
- [21] J. H. Montoya, L. C. Seitz, P. Chakthranont, A. Vojvodic, T. F. Jaramillo, J. K. Nørskov, Materials for solar fuels and chemicals, *Nat. Mater.* 16 (2016) 70–81. <https://doi.org/10.1038/nmat4778>.
- [22] C. Wei, R. R. Rao, J. Peng, B. Huang, I. E. L. Stephens, M. Risch, Z. J. Xu, Y. Shao-Horn, Recommended practices and benchmark activity for hydrogen and oxygen electrocatalysis in water splitting and fuel cells, *Adv. Mater.* 31 (2019) 1806296 (1-24). <https://doi.org/10.1002/adma.201806296>.
- [23] R. Kötz, Anodic iridium oxide films, *J. Electrochem. Soc.* 131 (1984) 72-77. <https://doi.org/10.1149/1.2115548>.
- [24] R. Kötz, XPS studies of oxygen evolution on Ru and RuO₂ anodes, *J. Electrochem. Soc.* 130 (1983) 825-829. <https://doi.org/10.1149/1.2119829>.
- [25] J. Hu, C. Zhang, X. Meng, H. Lin, C. Hu, X. Long, S. Yang, Hydrogen evolution electrocatalysis with binary-nonmetal transition metal compounds, *J. Mater. Chem. A* 5 (2017) 5995–6012. <https://doi.org/10.1039/c7ta00743d>.
- [26] Y. Guo, J. Tang, Z. Wang, Y. Sugahara, Y. Yamauchi, Hollow porous heterometallic phosphide nanocubes for enhanced electrochemical water splitting, *Small* 14 (2018) 1802442 (1-8). <https://doi.org/10.1002/smll.201802442>.
- [27] K. Xu, P. Chen, X. Li, Y. Tong, H. Ding, X. Wu, W. Chu, Z. Peng, C. Wu, Y. Xie, Metallic nickel nitride nanosheets realizing enhanced electrochemical water oxidation, *J. Am. Chem. Soc.* 137 (2015) 4119–4125. <https://doi.org/10.1021/ja5119495>.
- [28] L. Han, S. Dong, E. Wang, Transition-metal (Co, Ni, and Fe)-based electrocatalysts for the water oxidation reaction, *Adv. Mater.* 28 (2016) 9266–9291. <https://doi.org/10.1002/adma.201602270>.
- [29] L. I. Krishtalik, Kinetics and mechanism of anodic chlorine and oxygen evolution reactions on transition metal oxide electrodes, *Electrochim. Acta* 26 (1981) 329–337. [https://doi.org/https://doi.org/10.1016/0013-4686\(81\)85019-0](https://doi.org/https://doi.org/10.1016/0013-4686(81)85019-0).
- [30] Y. Tong, P. Chen, T. Zhou, K. Xu, W. Chu, C. Wu, Y. Xie, A bifunctional hybrid
-

- hr/>
- electrocatalyst for oxygen reduction and evolution: cobalt oxide nanoparticles strongly coupled to B, N-decorated graphene, *Angew. Chemie Int. Ed.* 56 (2017) 7121–7125. <https://doi.org/10.1002/anie.201702430>.
- [31] Y. Li, F. M. Li, X. Y. Meng, S. N. Li, J. H. Zeng, Y. Chen, Ultrathin Co_3O_4 nanomeshes for the oxygen evolution reaction, *ACS Catal.* 8 (2018) 1913–1920. <https://doi.org/10.1021/acscatal.7b03949>.
- [32] I. Barauskienė, E. Valatka, Layered Nickel-cobalt oxide coatings on stainless steel as an electrocatalyst for oxygen evolution reaction, *Electrocatalysis*. 10 (2019) 63–71. <https://doi.org/10.1007/s12678-018-0495-x>.
- [33] C. Zhu, D. Wen, S. Leubner, M. Oschatz, W. Liu, M. Holzschuh, F. Simon, S. Kaskel, A. Eychmüller, Nickel cobalt oxide hollow nanosponges as advanced electrocatalysts for the oxygen evolution reaction, *Chem. Commun.* 51 (2015) 7851–7854. <https://doi.org/10.1039/C5CC01558H>.
- [34] T. Ma, C. Li, X. Chen, F. Cheng, J. Chen, Spinel cobalt–manganese oxide supported on non-oxidized carbon nanotubes as a highly efficient oxygen reduction/evolution electrocatalyst, *Inorg. Chem. Front.* 4 (2017) 1628–1633. <https://doi.org/10.1039/C7QI00367F>.
- [35] M. Huynh, C. Shi, S. J. L. Billinge, D. G. Nocera, Nature of activated manganese oxide for oxygen evolution, *J. Am. Chem. Soc.* 137 (2015) 14887–14904. <https://doi.org/10.1021/jacs.5b06382>.
- [36] P. W. Menezes, A. Indra, O. Levy, K. Kailasam, V. Gutkin, J. Pfrommer, M. Driess, Using nickel manganese oxide catalysts for efficient water oxidation, *Chem. Commun.* 51 (2015) 5005–5008. <https://doi.org/10.1039/C4CC09671A>.
- [37] L. Han, L. Guo, C. Dong, C. Zhang, H. Gao, J. Niu, Z. Peng, Z. Zhang, Ternary mesoporous cobalt-iron-nickel oxide efficiently catalyzing oxygen/hydrogen evolution reactions and overall water splitting, *Nano Res.* 12 (2019) 2281–2287. <https://doi.org/10.1007/s12274-019-2389-5>.
- [38] P. Sivakumar, P. Subramanian, T. Maiyalagan, A. Gedanken, A. Schechter, Ternary nickel-cobalt-manganese spinel oxide nanoparticles as heterogeneous electrocatalysts for oxygen evolution and oxygen reduction reaction, *Mater. Chem. Phys.* 229 (2019) 190–196. <https://doi.org/10.1016/j.matchemphys.2019.03.017>.
- [39] I. M. Sadiq, A. M. Mohammad, M. E. El-Shakre, M. S. El-Deab, Electrocatalytic activity of nickel oxide nanoparticles-modified electrodes: Optimization of the loading level and operating pH towards the oxygen evolution reaction, *Int. J. Hydrogen Energy*. 37 (2012) 68–77. <https://doi.org/10.1016/j.ijhydene.2011.09.097>.
- [40] C. Broicher, F. Zeng, J. Artz, H. Hartmann, A. Besmehn, S. Palkovits, R. Palkovits, Facile synthesis of mesoporous nickel cobalt oxide for OER – insight into intrinsic electrocatalytic activity, *ChemCatChem*. 11 (2019) 412–416. <https://doi.org/10.1002/cctc.201801316>.

-
- [41] S. Anantharaj, S. R. Ede, K. Sakthikumar, K. Karthick, S. Mishra, S. Kundu, Recent trends and perspectives in electrochemical water splitting with an emphasis on sulfide, selenide, and phosphide catalysts of Fe, Co, and Ni: A review, *ACS Catal.* 6 (2016) 8069–8097. <https://doi.org/10.1021/acscatal.6b02479>.
- [42] C. H. Lai, M. Y. Lu, L. J. Chen, Metal sulfide nanostructures: synthesis, properties and applications in energy conversion and storage, *J. Mater. Chem.* 22 (2012) 19–30. <https://doi.org/10.1039/C1JM13879K>.
- [43] H. Knözinger, P. Ratnasamy, Catalytic aluminas: surface models and characterization of surface sites, *Catal. Rev.* 17 (1978) 31–70. <https://doi.org/10.1080/03602457808080878>.
- [44] Y. Tang, H. Yang, J. Sun, M. Xia, W. Guo, L. Yu, J. Yan, J. Zheng, L. Chang, F. Gao, Phase-pure pentlandite $\text{Ni}_{4.3}\text{Co}_{4.7}\text{S}_8$ binary sulfide as an efficient bifunctional electrocatalyst for oxygen evolution and hydrogen evolution, *Nanoscale*. 10 (2018) 10459–10466. <https://doi.org/10.1039/C8NR02402B>.
- [45] L. L. Feng, M. Fan, Y. Wu, Y. Liu, G. D. Li, H. Chen, W. Chen, D. Wang, X. Zou, Metallic Co_9S_8 nanosheets grown on carbon cloth as efficient binder-free electrocatalysts for the hydrogen evolution reaction in neutral media, *J. Mater. Chem. A*. 4 (2016) 6860–6867. <https://doi.org/10.1039/C5TA08611F>.
- [46] Z. F. Huang, J. Song, K. Li, M. Tahir, Y. T. Wang, L. Pan, L. Wang, X. Zhang, J. J. Zou, Hollow cobalt-based bimetallic sulfide polyhedra for efficient all-pH-value electrochemical and photocatalytic hydrogen evolution, *J. Am. Chem. Soc.* 138 (2016) 1359–1365. <https://doi.org/10.1021/jacs.5b11986>.
- [47] S. Liu, S. C. Jun, Hierarchical manganese cobalt sulfide core shell nanostructures for high-performance asymmetric supercapacitors, *J. Power Sources*. 342 (2017) 629–637. <https://doi.org/https://doi.org/10.1016/j.jpowsour.2016.12.057>.
- [48] M. Yu, X. Li, Y. Ma, R. Liu, J. Liu, S. Li, Nanohoneycomb-like manganese cobalt sulfide/three dimensional graphene-nickel foam hybrid electrodes for high-rate capability supercapacitors, *Appl. Surf. Sci.* 396 (2017) 1816–1824. <https://doi.org/https://doi.org/10.1016/j.apsusc.2016.11.203>.
- [49] Y. Zhao, Z. Shi, H. Li, C. A. Wang, Designing pinecone-like and hierarchical manganese cobalt sulfides for advanced supercapacitor electrodes, *J. Mater. Chem. A*. 6 (2018) 12782–12793. <https://doi.org/10.1039/C8TA02438C>.
- [50] X. Han, H. Xuan, J. Gao, T. Liang, J. Yang, Y. Xu, P. Han, Y. Du, Construction of manganese-cobalt-sulfide anchored onto rGO/Ni foam with a high capacity for hybrid supercapacitors, *Electrochim. Acta*. 288 (2018) 31–41. <https://doi.org/https://doi.org/10.1016/j.electacta.2018.08.063>.
- [51] F. Zhang, M. Cho, T. Eom, C. Kang, H. Lee, Facile synthesis of manganese cobalt sulfide nanoparticles as high-performance supercapacitor electrode, *Ceram. Int.* 45(2019) 20972–20976.
-

<https://doi.org/https://doi.org/10.1016/j.ceramint.2019.06.240>.

- [52] F. Wang, K. Zhou, J. Zheng, J. Ma, Rapid synthesis of porous manganese cobalt sulfide grown on Ni foam by microwave method for high performance supercapacitors, *Synth. Met.* 256 (2019) 116113 (1-7). <https://doi.org/https://doi.org/10.1016/j.synthmet.2019.116113>.
- [53] J. Li, W. Xu, J. Luo, D. Zhou, D. Zhang, L. Wei, P. Xu, D. Yuan, Synthesis of 3D hexagram-like cobalt–manganese sulfides nanosheets grown on nickel foam: A bifunctional electrocatalyst for overall water splitting, *Nano-Micro Lett.* 10 (2017) 6 (1-10). <https://doi.org/10.1007/s40820-017-0160-6>.
- [54] X. Zhang, C. Si, X. Guo, R. Kong, F. Qu, A MnCo_2S_4 nanowire array as an earth-abundant electrocatalyst for an efficient oxygen evolution reaction under alkaline conditions, *J. Mater. Chem. A* 5 (2017) 17211–17215. <https://doi.org/10.1039/c7ta04804a>.
- [55] B. Zhang, X. Zheng, O. Voznyy, R. Comin, M. Bajdich, M. García-Melchor, L. Han, J. Xu, M. Liu, L. Zheng, F. P. G. De Arquer, C. T. Dinh, F. Fan, M. Yuan, E. Yassitepe, N. Chen, T. Regier, P. Liu, Y. Li, P. De Luna, A. Janmohamed, H.L. Xin, H. Yang, A. Vojvodic, E.H. Sargent, Homogeneously dispersed multimetal oxygen-evolving catalysts, *Science* 352 (2016) 333–337. <https://doi.org/10.1126/science.aaf1525>.
- [56] S. Sahoo, R. Mondal, D. J. Late, C. S. Rout, Electrodeposited nickel cobalt manganese based mixed sulfide nanosheets for high performance supercapacitor application, *Microporous Mesoporous Mater.* 244 (2017) 101–108. <https://doi.org/https://doi.org/10.1016/j.micromeso.2017.02.043>.
- [57] X. Wang, Q. Zhang, J. Sun, Z. Zhou, Q. Li, B. He, J. Zhao, W. Lu, C.P. Wong, Y. Yao, Facile synthesis of hierarchical porous manganese nickel cobalt sulfide nanotube arrays with enhanced electrochemical performance for ultrahigh energy density fiber-shaped asymmetric supercapacitors, *J. Mater. Chem. A* 6 (2018) 8030–8038. <https://doi.org/10.1039/c8ta01440j>.
- [58] M. Verma, R. Yadav, L. Sinha, S. S. Mali, C. K. Hong, P. M. Shirage, Pseudocapacitive-battery-like behavior of cobalt manganese nickel sulfide (CoMnNiS) nanosheets grown on Ni-foam by electrodeposition for realizing high capacity, *RSC Adv.* 8 (2018) 40198–40209. <https://doi.org/10.1039/C8RA07471B>.
- [59] K. S. Novoselov, A. K. Geim, S. V Morozov, D. Jiang, Y. Zhang, S. V Dubonos, I. V Grigorieva, A. A. Firsov, Electric Field Effect in Atomically Thin Carbon Films, *Science* 306 (2004) 666–669. <https://doi.org/10.1126/science.1102896>.
- [60] U. Evariste, G. Jiang, B. Yu, Y. Liu, P. Ma, Electrodeposition of manganese-nickel-cobalt sulfides on reduced graphene oxide/nickel foam for high-performance asymmetric supercapacitors, *J. Electron. Mater.* 49 (2020) 922–930. <https://doi.org/10.1007/s11664-019-07810-6>.
- [61] T. Liu, Y. Liang, Q. Liu, X. Sun, Y. He, A. M. Asiri, Electrodeposition of

- cobalt-sulfide nanosheets film as an efficient electrocatalyst for oxygen evolution reaction, *Electrochem. Commun.* 60 (2015) 92–96. <https://doi.org/10.1016/j.elecom.2015.08.011>.
- [62] M. Zhu, Z. Zhang, H. Zhang, H. Zhang, X. Zhang, L. Zhang, S. Wang, Hydrophilic cobalt sulfide nanosheets as a bifunctional catalyst for oxygen and hydrogen evolution in electrolysis of alkaline aqueous solution, *J. Colloid Interface Sci.* 509 (2018) 522–528. <https://doi.org/10.1016/j.jcis.2017.09.076>.
- [63] L. Wu, Q. Li, C. H. Wu, H. Zhu, A. Mendoza-Garcia, B. Shen, J. Guo, S. Sun, Stable cobalt nanoparticles and their monolayer array as an efficient electrocatalyst for oxygen evolution reaction, *J. Am. Chem. Soc.* 137 (2015) 7071–7074. <https://doi.org/10.1021/jacs.5b04142>.
- [64] R. Lin, T. Lin, J. Huang, X. Huang, Y. Liu, Hierarchical cobalt sulfide with vertical in-plane edge structure for enhanced electrocatalytic oxygen evolution reaction, *Electrochim. Acta.* 281 (2018) 348–356. <https://doi.org/https://doi.org/10.1016/j.electacta.2018.05.184>.
- [65] H. Liu, F. X. Ma, C. Y. Xu, L. Yang, Y. Du, P. P. Wang, S. Yang, L. Zhen, Sulfurizing-induced hollowing of Co_9S_8 microplates with nanosheet units for highly efficient water oxidation, *ACS Appl. Mater. Interfaces.* 9 (2017) 11634–11641. <https://doi.org/10.1021/acsami.7b00899>.
- [66] X. Zhao, J. Jiang, Z. Xue, C. Yan, T. Mu, An ambient temperature, CO_2 -assisted solution processing of amorphous cobalt sulfide in a thiol/amine based quasi-ionic liquid for oxygen evolution catalysis, *Chem. Commun.* 53 (2017) 9418–9421. <https://doi.org/10.1039/C7CC05503J>.
- [67] X. Feng, Q. Jiao, T. Liu, Q. Li, M. Yin, Y. Zhao, H. Li, C. Feng, W. Zhou, Facile synthesis of Co_9S_8 hollow spheres as a high-performance electrocatalyst for the oxygen evolution reaction, *ACS Sustain. Chem. Eng.* 6 (2018) 1863–1871. <https://doi.org/10.1021/acssuschemeng.7b03236>.
- [68] K. Nan, H. Du, L. Su, C.M. Li, Directly electrodeposited cobalt sulfide nanosheets as advanced catalyst for oxygen evolution reaction, *Chemistry Select.* 3 (2018) 7081–7088. <https://doi.org/10.1002/slct.201801482>.
- [69] S. Ju, Y. Liu, H. Chen, F. Tan, A. Yuan, X. Li, G. Zhu, In situ surface chemistry engineering of cobalt-sulfide nanosheets for improved oxygen evolution activity, *ACS Appl. Energy Mater.* 2 (2019) 4439–4449. <https://doi.org/10.1021/acsaem.9b00687>.
- [70] W. Zhu, X. Yue, W. Zhang, S. Yu, Y. Zhang, J. Wang, J. Wang, Nickel sulfide microsphere film on Ni foam as an efficient bifunctional electrocatalyst for overall water splitting, *Chem. Commun.* 52 (2016) 1486–1489. <https://doi.org/10.1039/C5CC08064A>.
- [71] C. Ouyang, X. Wang, C. Wang, X. Zhang, J. Wu, Z. Ma, S. Dou, S. Wang, Hierarchically porous Ni_3S_2 nanorod array foam as highly efficient electrocatalyst for hydrogen evolution reaction and oxygen evolution reaction,

-
- Electrochim. Acta. 174 (2015) 297–301.
<https://doi.org/https://doi.org/10.1016/j.electacta.2015.05.186>.
- [72] J. S. Chen, J. Ren, M. Shalom, T. Fellingner, M. Antonietti, Stainless steel mesh-supported nis nanosheet array as highly efficient catalyst for oxygen evolution reaction, *ACS Appl. Mater. Interfaces*. 8 (2016) 5509–5516.
<https://doi.org/10.1021/acsami.5b10099>.
- [73] H. Li, Y. Shao, Y. Su, Y. Gao, X. Wang, Vapor-phase atomic layer deposition of nickel sulfide and its application for efficient oxygen-evolution electrocatalysis, *Chem. Mater.* 28 (2016) 1155–1164.
<https://doi.org/10.1021/acs.chemmater.5b04645>.
- [74] K. Wan, J. Luo, C. Zhou, T. Zhang, J. Arbiol, X. Lu, B. W. Mao, X. Zhang, J. Fransaer, Hierarchical porous Ni₃S₄ with enriched high-valence Ni sites as a robust electrocatalyst for efficient oxygen evolution reaction, *Adv. Funct. Mater.* 29 (2019) 1900315 (1-8). <https://doi.org/10.1002/adfm.201900315>.
- [75] X. Shang, X. Li, W. H. Hu, B. Dong, Y. R. Liu, G. Q. Han, Y. M. Chai, Y. Q. Liu, C. G. Liu, In situ growth of Ni_xS_y controlled by surface treatment of nickel foam as efficient electrocatalyst for oxygen evolution reaction, *Appl. Surf. Sci.* 378 (2016) 15–21. <https://doi.org/https://doi.org/10.1016/j.apsusc.2016.03.197>.
- [76] N. K. Chaudhari, A. Oh, Y. J. Sa, H. Jin, H. Baik, S. G. Kim, S. J. Lee, S. H. Joo, K. Lee, Morphology controlled synthesis of 2-D Ni–Ni₃S₂ and Ni₃S₂ nanostructures on Ni foam towards oxygen evolution reaction, *Nano Converg.* 4 (2017) 7 (1-9). <https://doi.org/10.1186/s40580-017-0101-6>.
- [77] W. Zhou, X. J. Wu, X. Cao, X. Huang, C. Tan, J. Tian, H. Liu, J. Wang, H. Zhang, Ni₃S₂ nanorods/Ni foam composite electrode with low overpotential for electrocatalytic oxygen evolution, *Energy Environ. Sci.* 6 (2013) 2921–2924.
<https://doi.org/10.1039/C3EE41572D>.
- [78] R. B. Pujari, G. S. Gund, S. J. Patil, H. S. Park, D. W. Lee, Anion-exchange phase control of manganese sulfide for oxygen evolution reaction, *J. Mater. Chem. A*. 8 (2020) 3901–3909. <https://doi.org/10.1039/c9ta10553k>.
- [79] Y. R. Hong, S. Mhin, K. M. Kim, W. S. Han, H. Choi, G. Ali, K. Y. Chung, H. J. Lee, S. I. Moon, S. Dutta, S. Sun, Y. G. Jung, T. Song, H. S. Han, Electrochemically activated cobalt nickel sulfide for an efficient oxygen evolution reaction: Partial amorphization and phase control, *J. Mater. Chem. A*. 7 (2019) 3592–3602. <https://doi.org/10.1039/c8ta10142f>.
- [80] V. Ganesan, P. Ramasamy, J. Kim, Hierarchical Ni_{3.5}Co_{0.5}S₈ nanosheet-assembled hollow nanocages: Superior electrocatalyst towards oxygen evolution reaction, *Int. J. Hydrogen Energy*. 42 (2017) 5985–5992.
<https://doi.org/https://doi.org/10.1016/j.ijhydene.2016.12.060>.
- [81] Z. Yu, Y. Bai, S. Zhang, Y. Liu, N. Zhang, K. Sun, MOF-directed templating synthesis of hollow nickel-cobalt sulfide with enhanced electrocatalytic activity for oxygen evolution, *Int. J. Hydrogen Energy*. 43 (2018) 8815–8823.
-

<https://doi.org/10.1016/j.ijhydene.2018.03.154>.

- [82] J. Zhang, X. Bai, T. Wang, W. Xiao, P. Xi, J. Wang, D. Gao, J. Wang, Bimetallic nickel cobalt sulfide as efficient electrocatalyst for Zn–air battery and water splitting, *Nano-Micro Lett.* 11 (2019) 2 (1–13). <https://doi.org/10.1007/s40820-018-0232-2>.
- [83] C. Zequine, S. Bhoyate, K. Siam, P. K. Kahol, N. Kostoglou, C. Mitterer, S. J. Hinder, M. A. Baker, G. Constantinides, C. Rebholz, G. Gupta, X. Li, R. K. Gupta, Needle grass array of nanostructured nickel cobalt sulfide electrode for clean energy generation, *Surf. Coatings Technol.* 354 (2018) 306–312. <https://doi.org/https://doi.org/10.1016/j.surfcoat.2018.09.045>.
- [84] S. Shit, S. Chhetri, W. Jang, N. C. Murmu, H. Koo, P. Samanta, T. Kuila, Cobalt sulfide/nickel sulfide heterostructure directly grown on nickel foam: an efficient and durable electrocatalyst for overall water splitting application, *ACS Appl. Mater. Interfaces.* 10 (2018) 27712–27722. <https://doi.org/10.1021/acsami.8b04223>.
- [85] J. Jiang, C. Yan, X. Zhao, H. Luo, Z. Xuc, T. Mu, A PEGylated deep eutectic solvent for controllable solvothermal synthesis of porous NiCo₂S₄ for efficient oxygen evolution reaction, *Green Chem.* 19 (2017) 3023–3031. <https://doi.org/10.1039/C7GC01012E>.
- [86] S. Hyun, S. Shanmugam, Hierarchical nickel–cobalt dichalcogenide nanostructure as an efficient electrocatalyst for oxygen evolution reaction and a Zn–Air battery, *ACS Omega.* 3 (2018) 8621–8630. <https://doi.org/10.1021/acsomega.8b01375>.
- [87] W. Fang, D. Liu, Q. Lu, X. Sun, A. M. Asiri, Nickel promoted cobalt disulfide nanowire array supported on carbon cloth: An efficient and stable bifunctional electrocatalyst for full water splitting, *Electrochim. Commun.* 63 (2016) 60–64. <https://doi.org/https://doi.org/10.1016/j.elecom.2015.10.010>.
- [88] X. Cao, X. Zheng, J. Tian, C. Jin, K. Ke, R. Yang, Cobalt sulfide embedded in porous nitrogen-doped carbon as a bifunctional electrocatalyst for oxygen reduction and evolution reactions, *Electrochim. Acta.* 191 (2016) 776–783. <https://doi.org/https://doi.org/10.1016/j.electacta.2016.01.137>.
- [89] H. Qian, J. Tang, Z. Wang, J. Kim, J. H. Kim, S. M. Alshehri, E. Yanmaz, X. Wang, Y. Yamauchi, Synthesis of cobalt sulfide/sulfur doped carbon nanocomposites with efficient catalytic activity in the oxygen evolution reaction, *Chem. A Eur. J.* 22 (2016) 18259–18264. <https://doi.org/10.1002/chem.201604162>.
- [90] P. Ganesan, M. Prabu, J. Sanetuntikul, S. Shanmugam, Cobalt sulfide nanoparticles grown on nitrogen and sulfur codoped graphene oxide: an efficient electrocatalyst for oxygen reduction and evolution reactions, *ACS Catal.* 5 (2015) 3625–3637. <https://doi.org/10.1021/acscatal.5b00154>.
- [91] K. Prabakaran, M. Lokanathan, B. Kakade, Three dimensional flower like

cobalt sulfide (CoS)/functionalized MWCNT composite catalyst for efficient oxygen evolution reactions, *Appl. Surf. Sci.* 466 (2019) 830–836. <https://doi.org/https://doi.org/10.1016/j.apsusc.2018.10.015>.

- [92] K. Jayaramulu, J. Masa, O. Tomanec, D. Peeters, V. Ranc, A. Schneemann, R. Zboril, W. Schuhmann, R. A. Fischer, Nanoporous nitrogen-doped graphene oxide/nickel sulfide composite sheets derived from a metal-organic framework as an efficient electrocatalyst for hydrogen and oxygen evolution, *Adv. Funct. Mater.* 27 (2017) 1700451 (1-10). <https://doi.org/10.1002/adfm.201700451>.

CHAPTER 2

**Behind the method and
characterization techniques used**

Chapter 2: Behind the method and characterization techniques used

2.1. Materials and chemicals used.....	29
2.2. Introduction to thin films.....	29
2.3. Successive ionic layer adsorption and reaction (SILAR) method	31
2.3.1. <i>Theoretical background</i>	31
2.3.2. <i>Introduction to nucleation and film growth in SILR</i>	38
2.3.2 <i>Effect of preparative parameter</i>	41
2.3.3 <i>Advantages of SILAR</i>	43
2.4. Physicochemical characterization techniques.....	43
2.4.1. <i>X-ray diffraction (XRD)</i>	44
2.4.2. <i>Field emission scanning electron microscope (FE-SEM)</i>	48
2.4.3. <i>High-resolution transmission electron microscope (HR-TEM)</i>	51
2.4.4. <i>X-ray photoelectron spectroscopy (XPS)</i>	53
2.4.5. <i>Raman spectroscopy</i>	55
2.5. Electrochemical characterization techniques.....	57
2.5.1. <i>Cyclic Voltammetry (CV)</i>	59
2.5.2. <i>Linear sweep voltammetry (LSV)</i>	61
2.5.3. <i>Tafel slope</i>	62
2.5.4. <i>Electrochemical impedance spectroscopy (EIS)</i>	63
2.6 References.....	64

2.1. Materials and chemicals used

During the present study, various transition metal sulfides were deposited onto stainless steel (SS) substrates and tested for oxygen evolution reaction (OER). As received chloride precursors of cobalt (CoCl_2), nickel (NiCl_2) and manganese (MnCl_2) were used as cationic sources, while sodium sulfide (Na_2S) was used as an anionic source. Potassium hydroxide (KOH) was used to prepare electrolyte for electrochemical study. The solutions were made in double-distilled water (DDW) (resistivity of $18.2 \text{ M}\Omega \text{ cm}$).

2.2. Introduction to thin films

In the field of energy generation (e.g. solar cells), conversion (e.g. water splitting) and storage (e.g. batteries), material synthesis play an important role. In all the above-mentioned research fields, different materials are synthesized mainly in two forms: 1) bulk form (powder) and 2) thin film form. The use of electrically insulating binding agents hinders the actual electrochemical performance of powder material [1]. Therefore, the direct deposition of active material on the conducting backbone in thin film form has attracted many researchers.

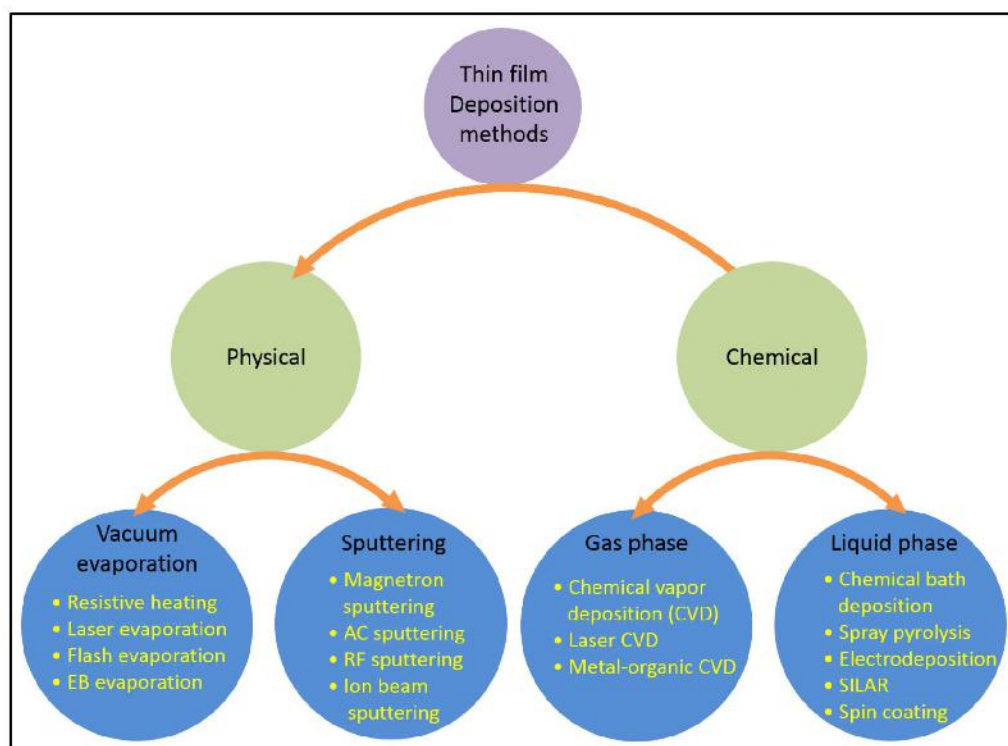
Thin film is a layer of material with a thickness of few micrometers. The process of thin film synthesis on any substrate is called a thin film deposition method. The properties of thin films are dependent on the method of deposition [2]. The broad classification of thin film deposition methods is listed in Figure 2.1. Based on the synthesis approach, thin films deposition methods are broadly classified into physical (top-up) and chemical (bottom-up) methods. The physical methods are subdivided into vacuum evaporation and sputtering. In vacuum evaporation, the pressure of the liquid (to be deposited) reduced below its vapor pressure, due to which the liquid gets

evaporate. The vacuum allows vapor particles to travel directly to the target substrate. Resistive heating, Flash evaporation, Electron beam evaporation, Laser evaporation, arc evaporation, etc. are examples of vacuum evaporation methods. While in the sputtering method, a slab of the material to be coated onto the substrates is electrically energized in a vacuum chamber in the presence of an inert atmosphere. The energizing process creates a self-sustaining plasma. The positively charged gas ions (gas atoms after losing electrons inside plasma) strike to atoms of the target material with sufficient kinetic energy. This forms a vapor stream that crosses the chamber and hits and sticks the substrate.

Glow discharge DC sputtering, Radiofrequency (RF) sputtering, Magnetron sputtering, AC sputtering, etc. are the examples of a sputtering method. The chemical deposition method is further categorized into Gas and liquid phase by the phase of the precursor. Chemical vapor deposition (CVD), laser chemical vapor deposition (LCVD), metal-organic chemical vapor deposition (MOCVD), etc are examples of gas-phase chemical deposition methods. In those methods, vapors of precursors react with a solid surface of the substrate to produce the desired deposition. Liquid phase chemical deposition is a unique soft solution process in which the thin film is formed on the substrate through a ligand-exchange reaction at different experimental conditions. An appropriate amount of precursors is dissolved into a solvent (either organic or inorganic) to prepare a precursor solution. Spray pyrolysis, electrodeposition, chemical bath deposition (CBD), successive ionic layer adsorption and reaction (SILAR), spin coating, sol-gel process, etc. are examples of liquid phase chemical deposition method. High working pressure and temperature, sophisticated instrumentation and their maintenance and high cost are some drawbacks of physical and gas-phase chemical deposition. Whereas, the solution phase chemical methods are

very simple, low cost and convenient for large area deposition of various materials. Therefore, chemical methods are widely used to prepare nanostructured materials for various applications.

Figure 2.1: Classification of thin film deposition methods.

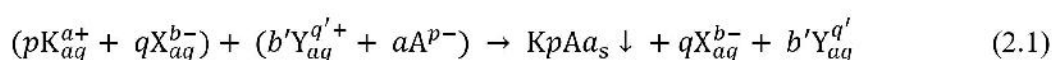


2.3. Successive ionic layer adsorption and reaction (SILAR) method

2.3.1. Theoretical background

Among the liquid phase chemical deposition method, SILAR is the renowned method for the deposition of chalcogenide thin films. It is also known as the modified version of CBD method. In CBD method the cations and anions are present in the same chemical bath while in SILAR method separate chemical baths are prepared from cationic and anionic precursors. SILAR is simple, low energy consumption and hence low-cost method useful for the preparation of uniform, well adherent and large-area thin films.

In 1985, Ristov et. al. [3] reported a new chemical method for the deposition of Cu₂O thin films. In their study, a previously cleaned glass substrate was successively immersed in a cold complex solution of 3Cu₂S₂O₃·2Na₂S₂O₃ and a hot solution of NaOH. After a certain number of successive immersions, brown colored Cu₂O is deposited on a glass substrate. The name SILAR was first given to this method in 1985 by Nicolau [4]. SILAR method is wholly based on the adsorption of cations and their reaction with secondly adsorbed anions from the solutions and additional rinsing with deionized water after each immersion. The SILAR method is aimed to grow K_pA_a type water insoluble compounds in thin film form. For this suppose, K_pX_q (eg. CoCl₂) and Y_b'A_a (eg. Na₂S) are used as cationic and anionic precursors. This growth takes place by a heterogeneous chemical reaction at the solid solution interface between adsorbed cations, pK_a⁺ and anions, aK_p⁻, following the reaction



with $ap = bq = b'q'$

Where, 'K' represents cation (Co²⁺, Mn²⁺, Ni²⁺, etc.), 'p' represents the number of cations, a represents the numerical value of charge on cation, 'X' is an ion in cationic precursors having negative charge (X = SO₄²⁻, Cl²⁻, NO₃²⁻ etc.) 'q' represents the number of X in cationic precursors and 'b' is the numerical value of charges on X. b' is the number of Y in the anionic solutions. q' is the numerical value of charge on Y, 'Y' is the ion which is attached to chalcogen ion, A represents the anion (O-, OH-, S, Se and Te), 'a' is the number of anions.

In detail, the SILAR method works in four different steps, adsorption, 1st

rinsing, reaction, 2nd rinsing. Figure 2.2. represents a typical experimental setup of SILAR in 4 steps.

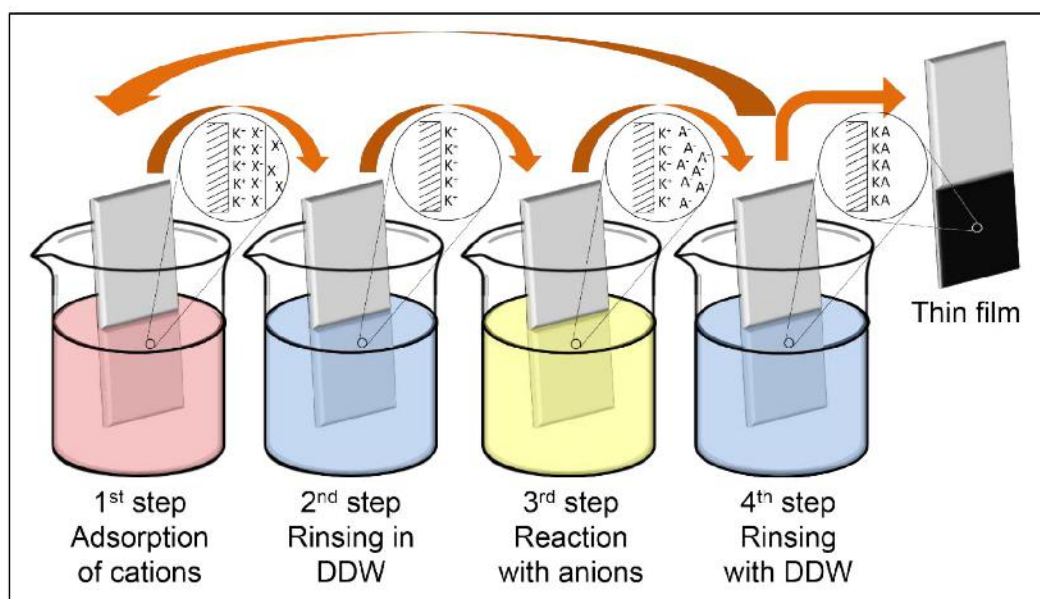


Figure 2.2: Schematic representation of SILAR method.

The first and third beakers contain the solution of cationic and anionic precursors, respectively, while second and fourth beaker contains DDW for rinsing purpose. During the deposition procedure, the substrate is successively immersed in each beaker one by one starting from 1st.

1) Adsorption: This is the 1st step of SILAR process. When substrate dipped into cationic solution, different layers of charges are developed on its surface (Figure 2.3). The closest to the substrate, a very thin layer of solvent molecules (water molecules in present case) is formed and it is called as inner layer. This inner layer sometimes contains other species called specifically adsorbed anions [5].

The locus of the electrical centers of these specifically adsorbed anions is called as inner Helmholtz plane (IHP). The solvated (solvated ions are surrounded or complexed by solvent molecules) cations present in solution approach to the substrate

and get adsorbed on it to equilibrium the surface charges.

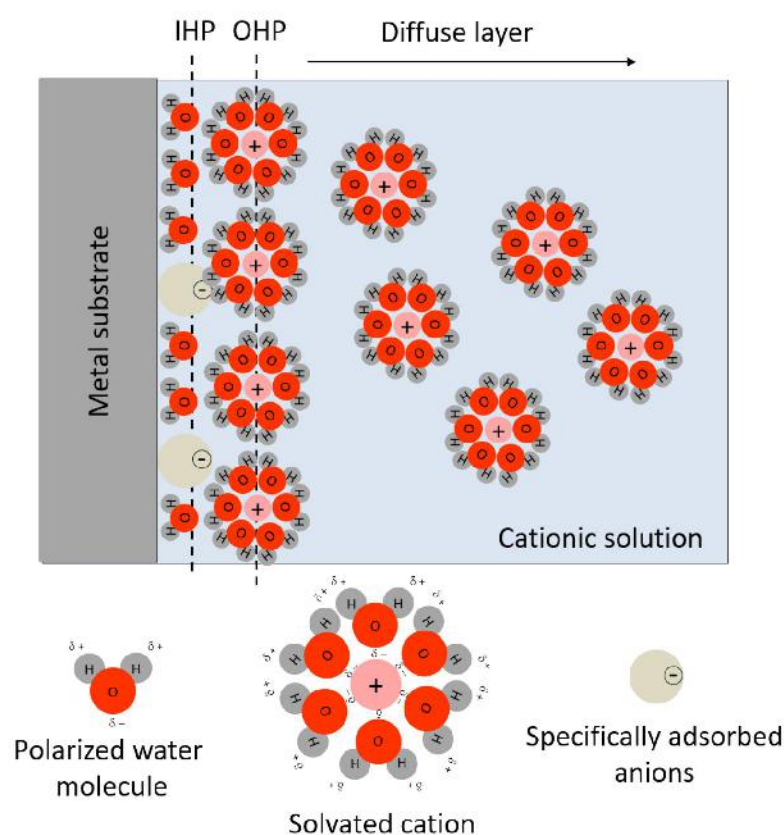


Figure 2.3: Schematic of formation of Helmholtz double layer during 1st step of SILAR.

This adsorption is possible due to the chemical attractive forces between them [6]. The locus of centers of these nearest solvated cations is called the outer Helmholtz plane (OHP). From OHP to the bulk of solution nonspecifically adsorbed solvated cations are present. This layer of nonspecifically adsorbed solvated cations is called as a diffuse layer. The thickness of this diffuse layer depends on the surface charge of the substrate.

2) 1st rinsing: To prevent the homogeneous precipitation from the instantaneous reaction with anion in 3rd step, the loosely bounded and excess solvated cations in the

Helmholtz layer are removed by rinsing in DDW in this step (2nd) (Figure 2.4). This is the advantage of SILAR method over CBD while depositing thin film of material.

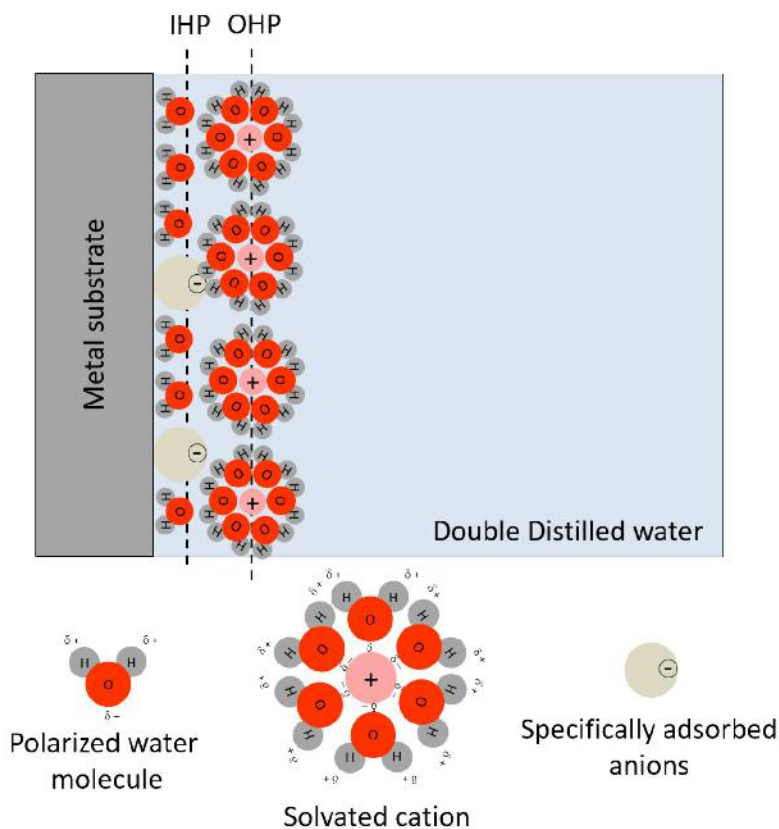


Figure 2.4: Schematic of rinsing of excess ions during 2nd step of SILAR.

In the CBD method both anions and cations are present in single chemical bath therefore one could not avoid the unnecessary homogeneous precipitation. While in SILAR method there is no possibility of homogeneous precipitation until substrates are properly rinsed.

3) Reaction: In this step, the previously adsorb cations and newly adsorb anions reacts and forms a water-insoluble solid compound as shown in Figure 2.5. Some of the counter ions from anionic solution also get attached to this solid compound.

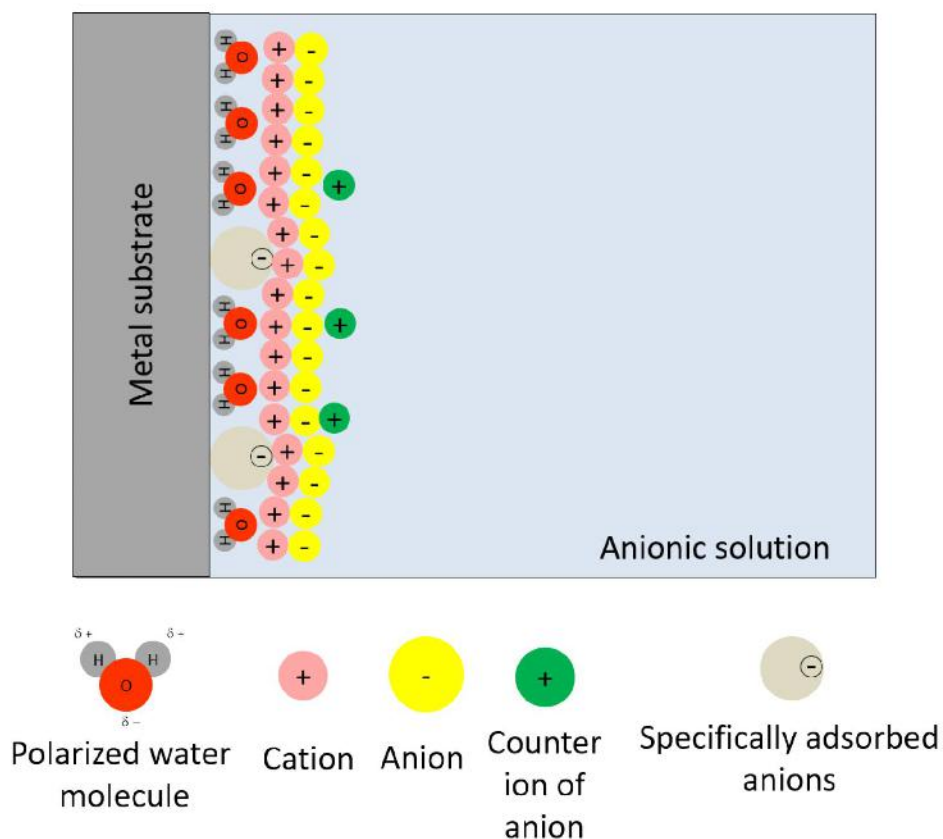


Figure 2.5: Schematic of formation of water insoluble solid compound during 3rd step of SILAR.

4) 2nd rinsing: This is the last step of SILAR method in which the excess and unreacted species and reaction by-products are removed. At the end of this step, a monolayer of targeted material gets deposited on the substrate as seen in figure 2.6.

These four steps combinedly complete one SILAR deposition cycle. After a certain number of cycles, enough material is deposited on the substrate in the form of uniform and adherent thin film. The quality of the thin film in SILAR method (in terms of adherence, uniformity, etc.) is strongly influenced by the adsorption, reaction and rinsing times used. In the present study, adsorption, reaction and rinsing time in each chapter were experimentally optimized via various trials to get uniform and adherent deposition.

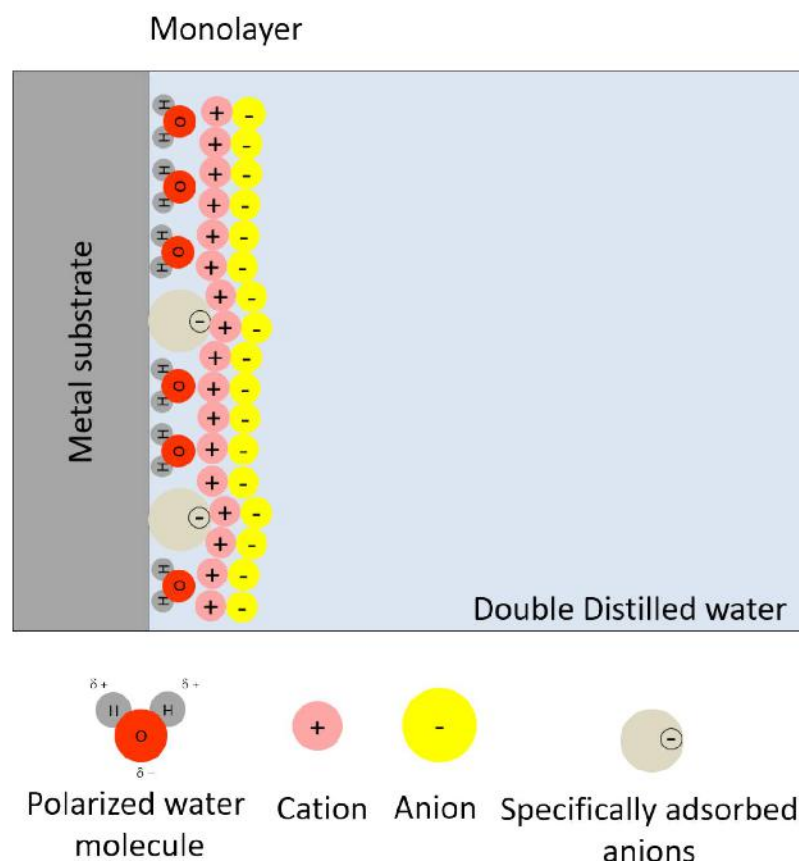


Figure 2.6: Schematic of formation of a monolayer of targeted material during 4th step of SILAR.

The SILAR deposition method can be operated by three ways,

- 1) Manual operation: The immersion of the substrate in each beaker is done manually. This is a time-consuming operation.
- 2) Computer-based operation: The computer program monitors the vertical and translational movement of the arm to which substrates are attached.
- 3) Microprocessor-based: The substrates are attached to a horizontal robotic arm in the vertical direction and a microprocessor governs its movements in vertical and translational movements. Nowadays microprocessor based SILAR equipment is popular among researchers due to its easy operation settings, and feasibility for the

binary, ternary chalcogenide as well as composite materials synthesis. Microprocessor-based SILAR machine (shown in figure 2.7) from Holmarc Optomechatronics PVT. LTD. is used to deposit thin films electrodes.



Figure 2.7: Photograph of SILAR machine used to deposit thin film electrodes in the present study.

2.3.2. Introduction to nucleation and film growth in SILAR

Nucleation:

Nucleation is the first step in the deposition of material via a chemical method. There are two types of nucleation in chemical deposition methods namely, homogeneous and heterogeneous nucleation. The homogeneous nucleation occurs in the solution while heterogeneous nucleation occurs on the surface of substrate. In SILAR method, the cationic and anionic precursor solution are kept separate and the

substrate is rinsed after each adsorption and reaction steps, there is very less possibility of homogeneous nucleation. Hence, in SILAR method the material is mainly deposited via heterogeneous nucleation.

The surface of metal substrate offers various nucleation sites for deposition as shown in Figure 2.8. On the flat metal surface, a single atom signified as an adatom; a combination of several adatoms known as an adatom cluster. Missing of single atom assigned as vacancy and several vacancies combinedly called as vacancy cluster. Steps and kink sites are important for crystal growth. The addition and removal of atoms at the kink site create new kink sites [7].

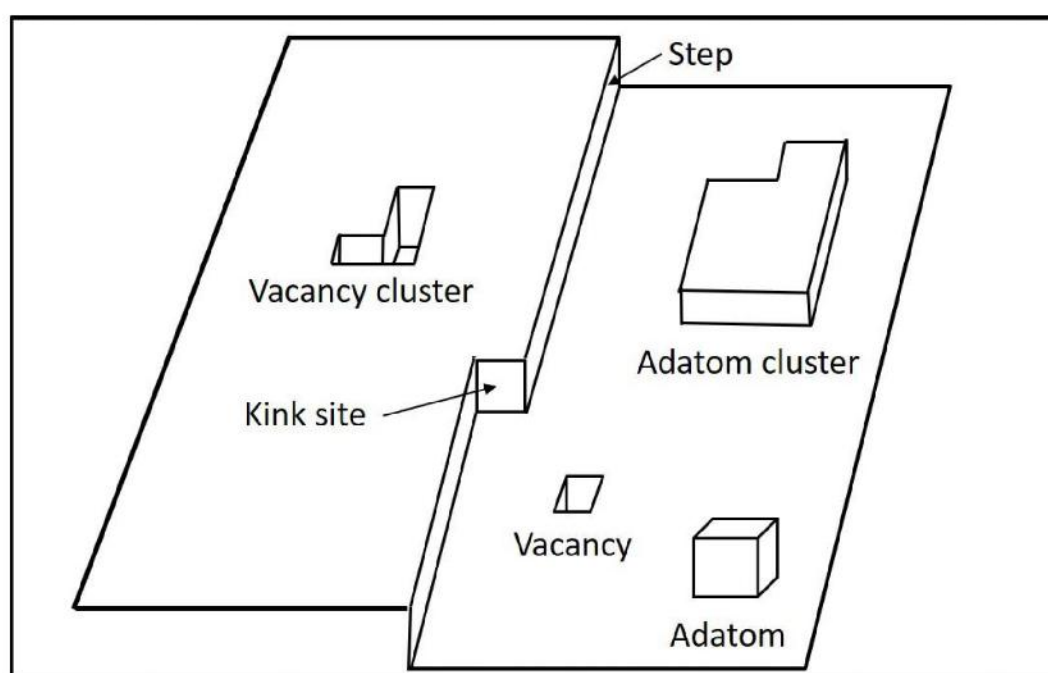


Figure 2.8: Schematic of substrate surface with different types of nucleation centers.

In SILAR method the water insoluble species deposited on substrate at the end of 1st SILAR cycle, acts as nucleation centers for further growth of material. Hence in SILAR method, adatoms mainly act as nucleation centers.

Film growth:

There are three primary mechanisms by which thin film grow on the surface of metal substrate via nucleation sites. Since the monolayer of water insoluble compound formed in 1st SILAR cycle act as nucleation centers, in SILAR method film starts to grow after 1st or 2nd deposition cycle.

- i) Volmer–Weber mechanism: In Volmer–Weber growth mechanism (Figure 2.9 (a)), adatom–adatom interactions are stronger than those of the adatom with the surface, leading to the formation of three-dimensional adatom clusters or islands. The growth of these clusters, along with roughening, will cause rough multi-layer films to grow on the substrate surface [8].

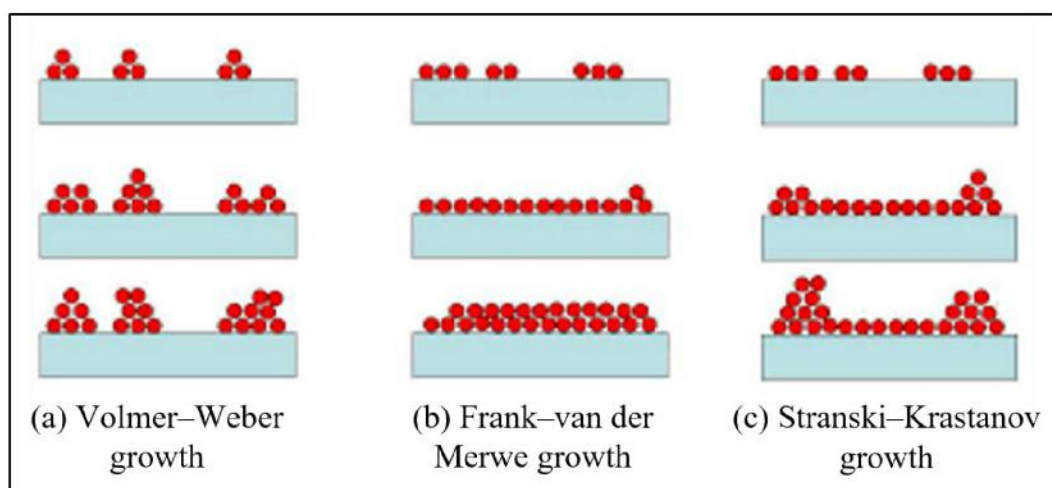


Figure 2.9: Schematic of three growth mechanisms.

- ii) Frank–van der Merwe mechanism: Frank–van der Merwe growth mechanism (Figure 2.9 (b)) is one of the three primary modes by which thin films grow at a crystal surface or interface. It is also known as 'layer-by-layer growth'. In this kind of growth atoms (to be deposited) are more attracted to the substrate than to each other, which is in contrast to the layer-plus-island or Stranski–Krastanov growth model [9].

iii) Stranski–Krastanov mechanism: Stranski–Krastanov growth mechanism (Figure 2.9 (c)) also known as 'layer-plus-island growth'. In this growth model two-dimensional nucleation occurs up to one or more atomic layers of the novel phase (formation of few monolayers); thereafter a three-dimensional nucleation process starts (island formation) [10].

The kind of growth mechanism followed during the deposition of a material depends on the different preparative parameters used.

2.3.3. Effect of preparative parameters

In SILAR method, the growth kinetic of thin film depends on different parameters such as complexing agent, temperature, concentration of solution, adsorption and reaction time, rinsing time, and Composition of reaction solution (cationic). The effect of various deposition parameters on film growth are discussed below:

i) Complexing agent

A complexing agent is a substance capable of forming a complex compound with another material in solution. Ammonia (NH_3), Ethylenediaminetetraacetic acid (EDTA), Triethylamine (TEA), Polyvinyl alcohol (PVA), Polyvinylpyrrolidone (PVP), etc. are the common complexing agents used in chemical deposition methods. Ions of the complexing agent bind the simple metal ions forming complex ions. As reaction precedes, metal ions are released for the reaction with other ions. Hence, complexing agent maintains the concentration of metal ions during a chemical reaction. The slow release of metal ions in SILAR method leads to a slow growth rate of the film. Hence, by using complexing agent growth kinetics of film can be controlled.

ii) Temperature

The dissociation of a complex compound depends on the temperature. At the higher temperature, the dissociation is greater which gives the higher concentration of cations and resulted in a higher rate of deposition.

iii) Concentration of solution

The surface density of adsorbed ions depends on the concentration of precursor solution. Therefore, for a high concentration of solutions thicker films can be obtained while for low concentration thin and non-uniform film can be obtained. This indicates that at lower concentrations there is a lack of required number of ionic species for the better quality of film.

iv) Adsorption and reaction time

Adsorption and reaction time plays important role in the formation of thin film. As the adsorption time is greater than that of reaction time the film formation takes place by the assorted reaction it results in higher terminal thickness. Equal adsorption and reaction time, result in a consistent reaction. Consistent growth provides uniform film formation. The effect of adsorption and reaction time on film growth is well discussed by Shinde et al. [11].

v) Rinsing time

Rinsing between every immersion is significant to avoid precipitation in the reaction bath. In a rinsing bath, the loosely bounded species peel off from the substrate surface. Sufficient rinsing time can provide a good quality film.

vi) Composition of reaction solution (cationic)

The film growth can be affected by changing the composition of cations in the solution. The process of homogeneous and heterogeneous nucleation can be altered by changing the bath composition of cationic precursors.

2.3.4. Advantages of SILAR method

Along with the simplicity, SILAR method has several advantages as given below:

- Any foreign element can be doped into thin film material by simply adding it into the cationic solution.
- In many applications, the thickness of thin film plays an important role and it can be easily controlled in SILAR method by changing the deposition cycles.
- Thin film can be deposited on any substrate irrespective of its material and dimension.
- There is no chance of oxidation or corrosion of metallic substrates during deposition, as it is carried out at or near room temperature.
- It does not require sophisticated instrumentation.
- It is a very convenient method to synthesize composites of transition metal based and carbon based materials

2.4. Physicochemical characterization techniques

The effective performance of a material is strongly correlated with its different physicochemical properties. Therefore, the characterization of material through different techniques and careful analysis of obtained results are important tasks in the research field. This will lead to decide a suitable material for a particular application. Also, one can define the required qualities of material and find ways to improve them. The as-deposited thin film electrodes in the present study were analyzed through different material characterization techniques. The comprehensive

description of the basic principle, instrumentation and working of these techniques are covered in this section.

2.4.1. X-ray Diffraction (XRD)

In the field of materials science, X-ray diffraction is considered a very primary and rapid characterization technique for material confirmation via matching with the available previous database [12]. The technique also provides information on unit cell dimensions. The technique is also used to measure crystallite size and to calculate lattice strain, chemical composition, state of ordering and to determine phase diagrams as well.

Basic principle

When the monochromatic X-rays incident on a crystalline sample with an angle of incidence θ , the X-rays get diffracted from parallel lattice planes separated by the interplanar distance, d . When the intensity of diffracted X-rays measured as a function of scattering angle, a diffraction pattern is obtained. According to Bragg's condition (Figure 2.10), when the path difference becomes equal to the integral multiple of the wavelength of incident X-rays, the diffracted X-rays interfere constructively.

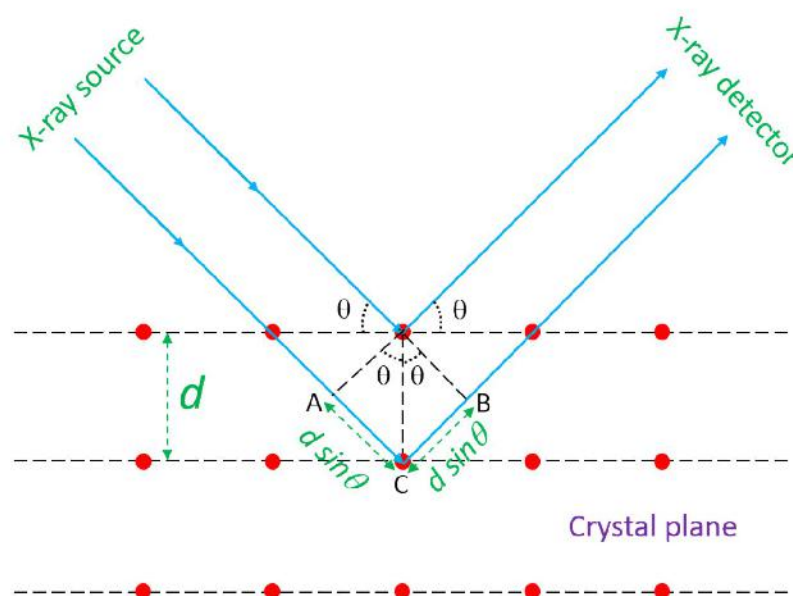


Figure 2.10: Bragg's diffraction.

At such conditions, peaks obtained in diffraction patterns are known as Bragg peaks.

$$n\lambda = \text{path difference} = ACB$$

$$\text{Path difference between two waves} = ACB = 2d \sin \theta$$

$$\text{therefore, } n\lambda = 2d \sin \theta$$

Where, ' λ ' is the wavelength of X-ray and ' n ' is the order of diffraction.

Instrumentation and working

A fully automated X-ray diffractometer includes three main parts; an X-ray tube/source, sample stage and X-ray detector (Figure 2.11). To detect X-rays at various diffraction angles, the X-ray tube rotates in a clockwise direction with angle θ while X-ray detector rotates in an anti-clockwise direction with angle 2θ .

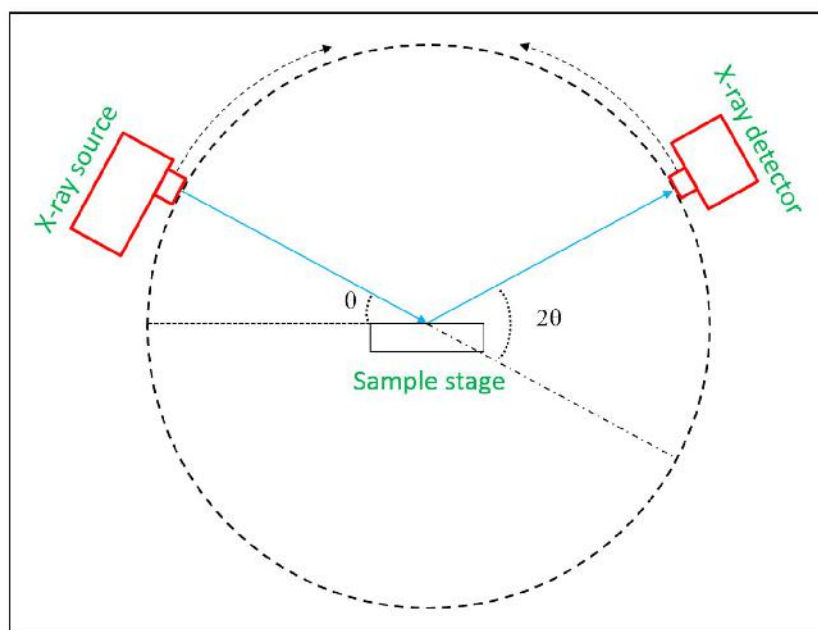


Figure 2.11: The schematic of the X-ray diffractometer.

The X-ray tube is the heart of XRD instrument which is either a ceramic or glass container that has a tungsten filament that acts as a cathode. The schematic of the X-ray tube is shown in Figure 2.12. This cathode filament emits electrons that pass through a vacuum. The accelerated electrons then travel to the target material where electrons bombard the atomic structure of the elements of the targeted material causing the secondary electrons to be kicked out of the inner electronic shells. The electrons from higher energy levels drop into lower energy levels to fill the space caused due to secondary electrons. However, to go from higher to lower energy levels, electrons must lose some energy. This energy is released in the form of X-rays and these X-rays are called characteristic X-rays of target material because the characteristics of generated X-rays depend on the energy level of the atom of the target material. Typically, the target material is copper (Cu) and the characteristic radiation is either K_{α} or K_{β} .

The X-rays generated by an X-ray tube before the incident on the sample

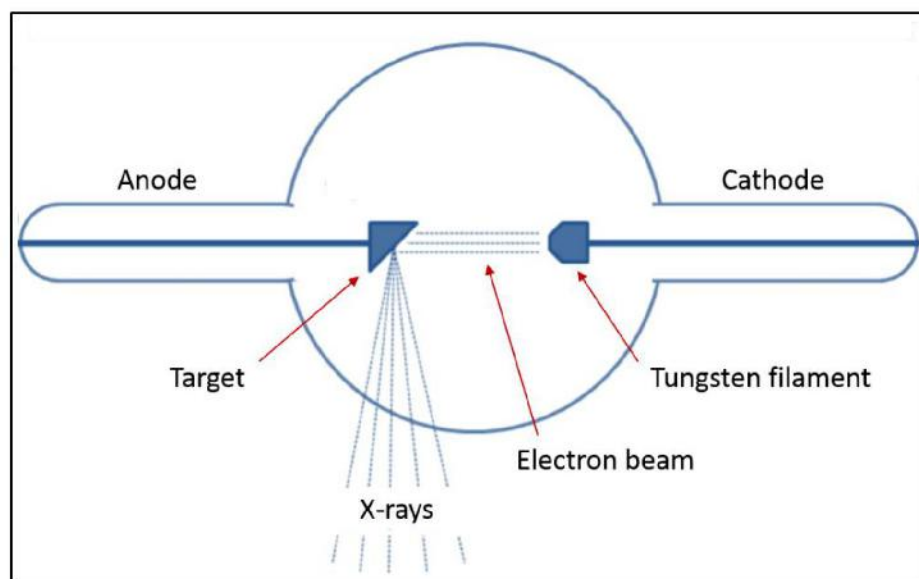


Figure 2.12: Schematic of the X-ray tube.

goes through a monochromator. The monochromator absorbs K_{β} and white radiations and allows only K_{α} radiations through. These allowed X-rays are collimated and directed onto the sample. For a crystalline sample, it can be expected that there are a significant number of crystallites present to fulfill the Bragg condition for constructive interference of reflected waves. Therefore, the X-ray source and detector rotate, and the intensity of reflected X-rays is recorded as a function of diffraction angle 2θ . A detector records and processes the X-ray signals and converts them to a count rate which is then output to a printer. Each Bragg peak represents a certain lattice plane and therefore, can be characterized by a Miller index.

In the present study, the XRD patterns of as-deposited thin film electrodes are recorded using PANalytical Empyrean diffractometer with Cu K_{α} characteristic radiations ($\lambda = 1.5406 \text{ \AA}$) operated at 40 kV in $\theta/2\theta$ mode, at a Cooperative Center for Research Facilities (CCRF), Chonnam National University, South Korea.

2.4.2. Field Emission Scanning Electron Microscope (FE-SEM)

Field emission scanning electron microscope (FESEM) works with electrons instead of light. FESEM provides topographical and elemental information at magnifications of 10x to 300,000x, with virtually unlimited depth of field. FESEM produces clear and less electrostatically distorted images.

Basic principle

The primary electrons liberated from a field emission source are accelerated in the electric field. Using electromagnetic lenses, a narrow beam is produced by focusing these primary electrons. The beam is allowed to strike the sample. This causes the emission of secondary electrons from the sample. These secondary electrons carry the topographical information of the sample. By processing these electrons detector generates an electric signal which is further amplified and transformed into an image.

Instrumentation and working

The schematic diagram of the FESEM instrument is shown in Figure 2.13. An electron gun, an anode (accelerator), magnetic lenses, sample holder and detector are the main parts of a FESEM instrument. The whole assembly is mounted on a desk. Sample preparation is also one of the parts of the FESEM characterization technique. Before mounting on a special holder, the samples are first made conductive by coating them with 1.5-3.0 nm thin layer of platinum or gold [13].

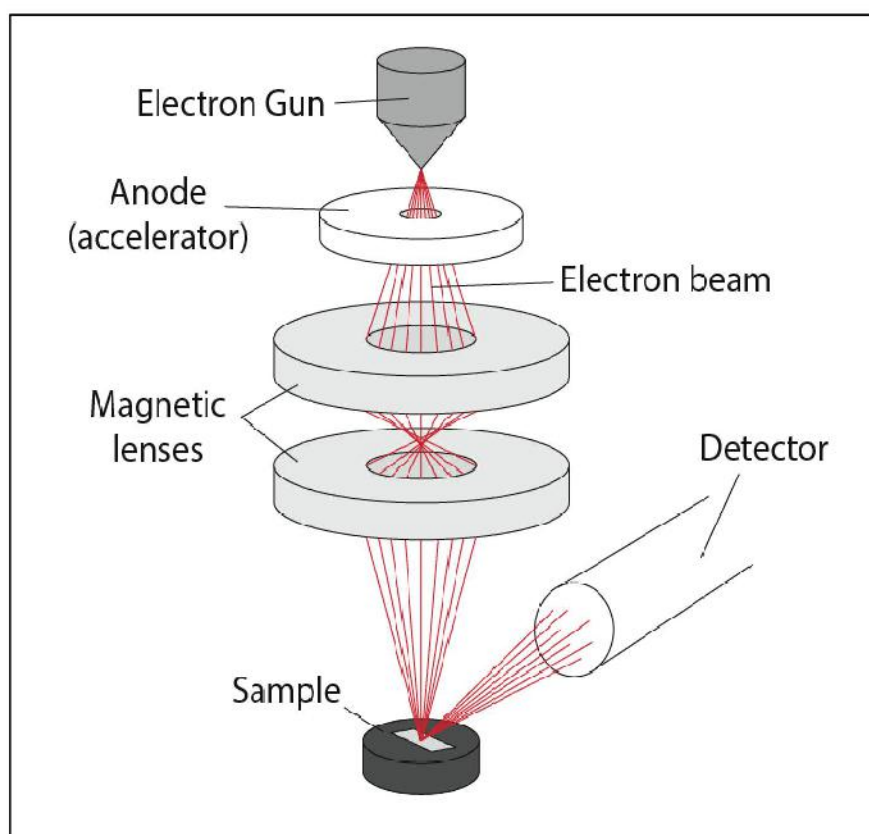


Figure 2.13: Schematic of FESEM instrument.

In FESEM, high-energy electrons (also called primary electrons) are generated by heating a thin and sharp tungsten needle (cathode). The voltage difference between anode and cathode allows generated electrons to accelerate towards the sample. The electron beam is focused by the electromagnetic lenses to a tiny sharp spot. The pre-coated sample is mounted on the special holder and inserted onto the high vacuum part of the microscope through an exchange chamber. The FESEM is always performed in a high vacuum to avoid the interaction of high-energy electrons with gas molecules in order to obtain high resolution. Once the focused electron beam bombards on the surface of the sample, it penetrates the sample up to a few microns and interacts in different ways. After the interaction, primary electrons lose their energy inside the sample, due to this, different types of electrons are produced as shown in Figure 2.14 [14]. The scattering of electrons and volume of interaction

depends on the atomic number, the concentration of atoms of sample and the energy of primary electrons. The high energy of primary electrons increases interaction volume and scattering process. While the high concentration of atoms and the atomic number will decrease the interaction volume and scattering.

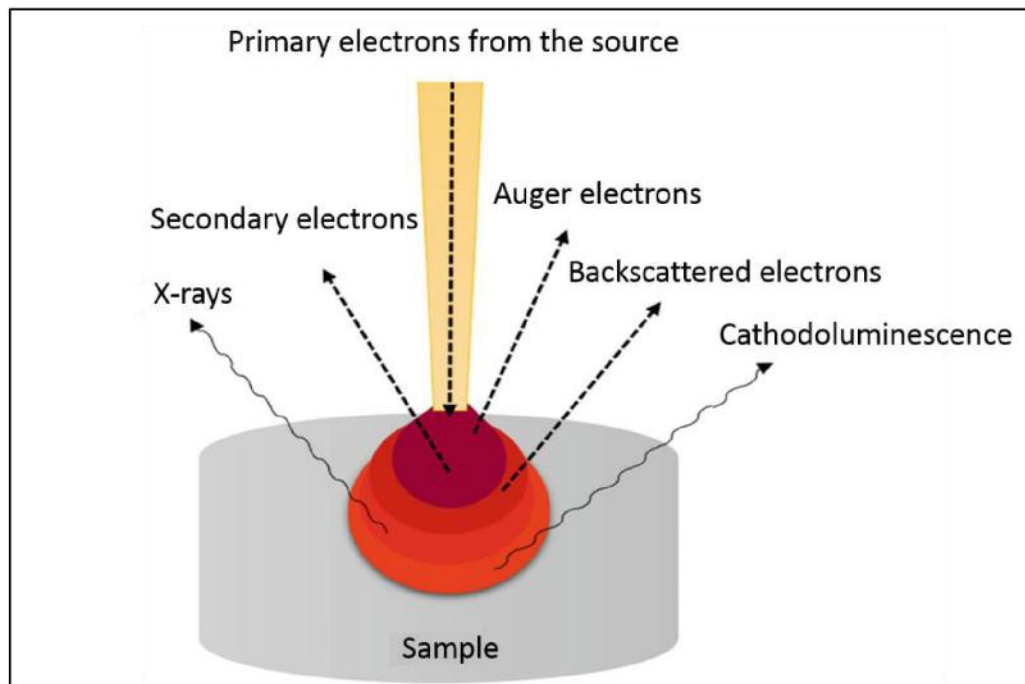


Figure 2.14: Ray diagram for the emission of different types of electrons after the interaction of primary electrons from source with sample.

All these signals are gathered by a detector and separated based on their energy values. The backscattered and secondary electrons are used for the creation of a sample image by amplifying and transforming the signals. When primary electrons interact with electrons at the inner shell and knock it out, the electron from a higher energy level jumps to lower energy by losing some energy. This extra energy is loosed in the form of X-rays. Therefore, each element in the sample produces a characteristic X-ray. All these characteristic X-rays from all elements are used to identify the elemental composition of the sample by energy-dispersive X-ray spectroscopy (EDX) coupled to the FESEM instrument.

In the present study, FESEM and EDX are performed on Philips SEM-XL30S microscope (Netherlands) coupled with an energy-dispersive X-ray spectroscopy (EDX) analyzer.

2.4.3. High-resolution Transmission Electron Microscope (HR-TEM)

High-resolution transmission electron microscopy (HR-TEM) is another important technique used as a materials characterization tool that involves passing an electron beam through the sample. It provides information about samples at very high resolution and down to atomic levels, such as morphology, size distribution, crystal structure, interplanar distance, elemental distribution, etc. The main difference in FESEM and HR-TEM is the speed of primary electrons. The electrons in HR-TEM have a much higher speed than in FESEM. Also, the electrons in case FESEM bounce off the sample while in HR-TEM it gets transmitted through the sample.

Basic principle

The high-speed electrons travel in a vacuum chamber and pass through the ultra-thin sample casted on a TEM grid and a charge-coupled device (CCD) camera is used for focused imaging.

Instrumentation and working

There is an electron gun on the top like FESEM which emits electrons (Figure 2.15). The electromagnetic lenses (magnetic condensing lens) help electrons to achieve high speed in the vacuum chamber. High-speed electrons hit the ultra-thin sample and partially transmitted through it. These transmitted electrons carry information about the structure of that sample. But this information is not enough to be recognized by CCD.

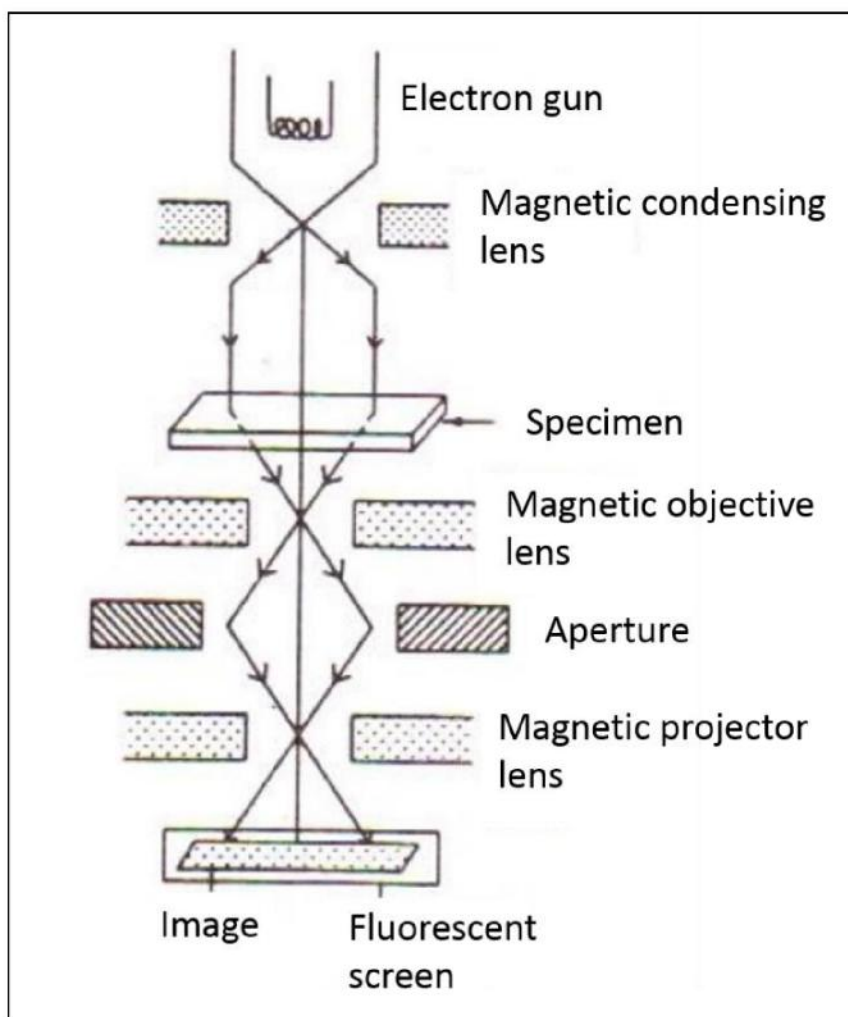


Figure 2.15: Schematic of HR-TEM.

Therefore, the signals from these transmitted electrons are amplified by the second set of lenses (magnetic objective and projector lenses). The CCD processes these signals and projects them on the computer screen. In HR-TEM the image quality depends on the scattering effect therefore, the sample preparation for HR-TEM must be done very well. A metal grid is used to support the sample. A metal grid is a flat disc with a mesh used to support a very thin section of the sample. Figure 2.16 (a) shows the grid holder and Figure 2.16 (b) shows the copper grid used to support the sample in the present study.

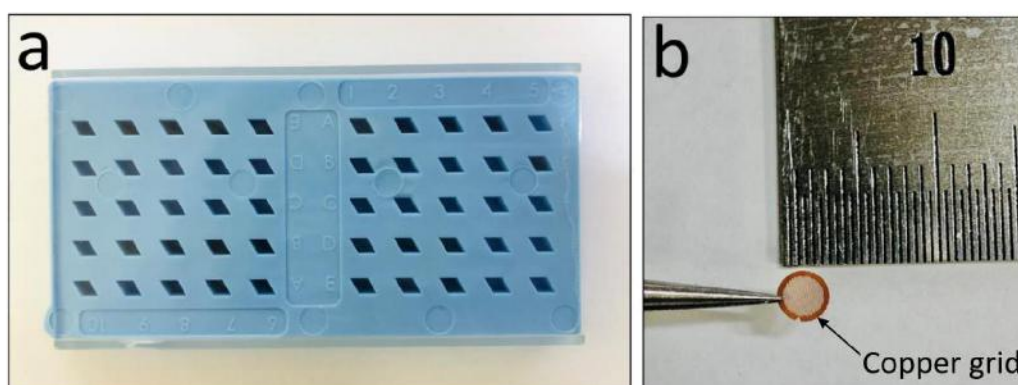


Figure 2.16: Photographs of a) TEM grid holder and b) copper grid.

To prepare a powder sample ready for HR-TEM measurement, a small quantity of powder is dispersed in a low boiling point solvent. Then ultrasonicate the solution for ~20 mins. Take a small drop of solution and carefully put it on the grid.

In the present study, the High-resolution transmission electron microscopy (HR-TEM) images and selected area diffraction (SAED) patterns are collected through JEOL ARM-200F (JEOL, U.S.) field-emission TEM. To prepare the sample, a small amount of powder is scratched from deposited thin film electrodes.

2.4.4. X-ray Photoelectron Spectroscopy (XPS)

X-ray photoelectron spectroscopy (XPS) is a chemical analysis technique mainly used for analyzing the surface composition of a material and oxidation state of elements present in it. The XPS can characterize only 1-10 nm depth of the sample. XPS technique is based on the photoelectric effect described by Einstein, which states that when electromagnetic radiation hits a material, electrons are emitted. These emitted electrons are also called photoelectrons.

Basic principle

When an incident X-ray has sufficient energy, it will be absorbed by an atom and by the phenomenon of the photoelectric effect, an inner shell electron will be ejected as demonstrated in Figure 2.17. The kinetic energy of photoelectrons is collected. As the energy of an incident X-ray is known, the binding energy of photoelectron is calculated by the below formula:

$$E_{binding} = E_{photon} - (E_{kinetic} + \varphi) \quad (2.2)$$

where, φ is the work function of the element.

By measuring the count of photoelectrons as a function of binding energy, the composition of the sample and the various oxidation states of elements present in it can be calculated.

Instrumentation and working

In XPS an X-ray source generates X-rays (typically $MgK\alpha$ and $AlK\alpha$) which are monochromatized using a monochromator in a high vacuum. These X-rays incident on the sample and excite the electrons inside the atoms present on the surface of the sample. These photoelectrons go to the electron detector where the detector counts the incoming electrons as well as the kinetic energy of these electrons. Finally, this kinetic energy is represented in the form of a spectrum where particular energy represents an element present in the sample.

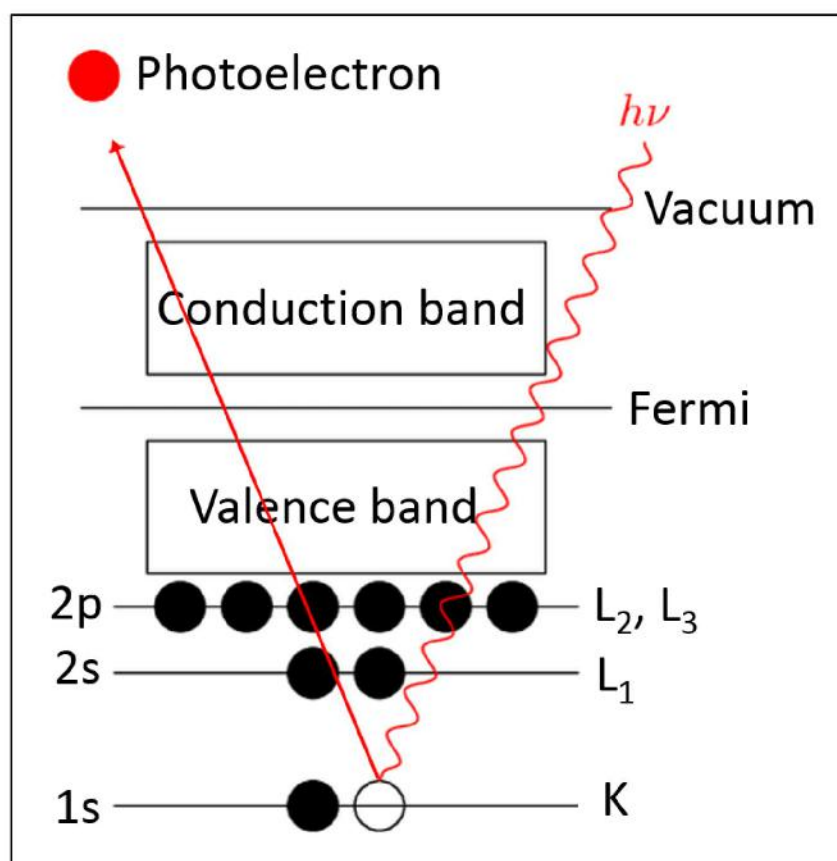


Figure 2.17: Atomic model of the working principle of XPS.

The X-ray photoelectron spectroscopy (XPS, K-alpha XPS System, Thermo Fisher Scientific, U.K.) is used in the present study.

2.4.5. Raman Spectroscopy

When a sample is exposed to monochromatic light in the visible region, the sample absorbs light and a major portion of light gets transmitted through the sample. However, a minute part of the light gets scattered by the sample in all directions. The incident and scattered light have a particular frequency. When the scattering is observed at the right angle to the incident beam 99% of the scattered light has similar to incident light, this kind of scattering is called Rayleigh scattering. Only 1% light

scattered with different frequencies than incident frequency. This is called Raman scattering.

Working principle

Raman scattering is a two-photon process. Electrons have different vibrational levels which are defined by specific energy differences (Figure 2.18). When an incident monochromatic light interacts with an electron in the sample, the electron absorbs energy from an incident photon and goes to a virtual state of energy. The electron falls back to an energy level by losing energy. When the energy lost equal to the energy of the incident photon, the electron falls back to its initial level and loses one photon. Hence the molecule doesn't have any Raman active modes. This secondary photon has the same frequency as the incident photon and Rayleigh scattering occurs. However, sometimes electrons while losing energy from the virtual state can fall back to a different vibrational level.

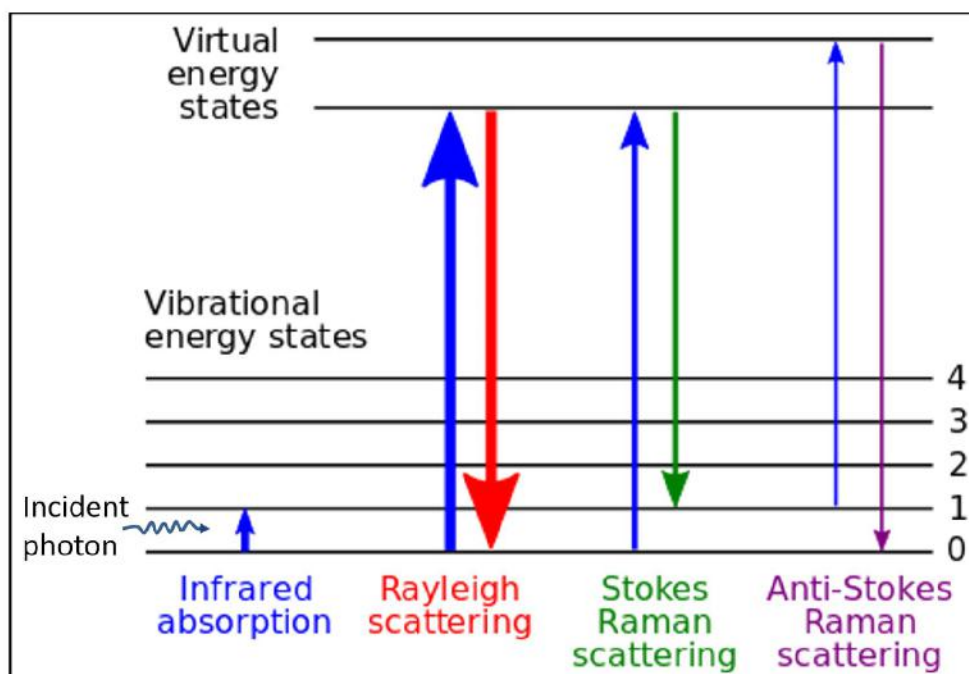


Figure 2.18: Energy-level diagram showing the states involved in Raman spectroscopy.

In this case, the energy loss by the electron is different than the energy absorbed from the incident photon. As a result, the emitted photon has energy different than the incident photon. In this case, the frequency of the emitted photon is not equal to the incident photon. This gives the Raman scattering. Depending on the final vibrational level of electron Raman scattering is separated into Stokes line and anti-Stokes lines. When the frequency of the scattered photon is less than the incident photon, Stokes lines are observed on the Raman spectrum. This happens when an electron absorbs energy. Oppositely, when the frequency of the emitted photon is greater than the incident photon, anti-Stokes lines are observed. Hence, the energy is released by the electron.

The Raman shift $\Delta\nu$ is positive for Stokes and negative for anti-Stokes and is a characteristic feature of material undergoing Raman shift. The Raman spectrum gives the molecular fingerprint and it is different for different molecules. By studying the Raman spectra one can identify the rotational levels and thus a particular molecule. This will help to analyze the sample qualitatively. Similarly, the intensity of a particular Raman line helps to determine the concentration of a molecule in the sample.

A confocal Raman spectrometer (JSACO NRS-5100, Japan) equipped with an aberration-corrected Czerny-Turner monochromator utilizing a laser excitation source (λ –532 nm) is employed in the present study.

2.5. Electrochemical characterization techniques

Electrochemical techniques can be divided into three main groups depending on whether we control the potential, the current or the charge, leaving impedance techniques in a fourth group. In this section, the main electrochemical techniques used

in the present study are briefly explained.

All the electrochemical studies reported in chapters 3rd, 4th, and 5th, were performed in a conventional three-electrode system (a photograph of the lab set up of three-electrode system is shown in Figure 2.19). The saturated calomel electrode (SCE) and platinum (Pt) wire were used as reference and counter electrodes, respectively. SILAR deposited thin film electrocatalysts were assigned to be working electrodes. The freshly prepared 1 M KOH is used as an electrolyte.

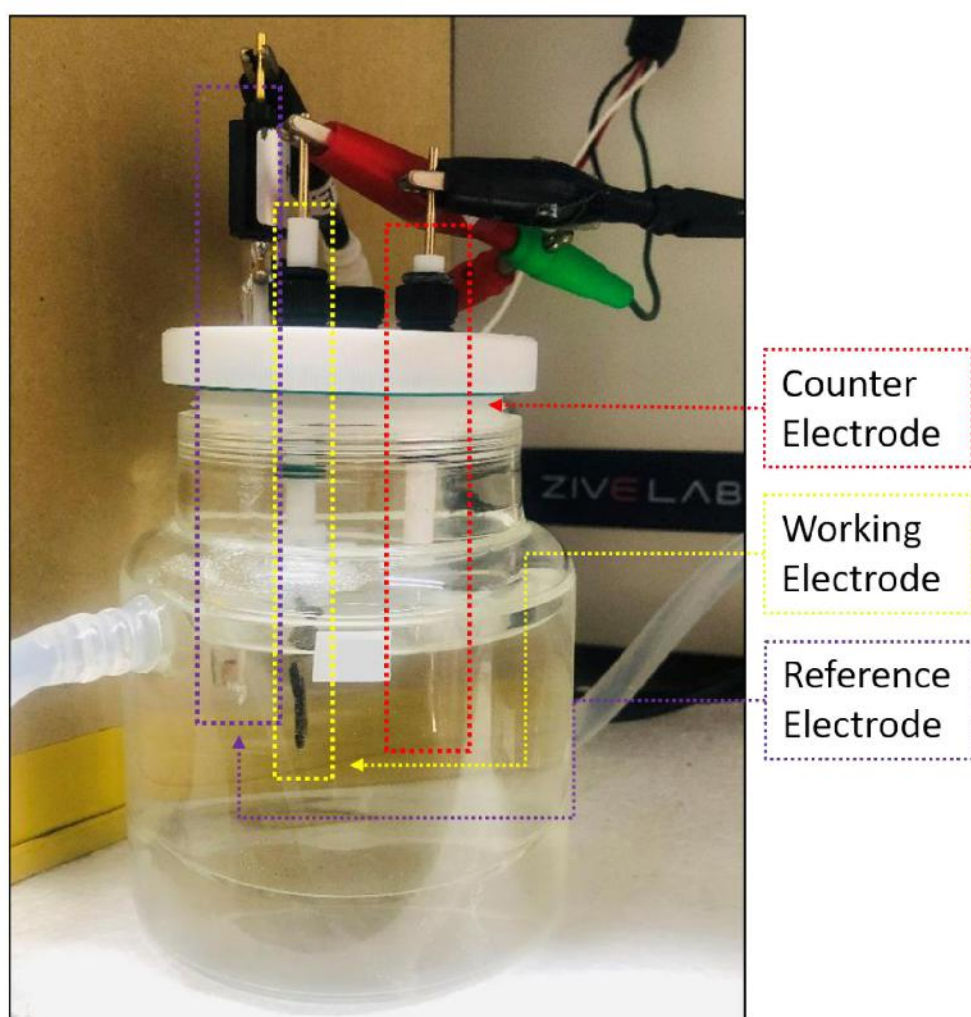


Figure 2.19: Photograph of three electrodes experimental set up for electrochemical techniques used for this study.

The electrochemical measurements are conducted using a potentiostat (Zive

Potentiostat/Galvanostat/EIS, Wonatech, Republic of Korea).

2.5.1. Cyclic voltammetry (CV)

Cyclic voltammetry (CV) is a potentiodynamic electrochemical measurement technique. In CV, the potential of the working electrode is ramped forward and backward through a predefined range with a constant sweep rate and the corresponding current is measured. Figure 2.20 shows a typical CV curve when the potential of the working electrode is ramped between V_1 and V_2 . As the potential increases, the current increases and the anodic peak is obtained. This anodic peak is called an oxidation peak. As the potential comes back the current decreases at a certain potential cathodic peak is obtained which is called a reduction peak.

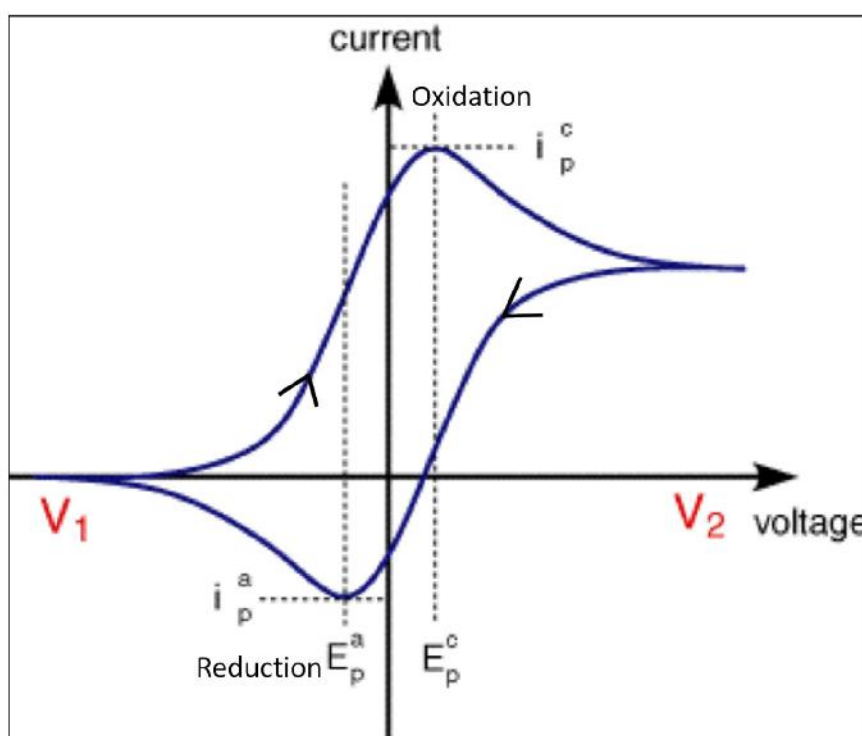


Figure 2.20: Cyclic voltammetry.

As the CV begins from V_1 the negative ions from the electrolyte get adsorbed on the surface of working electrode. As the potential of the working electrode increases slowly the concentration of positive charge also increases and resultantly

more and more negative ions get adsorbed. Hence, a double layer of charge is formed on the surface of the electrode. This is called charge storage by double layer or non-faradic mechanism. But when the potential of the working electrode further increases, at a potential value the current suddenly starts to increase and an anodic peak is obtained. This positive current is due to the oxidation of the electrode material. After reaching V_2 , the direction of ramping reversed from V_2 to V_1 . In this reverse scan, the oxidized material gets reduced and the cathodic peak is obtained. This oxidation and reduction of material in a higher potential region are combined called a redox reaction of a material and the charge storage through this process is called a redox or faradic mechanism [15]. The capacitance of material due to the non-faradic mechanism is called a double layer capacitance (C_{dl}) and the potential range in which it is measured is called a non-faradic potential region.

To better understand the origin of electrocatalytic performance, the electrochemically active surface area (ECSA) of thin film electrocatalysts prepared in the present study is estimated from the C_{dl} values. The CVs are recorded at different scanning rates in the non-faradic region of potential. The difference between anodic and cathodic current density at a fixed potential is plotted as a function of scan rate. The slope of linear fitting to the measured values represents the double-layer capacitance (C_{dl}). The ' C_{dl} ' can be further converted into ECSA using the specific capacitance value of a standard 1 cm^2 flat surface, which is normally between 0.02 - 0.06 mF cm^{-2} for an alkaline medium [16]. Therefore, an average value of 0.04 mF cm^{-2} is used for the estimation [17]. Therefore, the ECSA for an electrode is estimated through C_{dl} value using the relation,

$$ECSA = \frac{C_{dl}}{0.04 (\text{mF cm}^{-2})} \quad (2.3)$$

2.5.2. Linear sweep voltammetry (LSV)

Linear sweep voltammetry is a voltammetry method where current at the working electrode is measured while the potential between the working electrode and a reference electrode is swept linearly in time. The only difference between CV and LSV is that, in CV the potential is ramped between V_1 and V_2 in a cyclic manner ($V_1 \rightarrow V_2 \rightarrow V_1$) while in LSV potential is ramped from V_1 to V_2 in a linear way ($V_1 \rightarrow V_2$) as shown in Figure 2.21 (a). Hence LSV is nothing but the forward scan of CV (Figure 2.21 (b)).

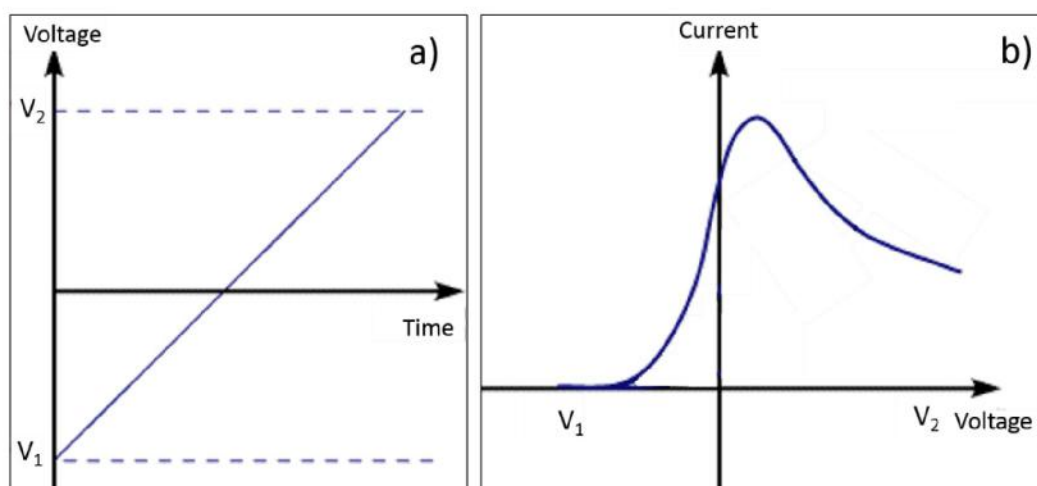


Figure 2.21: a) Potential sweep between V_1 and V_2 with time in LSV and b) corresponding current response as a function of voltage.

As discussed in CV, the peak occurs due to the oxidation of the material. After the peak potential, the oxidized species get saturated hence no material can oxidize on further increasing potential. Now if we further increased the potential of the working electrode the water oxidation reaction starts to occur at active sites. As we discussed in chapter 1, four electrons are removed in the evolution of one oxygen molecule (O_2). Hence current starts to increase.

The scan rate during LSV measurement makes a great impact on the current

response. The current increases with increasing scan rate. Hence while examining and comparing the LSV of more than two electrodes the scan rate must be similar. In the present study, all LSVs are measured with a scan rate of 2 mV s^{-1} . All the potentials measured (in SCE scale) in the present study converted to a reversible hydrogen electrode (RHE) scale by the Nernst equation:

$$E_{RHE} = E_{SCE} + 0.059 \times \text{pH} + E_{SCE}^0 \quad (2.4)$$

where ' E_{RHE} ' is the converted potential vs. RHE, ' E_{SCE} ' is experimentally measured potential versus reference electrode (SCE), and ' E_{SCE}^0 ' is the standard redox potential of SCE at 298 K ($0.244 \text{ V} \pm 0.002 \text{ V}$).

From the polarization curve, overpotential, η at current density, j (mA cm^{-2}) was estimated through the relation,

$$\eta_{@j} = E_{RHE} - 1.23 \text{ V} \quad (2.5)$$

2.5.3. Tafel slope

The current in electrochemistry is related exponentially to the overpotential as shown in equation 2.6.

$$i = a' e^{\eta/b'} \quad (2.6)$$

where i is current, η is overpotential and a' and b' are constants.

By taking logarithmic scale, the above equation can be written as,

$$\eta = a + b \log(i) \quad (2.7)$$

where a and b are constants.

The above equation (2.7) is nothing but the Tafel equation. Tafel equation relates the rate of an electrochemical reaction to the overpotential. The low value of Tafel slope

suggests the high rate of reaction or fast reaction kinetics while a high value of Tafel slope suggests the low rate of reaction or slow reaction kinetics. To determine the Tafel slope first the Tafel plots are plotted from LSV curves for each electrode and then the linear component of the Tafel plot fitted with the above Tafel equation.

2.5.4. Electrochemical impedance spectroscopy (EIS)

The oxygen evolution reaction (OER) is considered to occur with numerous elementary multi-step reactions such as adsorption, dissociation, charge-transfer and desorption. Each of these elementary reactions is expected to contribute some particular resistance to the overall operation, also called polarization. To perform an insightful analysis of the oxygen evolution reaction at the thin film electrocatalysts in the present study, electrochemical impedance spectroscopy (EIS) was employed. Impedance is nothing but the AC resistance of the cell, which consists of imaginary and real parts. The electrochemical cell contains resistive, capacitive and inductive properties. Resistive properties involve in the real part, while capacitive and inductive properties involve in the imaginary part. Figure 2.22 represents a typical Nyquist plot obtained from EIS. Where Z' and Z'' represent the real and imaginary parts of EIS, respectively.

The intercept of Nyquist plot to the X-axis (i.e. real part) in the lower frequency region represents the solution resistance (R_s). While the intercept in the higher frequency region represents the sum of a solution resistance (R_s) and charge transfer resistance (R_{ct}). Hence the diameter of the semicircle is nothing but R_{ct} . EIS in present study is measured with a nominal root-mean-square amplitude potential (V_{rms}) of 10 mV, in the frequency range of 0.1 MHz to 10 mHz.

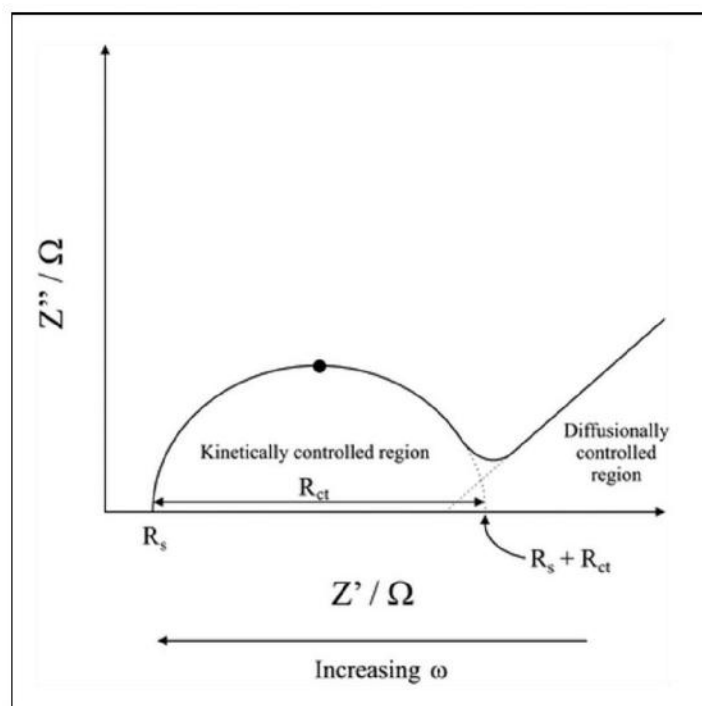


Figure 2.22: A typical Nyquist plot obtained from electrochemical impedance spectroscopy.

2.6 References

- [1] L. Yu, H. Zhou, J. Sun, F. Qin, F. Yu, J. Bao, Y. Yu, S. Chen, Z. Ren, Cu nanowires shelled with NiFe layered double hydroxide nanosheets as bifunctional electrocatalysts for overall water splitting, *Energy Environ. Sci.* 10 (2017) 1820–1827. <https://doi.org/10.1039/c7ee01571b>.
- [2] I. Gurrappa, L. Binder, Electrodeposition of nanostructured coatings and their characterization-A review, *Sci. Technol. Adv. Mater.* 9 (2008) 43001 (1-11). <https://doi.org/10.1088/1468-6996/9/4/043001>.
- [3] M. Ristov, G. Sinadinovski, I. Grozdanov, Chemical deposition of Cu_2O thin films, *Thin Solid Films.* 123 (1985) 63–67. [https://doi.org/10.1016/0040-6090\(85\)90041-0](https://doi.org/10.1016/0040-6090(85)90041-0).
- [4] Y. F. Nicolau, Solution deposition of thin solid compound films by a successive ionic-layer adsorption and reaction process, *Appl. Surf. Sci.* 22 (1985) 1061–1074. [https://doi.org/10.1016/0378-5963\(85\)90241-7](https://doi.org/10.1016/0378-5963(85)90241-7).
- [6] Allen J. Bard, Larry R. Faulkner, *Electrochemical Methods: Fundamentals and Applications*, 2nd Edition, John Wiley & Sons, inc. Chapter 1: Introduction and overview of electrode processes, (2000).
- [6] H. M. Pathan, C. D. Lokhande, Deposition of metal chalcogenide thin films by

- successive ionic layer adsorption and reaction (SILAR) method, *Bull. Mater. Sci.* 27 (2004) 85–111. <https://doi.org/10.1007/BF02708491>.
- [7] S. Saha, M. Johnson, F. Altayaran, Y. Wang, D. Wang, Q. Zhang, Electrodeposition fabrication of chalcogenide thin films for photovoltaic applications, *Electrochem*, 1 (2020) 286–321. <https://doi.org/10.3390/electrochem1030019>.
- [8] https://en.wikipedia.org/wiki/Stranski%E2%80%93Krastanov_growth
- [9] https://en.wikipedia.org/wiki/Frank%E2%80%93van_der_Merwe_growth
- [10] https://en.wikipedia.org/wiki/Stranski%E2%80%93Krastanov_growth
- [11] V. R. Shinde, T. P. Gujar, C. D. Lokhande, R. S. Mane, S. H. Han, Development of morphological dependent chemically deposited nanocrystalline ZnO films for liquefied petroleum gas (LPG) sensor, *Sens. Act. B*, 123 (2007) 882–887. <https://doi.org/10.1016/j.snb.2006.10.044>
- [12] S. Sharma, D. Verma, L. Khan, S. Kumar, S. Khan, Chapter 13: Introduction to X-Ray Absorption Spectroscopy and Its Applications in Material Science, *Handbook of Materials Characterization*, Springer International Publishing, (2018) 497–548.
- [13] G. McMahon, *Analytical instrumentation: a guide to laboratory, portable and miniaturized instruments*, John Wiley & Sons, (2008).
- [14] J. I. Goldstein, D. E. Newbury, J.R. Michael, N. W. M. Ritchie, J. II. J. Scott, D. C. Joy, *Scanning electron microscopy and X-ray microanalysis*, Springer, (2017).
- [15] C. G. Zoski, *Handbook of electrochemistry*, Elsevier Science, (2006). http://www.123library.org/book_details/?id=36518.
- [16] C. C. L. McCrory, S. Jung, J. C. Peters, T. F. Jaramillo, Benchmarking heterogeneous electrocatalysts for the oxygen evolution reaction, *J. Am. Chem. Soc.* 135 (2013) 16977–16987. <https://doi.org/10.1021/ja407115p>.
- [17] C. Ray, S. C. Lee, K. V. Sankar, B. Jin, J. Lee, J. H. Park, S. C. Jun, Amorphous phosphorus-incorporated cobalt molybdenum sulfide on carbon cloth: An efficient and stable electrocatalyst for enhanced overall water splitting over entire pH values, *ACS Appl. Mater. Interfaces*. 9 (2017) 37739–37749. <https://doi.org/10.1021/acsami.7b11192>.

CHAPTER 3

Synthesis, characterization and electrocatalytic OER performance of cobalt sulfide thin film electrode

**Chapter 3: Synthesis, characterization and electrocatalytic OER
 performance of cobalt sulfide thin film electrode**

3.1.	Introduction.....	67
3.2.	Experimental details.....	69
3.2.1.	<i>Substrate and Substrate cleaning</i>	69
3.2.2.	<i>Chemicals</i>	69
3.2.3.	<i>Synthesis of cobalt sulfide thin films</i>	70
3.3.	Results and discussion.....	73
3.3A.	Physicochemical Characterizations.....	73
3.3A.1.	<i>XRD</i>	73
3.3A.2.	<i>FESEM</i>	74
3.3A.3.	<i>HR-TEM</i>	76
3.3B.	Electrochemical characterizations.....	77
3.3B.1.	<i>LSV and Tafel slope</i>	77
3.3B.2.	<i>ECSA</i>	79
3.3B.3.	<i>EIS and Stability</i>	82
3.4.	Conclusions.....	85
3.5	References.....	85

3.1. Introduction

Electrolysis of water is the simplest of all the water-splitting techniques and it offers a promising approach for scalable production of high purity hydrogen [1,2]. However, the OER at anode has a thermodynamic barrier and to overcome it, the development of a cost-effective electrocatalyst from earth abundant transition metal elements is needed [3,4]. In this field of electrochemical water splitting, cobalt sulfide has acquired significant attention in recent years due to its excellent electrochemical activity among different transition metal chalcogenides [5]. Different phases of cobalt sulfide (CoS , Co_9S_8 , Co_3S_4 , Co_{1-x}S) have been investigated for application in electrocatalytic OER [6-9]. Among them, Co_9S_8 showed good OER performance (in terms of overpotential). Most of the electrode materials for electrocatalysis are prepared in the form of powder and polymer binders are used to adhere this powder to conducting substrate. The use of a binder during the electrode fabrication process increases contact resistance [10]. Therefore, to prepare an efficient electrocatalyst, direct deposition of the catalyst material on a conducting substrate is desired. The successive ionic layer adsorption and reaction (SILAR) is a simple and convenient chemical method for thin film deposition of metal chalcogenides on any substrate.

The OER is a surface phenomenon that takes place at electrochemically active sites present at the surface of catalyst material [11]. Due to this, the morphology of electrocatalyst plays an important role in its activity as it directly reflects the topological characteristic of material exposed to the electrolyte. It is observed that OER activity is significantly increased by tailoring the active sites in a particular morphology. Therefore, in addition to various performance limiting parameters, researchers are putting special efforts to tune the morphology of catalyst materials to obtain maximum surface area and reaction sites for the electrochemical

reactions [12-16]. Particularly for cobalt oxide, Xu et. al. [17] synthesized Co_3O_4 by three different methods (solution method, hydrothermal process and sol-gel auto combustion) to obtain three different morphologies and examined their electrochemical OER performance to establish the relationship between the catalytic activity and morphology. Kong et. al. [13] also synthesized different morphologies of Co_3O_4 using various solvents and investigated their effect on electrochemical catalytic properties.

In any electrochemical reaction, the mass loading of active material drastically influences its performance [18,19]. Therefore, it is very important to control the mass loading of active material on the conducting backbone to obtain optimum performance. In the SILAR method, the mass loading of active material can be easily controlled by varying deposition cycles. Also, from previous reports, the microstructure of thin films considerably changed with mass loadings [20-22]. To avoid drawbacks of the binder during casting of catalyst powder on conducting substrate, researchers have recently started to grow self-supported and binder free architectures on 3D porous nickel foam. However, under the extremely alkaline condition (1 M KOH) of water electrolysis, the nickel foam is highly unstable. The formation of nickel hydroxide and/or oxyhydroxide species takes place during the electrochemical study [23]. These issues can be overcome by using non-oxidizing stainless steel as a conducting backbone for binder free architectures. Therefore, in the present study, cobalt sulfide thin films are deposited by SILAR method on stainless steel substrates at different deposition cycles. Physicochemical properties of cobalt sulfide thin film electrodes are characterized using different characterization techniques such as XRD, FESEM, and HR-TEM. Electrochemical OER performance is tested in 1 M KOH electrolyte.

3.2. Experimental details

3.2.1 Substrate cleaning

The heterogeneous growth of material in chemical deposition methods initiates from nucleation sites provided by substrate. A substrate with an impurity is responsible for the uncontrolled growth of material and results in the deposition of a non-uniform thin film. Therefore, substrate cleaning is critical for uniform film deposition.

The step wise procedure used for the SS substrate cleaning is as follow,

Step 1: The SS substrate is wiped with acetone to remove the dirt.

Step 2: The SS substrate is mirror polished using zero grade polish paper.

Step 3: After polishing, the substrate is cleaned with detergent and double distilled water (DDW).

Step 4: Finally, the substrate is ultrasonically cleaned in DDW for 15 minutes and dried at room temperature.

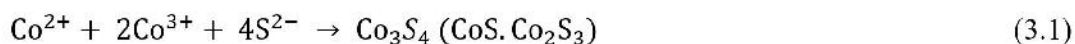
3.2.2. Chemicals

Analytical grade cobalt chloride ($\text{CoCl}_2 \cdot 6\text{H}_2\text{O}$), sodium sulfide ($\text{Na}_2\text{S} \cdot \text{H}_2\text{O}$) and potassium hydroxide (KOH) were purchased from S. D. Fine Chem. Ltd. and used without further purification. Stainless steel (SS) substrates of thickness 0.5 mm (purchased from a local supplier) were used for film deposition. Potassium hydroxide (KOH, Sigma Aldrich, USA) was used to prepare an aqueous electrolyte. The double distilled water (DDW) was used throughout the experiment.

3.2.3 Synthesis of cobalt sulfide thin films

The deposition of cobalt sulfide thin film electrodes was carried out using SILAR method. 40 ml, 0.1 M solutions of CoCl_2 and Na_2S prepared in DDW were used as cationic and anionic precursor solutions, respectively. The deposition was carried out at room temperature (300 K). Four steps were involved in one complete SILAR cycle; 1) adsorption of cations (Co^{2+}); 2) first rinsing in DDW; 3) adsorption of anions (S^{2-}) and their reaction with pre-adsorbed cations (Co^{2+}) and 4) second rinsing in DDW. In SILAR method, the time duration for adsorption, reaction and rinsing are important parameters. In the present study, the optimized time for adsorption of Co^{2+} , adsorption of anions (S^{2-}) and their reaction with pre-adsorbed cations (Co^{2+}) and rinsing in third and fourth beakers are 20, 20 and 50 s, respectively.

In detail, A clean SS substrate is immersed vertically into the first beaker containing cationic (Co^{2+}) solution for 20 s. During this step, the solvated cations (Co^{2+}) are adsorbed on the surface of SS substrate due to the cohesive forces or Van der Waals forces or chemical attractive forces [24]. Some of the Co^{2+} ions in this step are loosely bonded. To avoid homogeneous precipitation in the third step due to these loosely bonded ions, rinsing is introduced in the second step (for 50 s). In this step, loosely bonded and excess adsorbed Co^{2+} ions are washed away. The SS substrate is then immersed into anionic (S^{2-}) solution for 20 s as a third step. This step involves the reaction between pre-adsorbed Co^{2+} ions and newly adsorbed S^{2-} ions and finally, a solid film of cobalt sulfide is formed on the substrate. As the solution of Na_2S ($\text{pH} = 11 \pm 0.1$) is used in third step, the oxidation state of some pre-adsorbed cobalt ions changes from +2 to +3 (i.e. $\text{Co}^{2+} \rightarrow \text{Co}^{3+}$). Due to this, mixed-valence cobalt sulfide is formed. The reaction mechanism of cobalt sulfide formation is as follows,



In the fourth step, excess and unreacted species and reaction byproducts are removed by rinsing into DDW (for 50 s). Such deposition cycles are repeated 20, 40, 60 and 80 times and corresponding samples are designated as CS-20, CS-40, CS-60 and CS-80, respectively. The gravimetric weight difference method is used to determine the amount of cobalt sulfide deposited per unit area, with different deposition cycles. For this, the weight of substrate before and after deposition is measured and then the difference in the weights is divided by the total deposited area. In the case of thin film, the mass loading of material on a substrate is very small. Therefore, analytical balance from Contech Instruments Ltd. with an accuracy of 0.00001 gm is used. The weight deposited of cobalt sulfide at different deposition cycles is represented in Figure 3.1. The 0.07, 0.27, 1.09 and 3.71 mg cm⁻² material is deposited for CS-20, CS-40, CS-60 and CS-80 electrodes, respectively.

The photograph of cobalt sulfide thin film electrodes prepared at different deposition cycles is shown in Figure 3.2. The change in colour of the films from light black to dark black is credited to increased film thickness. Importantly, thin film prepared with more than 80 SILAR deposition cycles gets peeled off. This is maybe due to the formation of outer layer which develops stress to cause delamination of film after drying. This delamination of film results in its nonuniformity.

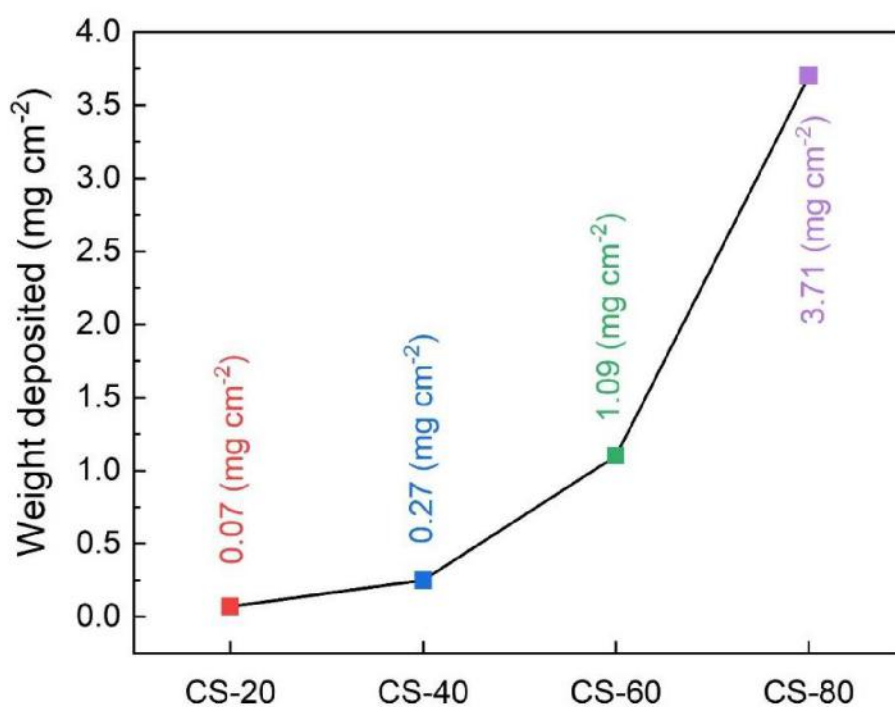


Figure 3.1: Graphical representation of weight deposited of cobalt sulfide on SS substrate at 20 (CS-20), 40 (CS-40), 60 (CS-60) and 80 (CS-80) SILAR deposition cycles.

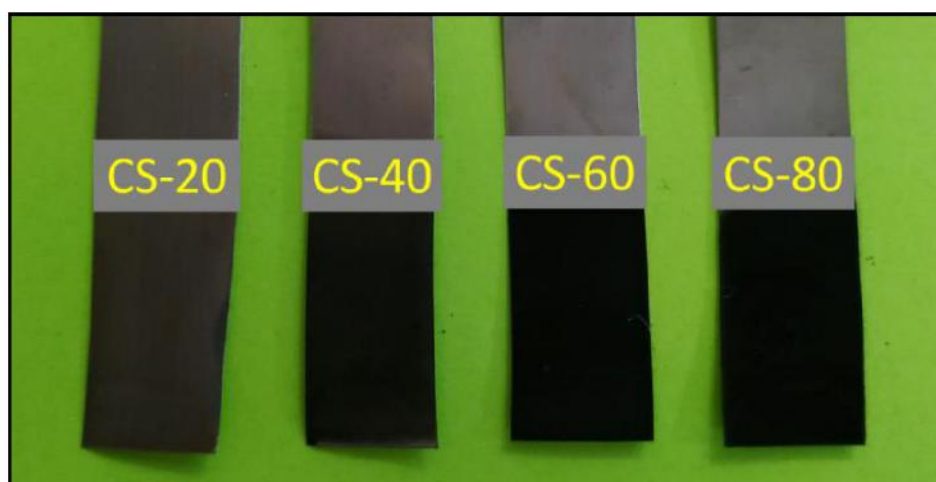


Figure 3.2: Photograph of cobalt sulfide thin film electrodes prepared at different SILAR deposition cycles.

3.3. Results and discussion

3.3A. Physicochemical characterizations

3.3A.1. X-ray diffraction

The X-ray diffraction patterns of bare SS substrate and cobalt sulfide thin films deposited on SS substrates at different SILAR deposition cycles are shown in Figure 3.3.

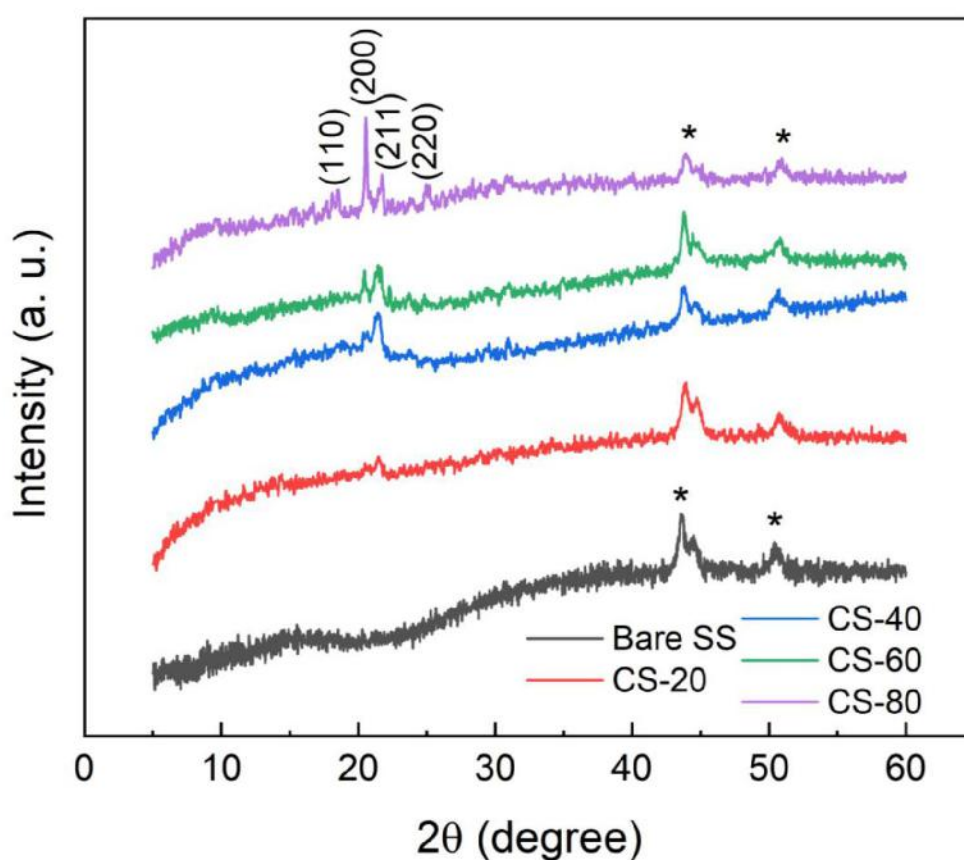


Figure 3.3: The XRD patterns of bare SS substrate and cobalt sulfide thin film electrodes prepared at different deposition cycles.

All the samples have a similar pattern of XRD. The diffraction peaks at 18.35° , 20.54° , 21.7° and 24.9° are well matched to the (110), (200), (211) and (220) diffraction planes of face centered cubic Co_3S_4 , respectively (JCPDS No. 75-0605). The peaks

denoted by ‘*’ correspond to SS substrate. The thickness of Co_3S_4 thin films increases with an increase in the number of deposition cycles. Therefore, with an increase in deposition cycles, the intensity of the diffraction peaks of SS substrate gradually decreases while the intensity of diffraction peaks from Co_3S_4 increases. The presence of sharp and intense diffraction peaks in XRD pattern of CS-80 indicates its high crystallinity. Also, the absence of any other additional peaks demonstrates the high purity of Co_3S_4 .

3.3A.2. Field emission scanning electron microscopy

The change in microstructure of Co_3S_4 thin film electrodes due to the variation in number of deposition cycles is visualized by FE-SEM images. Figure 3.4 shows FE-SEM images of Co_3S_4 thin film electrodes at two different magnifications of 300X and 600X. Figures 3.4 (a), 3.4 (c), 3.4 (e) and 3.4 (g) clearly show that thin film is uniformly deposited on SS substrate with some agglomerated particles on the surface. Also, the agglomeration of Co_3S_4 particles increases from sample CS-20 to CS-80. In the case of sample CS-80, bigger sized particles are seen. The texture of samples CS-20 and CS-40 in Figures 3.4 (b) and 3.4 (d) appear to be smooth, while sample CS-60 (Figure 3.4 (f)) is slightly rough.

The roughness of the surface is significantly increased in sample CS-80, as observed in Figure 3.4 (h). This change in the surface morphology in the samples is attributed to the growth of particles on the surface of the film. Along with the roughness, the surface porosity is also observed at higher magnification of 50kX (Figure 3.4 (i)), which is highly important for the ion exchange process during the electrochemical study.

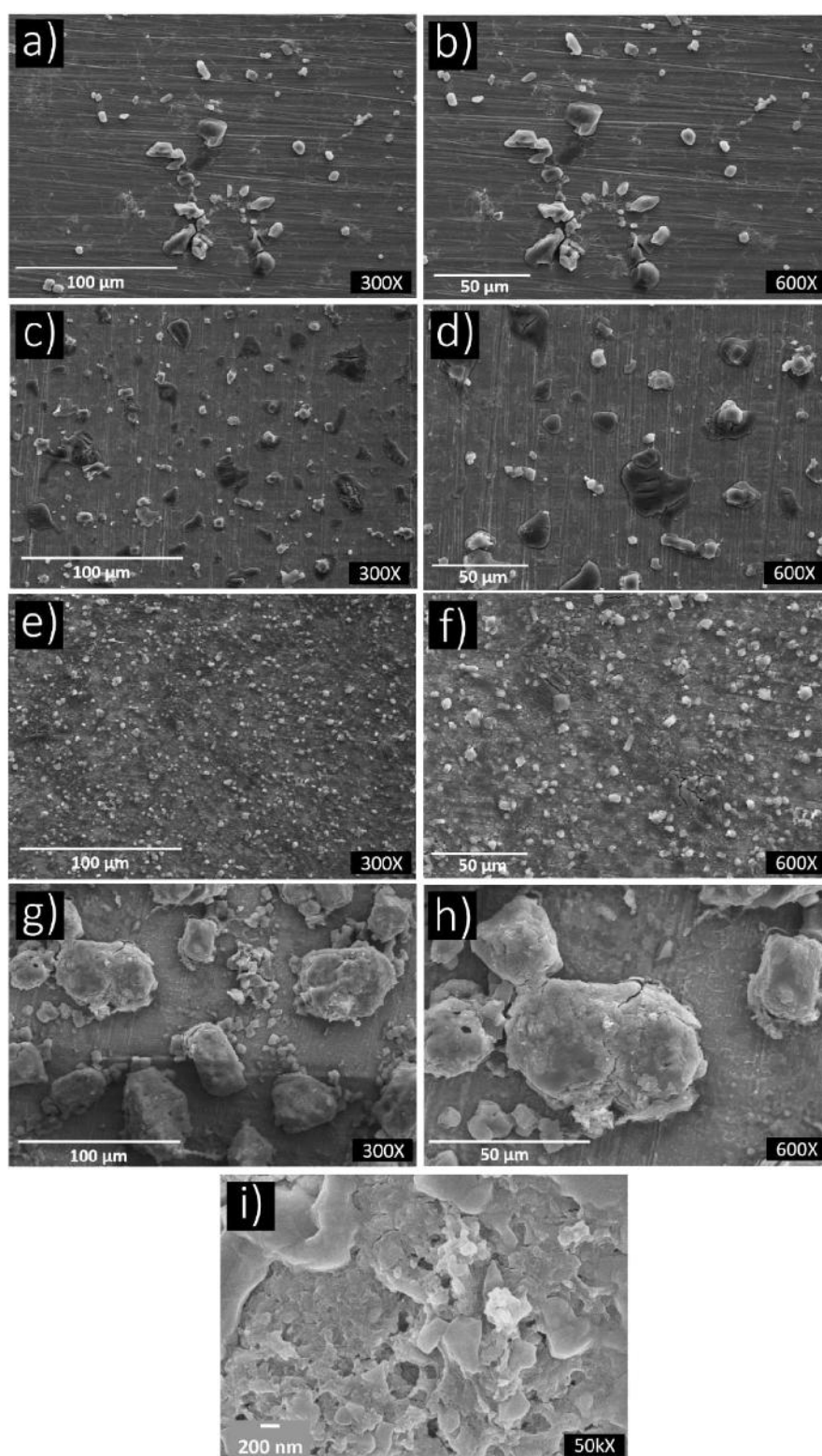


Figure 3.4: The FESEM images of Co_3S_4 thin film electrodes deposited at different SILAR cycles, (a, b) CS-20, (c, d) CS-40, (e, f) CS-60 and (g, h) CS-80 at 300X and 600X magnifications. (i) FESEM image of CS-80 at 50kX magnification.

Previously, Momeni and Mozafari [25] have studied the effect of number of SILAR cycles on the morphology of cadmium sulfide deposited on titania nanotubes and observed that by increasing the cycle number of SILAR, more amount of cadmium sulfide is deposited due to which morphology changes.

3.3A.3. High-resolution transmission electron microscopy

Figure 3.5 (a) shows the TEM image of CS-80 powder, smoothly scratched from SS substrate using a surgical blade. The figure confirms the agglomeration of material as like in FE-SEM image of CS-80. High Angle Annular Dark Field (HAADF) Scanning Transmission Electron Microscopy (STEM) is a very powerful technique to provide direct information on the local chemistry of nano-materials at atomic scale.

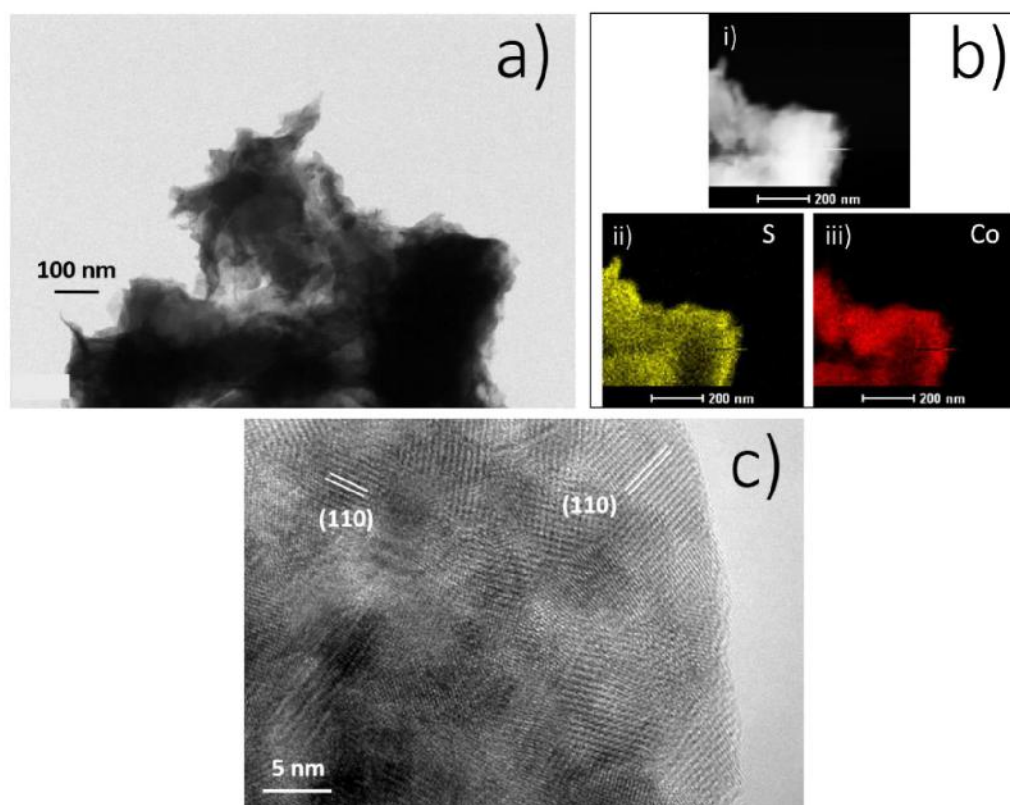


Figure 3.5: a) TEM image, b) (i) HAADF-STEM and (ii, iii) EDX elemental mapping and c) HR-TEM image of CS-80.

Figure 3.5 (b) (i) show HAADF-STEM image of a small area of CS-80. Energy-dispersive X-ray spectroscopy (EDX) elemental mappings of S and Co over the same area are shown in Figure 3.5 (b) (ii) and (iii), respectively. It is seen that Co and S are homogeneously distributed in the nanoparticle structure. Figure 3.5 (c) shows HR-TEM image of CS-80. The bright stripes are called lattice fringes, they can appear in one or more directions. As the TEM specimen/sample is very thin, these fringes can be interpreted as the projection of tunnels between columns of atoms, while the dark lines are the atoms themselves. From Figure, lattice fringe spacing of 0.351 nm is found which corresponds to the (110) plane of crystalline Co_3S_4 , consistent with XRD results discussed above.

3.3B. Electrochemical characterizations

3.3B.1. Linear sweep voltammetry and Tafel slope

The OER activity of Co_3S_4 thin film electrode is evaluated by performing linear sweep voltammetry (LSV) in 1 M KOH solution. The potential of working electrodes was swept linearly from 1.35 to 1.6 V vs RHE with a 2 mV s^{-1} scan rate. The LSV of bare SS substrate was also measured at similar conditions, to compare the performance of Co_3S_4 thin film electrodes. The obtained LSV curves are shown in Figure 3.6 (a). The catalytic activity is measured in terms of overpotential, calculated using equation (2.5) (given in the previous chapter), required to achieve a current density of 10 mA cm^{-2} . The overpotential required for bare SS substrate to reach 10 mA cm^{-2} current density is 400 mV. The absence of any active material, hence catalytically active sites, bare SS substrate requires such high overpotential to reach benchmarking current density. The value of overpotential decreased by 70 mV and become 330 mV (at the same current density) after 20 SILAR deposition cycles (CS-

20). The value of overpotential further decreases with an increase in deposition cycles. Co_3S_4 deposited with 40 and 60 SILAR cycles i.e., CS-20 and CS-40 require 300 and 288 mV overpotential to reach 10 mA cm^{-2} current density, respectively. For the Co_3S_4 thin film electrode deposited with 80 deposition cycles, 275 mV overpotential is required to reach 10 mA cm^{-2} current density. When compared with bare SS substrate, there is a 31.25% decrement in overpotential due to the deposition of 3.71 mg cm^{-2} Co_3S_4 . Hence, the electrochemical OER activity increases with an increase in the number of SILAR cycles.

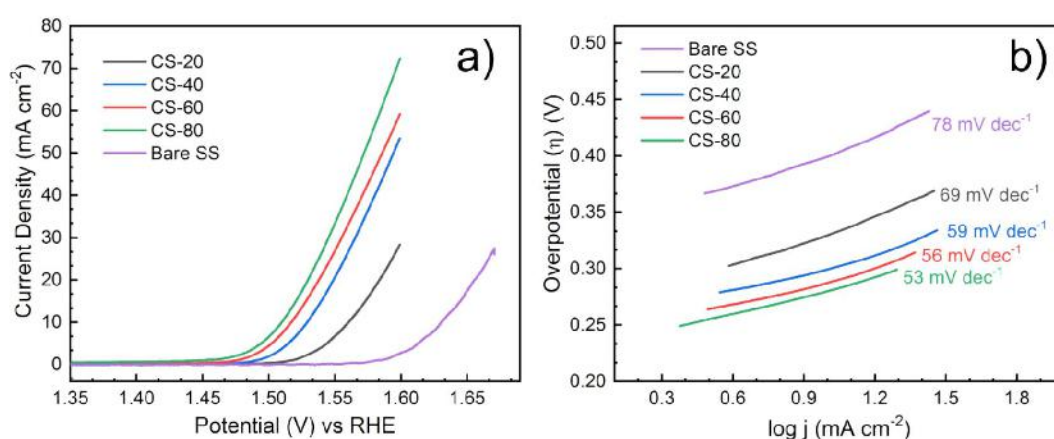


Figure 3.6: a) Linear sweep voltammetry (LSV) curves at a scan rate of 2 mV s^{-1} and b) Tafel plots extracted from LSV curves of Co_3S_4 thin film electrocatalysts prepared at different deposition cycles.

The high overpotential of bare SS substrate than the Co_3S_4 thin film electrode suggests poor catalytic activity of bare SS substrate. Therefore, it can be concluded that SS substrate does not contribute to the catalytic performance of thin film material. It is observed in the LSV curves, as the number of deposition cycles increases, the current density at higher potentials ($> 1.48 \text{ V vs RHE}$) also increases. The mass loading of Co_3S_4 has increased with increase in the number of SILAR cycles. Also, at a scan rate of 2 mV s^{-1} , the electrolyte gets sufficient time to interact with electrode

material, as well as the diffusion of electrolyte into electrode is maximum. Hence, the interaction of electrolyte and electrode material increases with the increase in the number of deposition cycles. Therefore, the current density increases with number of deposition cycles of Co_3S_4 . These results suggest the importance of optimization of mass loading of active material on substrate.

To extract the Tafel slope from LSV curve, the current density is first converted into a logarithmic scale. The log of current density is then plotted against overpotential (by subtracting 1.23 V from measured values). The resultant graph is called the Tafel plot. The Tafel plots for all Co_3S_4 thin film electrodes are shown in Figure 3.6 (b). The slope of these Tafel plots is nothing but the corresponding Tafel slope. The bare SS substrate possesses a Tafel slope of 78 mV dec^{-1} . While, CS-20, CS-40, CS-60 and CS-80 electrodes possess 69, 59, 56 and 53 mV dec^{-1} Tafel slopes, respectively. This indicates fast reaction kinetics with increasing deposition cycles. The large Tafel slope of bare SS substrate than Co_3S_4 thin film electrocatalysts may be due to the absence of any catalytically active material and hence catalytically active sites. Hence, Co_3S_4 thin film electrocatalysts deposited with 80 SILAR cycles i.e. CS-80 required low overpotential and have fast reaction kinetics than others. A rough and porous surface of CS-80 might have provided more catalytically active sites open to the electrolyte, due to which the total OER reactions increase than other electrodes.

3.3B.2. Electrochemical active surface area

The electrochemically active surface area (ECSA) of Co_3S_4 thin film electrocatalysts is estimated from the electrochemical double-layer capacitance (C_{dl}). To obtain C_{dl} , cyclic voltammetry (CV) at varied scan rates ($10\text{-}50 \text{ mV s}^{-1}$) is performed in a narrow potential window of ± 0.1 to $\pm 0.3 \text{ V vs SCE}$, where no faradic

reaction is observed. The obtained CV curves at different scan rates for all electrocatalysts are shown in Figure 3.7 (a-d). In this potential window (+0.1 to +0.3 V vs SCE), the current is generated only for charging of a double layer. From CV curves, the current density is measured @ 0.2 V vs. SCE and plotted as a function of scan rate, as shown in Figure 3.7 (e). The plots show linear nature and slope of it is nothing but the ' C_{dl} ' [26]. The ' C_{dl} ' can be further converted into ECSA using the specific capacitance value of a standard 1 cm² flat surface which is normally between 0.02-0.06 mF cm⁻² for alkaline medium [27]. Therefore, an average value of 0.04 mF cm⁻² is used in the calculation by equation (2.3) The values of ECSA obtained for samples CS-20, CS-40, CS-60 and CS-80 are 25, 175, 650 and 1750 cm², respectively. Hence, cobalt sulfide thin film electrocatalyst deposited with 80 SILAR cycles i.e. CS-80 possess higher ECSA. The higher ECSA value of sample CS-80 compared to other electrodes can be attributed to the surface roughness. The rough and porous morphology of CS-80 probably has more open sites than the smooth texture which acts as catalytic active sites.

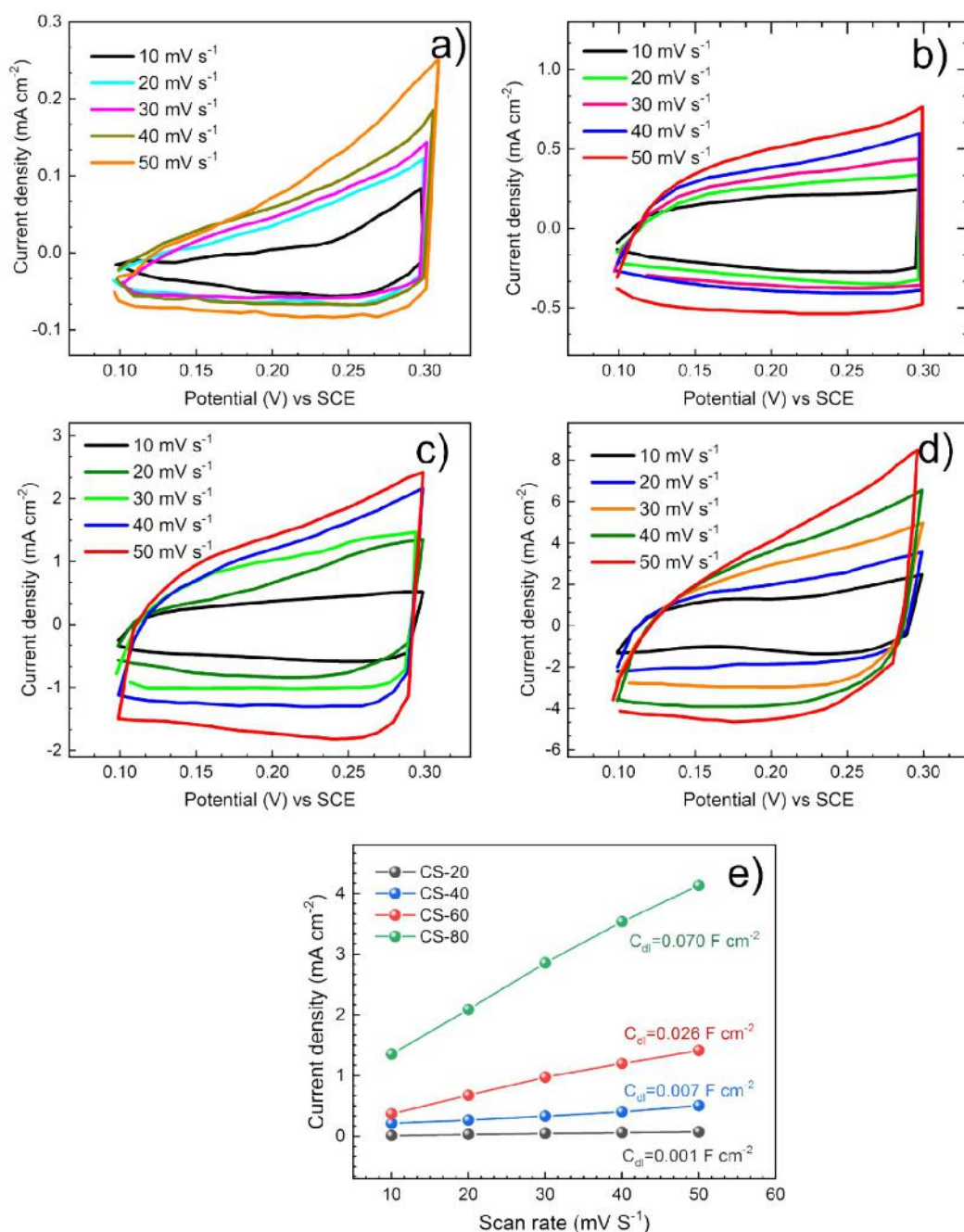


Figure 3.7: The cyclic voltammetry curves in a potential window of +0.1 to +0.3 V vs SCE for a) CS-20, b) CS-40, c) CS-60 and d) CS-80. e) Current density (at +0.2 V vs. SCE) vs. scan rate plots obtained from CV curves for all electrocatalysts.

3.3A.3. Electrochemical impedance spectroscopy and Stability

The electron and charge transferability during the electrochemical process is studied using the electrochemical impedance spectroscopy (EIS) technique. Nyquist plots for Co_3S_4 thin film electrocatalysts are shown in Figure 3.8. The inset (i) of Figure 3.8 shows equivalent circuit model (ECM) fitted to Nyquist plot. The inset (ii) of Figure 3.8 shows a magnified view of the higher frequency region of Nyquist plots. From magnified view, CS-80 possesses small semicircle among all electrocatalysts. The value of charge transfer resistance for CS-80 ($R_{ct}=1.52 \, \Omega \, \text{cm}^{-2}$) is significantly small than CS-60 ($3.17 \, \Omega \, \text{cm}^{-2}$). The low values of resistance may be due to more interaction between active material and electrolyte. The binder-free approach of Co_3S_4 synthesis using SILAR method in this study and slightly porous structure are the reasons for low resistance values.

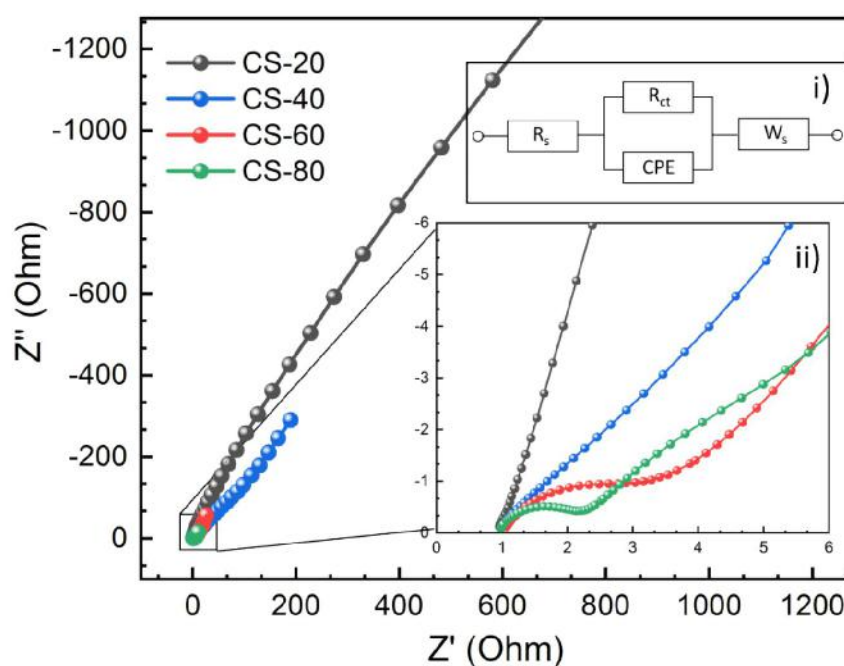


Figure 3.8: Nyquist plots (obtained from EIS) of Co_3S_4 thin film electrocatalysts prepared at different deposition cycles. The inset i) shows equivalent circuit model (ECM) and ii) shows magnified view of Nyquist plot in higher frequency region.

The stability of electrocatalyst is also an important criterion to assess the performance of the catalyst in practical applications. Herein, the electrochemical stability of CS-80 electrocatalyst towards OER is measured by chronopotentiometry mode at a constant current density of 10 mA cm^{-2} for 13 h (Figure 3.9 (a)). The CS-80 electrocatalyst displays a negligible change in the polarization curve after 13 h of continuous oxygen evolution, as shown in Figure 3.9 (b), indicating good stability towards the OER. Figure 3.9 (c) shows Tafel slope of CS-80 electrocatalyst, extracted from LSV graphs, before and after stability. The value of Tafel slope increased from 53 to 55 mV dec^{-1} . This may be due to the blocking of some catalytically active sites during the long term OER.

Electrochemical parameters obtained in this study for Co_3S_4 thin film electrocatalysts prepared at different SILAR deposition cycles are summarized in table 3.1. From the table, small Tafel slope, high ECSA and lower charge transfer resistance (R_{ct}) of CS-80 indicate faster OER kinetics with an effective electron transfer mechanism for efficient catalytic activity [25]. Hence, Co_3S_4 thin film electrocatalyst deposited at 80 SILAR cycles is efficient and promising for OER. Zhu et. al. [8] prepared hydrophilic Co_3S_4 electrocatalyst powder using hydrophilic medium and precursors. The glassy carbon electrode (GCE) was coated with this powder using Nafion solution as a binder. The hydrophilic Co_3S_4 required 360 mV overpotential to reach 10 mA cm^{-2} current density and possess an 84.7 mV/decade Tafel slope. The higher values of overpotential and Tafel slope for hydrophilic Co_3S_4 reported by Zhu et. al. [8] than the Co_3S_4 thin film electrode prepared by SILAR method, in the present study, is due to the use of a binder. Drawbacks of the binder are avoided in present study via direct deposition of material in the form of thin film. As given in the introduction part of this chapter, Co_9S_8 phase of cobalt sulfide shows

good electrocatalytic performance than other phases. The Co_9S_8 electrocatalyst prepared by Lin et. al. [28], Liu et. al. [29] and Feng et. al. [30] requires 275, 278 and 285 mV overpotential, respectively to reach 10 mA cm^{-2} current density, while Co_3S_4 thin film electrode prepared in the present study require 275 mV overpotential. This is due to the use of binder in above mentioned reports of Co_9S_8 and binder free synthesis of Co_3S_4 in the present study. Hence, when compared with previously reported cobalt sulfide OER electrocatalysts, the Co_3S_4 thin film electrode prepared by SILAR method in the present study shows good electrocatalytic performance. The binder free synthesis in the form of thin film could be the main reason for this.

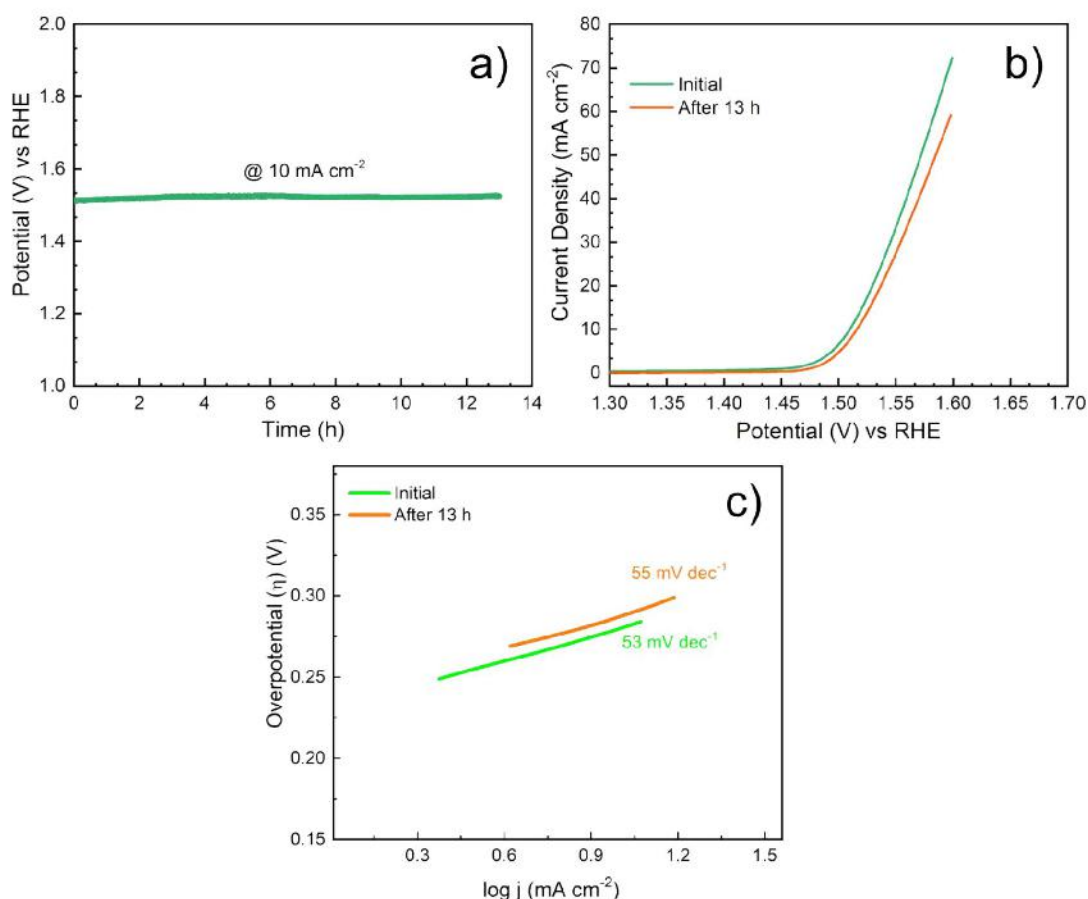


Figure 3.9: a) 13 h stability test of CS-80 thin film electrocatalyst at 10 mA cm^{-2} , b) The LSV curves measured before and after stability study and c) Tafel plots extracted from LSV curves of CS-80 thin film electrocatalysts before and after stability study.

Table 3.1: Electrochemical parameters obtained for Co₃S₄ thin film electrocatalysts prepared at different SILAR deposition cycles.

Electrode	Mass loading (mg cm ⁻²)	η @ 10 mA cm ⁻² (mV)	Tafel slope (mV dec ⁻¹)	ECSA (cm ²)	R_s (Ω cm ⁻²)	R_{ct} (Ω cm ⁻²)
SS	-	400	78	-		-
CS-20	0.07	330	69	25	0.81	2.2k
CS-40	0.27	300	59	175	0.84	310
CS-60	1.09	288	56	650	0.89	3.17
CS-80	3.71	275	53	1750	0.85	1.52

3.4. Conclusions

In summary, single metal sulfide i.e., cobalt sulfide thin film electrodes are deposited on SS substrates using a simple SILAR method. The mass loading of Co₃S₄ in thin film electrodes is significantly changed with the number of deposition cycles and which influenced the surface morphology. As an impact of change in morphology and mass loading, CS-80 (deposited at 80 SILAR cycles) thin film electrode exhibited an efficient electrocatalytic OER performance with 275 mV overpotential at 10 mA cm⁻² and Tafel slope 53 mV dec⁻¹. The rough and porous surface and binder free synthesis are the main reasons for high ECSA (1750 F cm⁻²) and low R_{ct} values (1.52 Ω) which enhance OER performance of CS-80 thin film electrode. Also, this study gives the importance of optimization of mass loading of catalyst material on the substrate.

3.5 References

- [1] M. Chauhan, K. P. Reddy, C. S. Gopinath, S. Deka, Copper cobalt sulfide nanosheets realizing a promising electrocatalytic oxygen evolution reaction, ACS Catal. 7 (2017) 5871–5879. <https://doi.org/10.1021/acscatal.7b01831>.

- [2] S. Hiao, Y. Yang, Water splitting in near-neutral media: using an Mn–Co-based nanowire array as a complementary electrocatalyst, *J. Mater. Chem. A* 5 (2017) 12091–12095. <https://doi.org/10.1039/C7TA03198J>.
- [3] Y. Lee, J. Suntivich, K. J. May, E. E. Perry, Y. Shao-Horn, Synthesis and activities of rutile IrO₂ and RuO₂ nanoparticles for oxygen evolution in acid and alkaline solutions, *J. Phys. Chem. Lett.* 3 (2012) 399–404. <https://doi.org/10.1021/jz2016507>.
- [4] J. Suntivich, K. J. May, H. A. Gasteiger, J. B. Goodenough, Y. Shao-Horn, A perovskite oxide optimized for oxygen evolution catalysis from molecular orbital principles, *Science* 334 (2011) 1383–1385. <https://doi.org/10.1126/science.1212858>.
- [5] X. Cao, X. Zheng, J. Tian, C. Jin, K. Ke, R. Yang, Cobalt sulfide embedded in porous nitrogen-doped carbon as a bifunctional electrocatalyst for oxygen reduction and evolution reactions, *Electrochim. Acta* 191 (2016) 776–783. <https://doi.org/https://doi.org/10.1016/j.electacta.2016.01.137>.
- [6] T. Liu, Y. Liang, Q. Liu, X. Sun, Y. He, A. M. Asiri, Electrodeposition of cobalt-sulfide nanosheets film as an efficient electrocatalyst for oxygen evolution reaction, *Electrochem. Commun.* 60 (2015) 92–96. <https://doi.org/10.1016/j.elecom.2015.08.011>.
- [7] H. Qian, J. Tang, Z. Wang, J. Kim, J. H. Kim, S. M. Alshehri, E. Yanmaz, X. Wang, Y. Yamauchi, Synthesis of cobalt sulfide/sulfur doped carbon nanocomposites with efficient catalytic activity in the oxygen evolution reaction, *Chem. A Eur. J.* 22 (2016) 18259–18264. <https://doi.org/10.1002/chem.201604162>.
- [8] M. Zhu, Z. Zhang, H. Zhang, H. Zhang, X. Zhang, L. Zhang, S. Wang, Hydrophilic cobalt sulfide nanosheets as a bifunctional catalyst for oxygen and hydrogen evolution in electrolysis of alkaline aqueous solution, *J. Colloid Interface Sci.* 509 (2018) 522–528. <https://doi.org/10.1016/j.jcis.2017.09.076>.
- [9] X. Qiao, J. Jin, H. Fan, Y. Li, S. Liao, In situ growth of cobalt sulfide hollow nanospheres embedded in nitrogen and sulfur co-doped graphene nanoholes as a highly active electrocatalyst for oxygen reduction and evolution, *J. Mater. Chem. A* 5 (2017) 12354–12360. <https://doi.org/10.1039/C7TA00993C>.
- [10] A. M. Elshahawy, X. Li, H. Zhang, Y. Hu, K.H. Ho, C. Guan, J. Wang, Controllable MnCo₂S₄ nanostructures for high performance hybrid supercapacitors, *J. Mater. Chem. A* 5 (2017) 7494–7506. <https://doi.org/10.1039/C7TA00943G>.
- [11] Y. Guo, J. Tang, Z. Wang, Y. Sugahara, Y. Yamauchi, Hollow porous heterometallic phosphide nanocubes for enhanced electrochemical water splitting, *Small* 14 (2018) 1802442 (1–8). <https://doi.org/10.1002/smll.201802442.36>
- [12] P. Ganesan, M. Prabu, J. Sanetuntikul, S. Shanmugam, Cobalt sulfide

- nanoparticles grown on nitrogen and sulfur codoped graphene oxide: an efficient electrocatalyst for oxygen reduction and evolution reactions, *ACS Catal.* 5 (2015) 3625–3637. <https://doi.org/10.1021/acscatal.5b00154>.
- [13] Q. Kong, W. Feng, X. Xie, S. Zhang, X. Yuan, C. Sun, Morphology-controlled synthesis of Co_3O_4 materials and its electrochemical catalytic properties towards oxygen evolution reaction, *Catal. Letters.* 148 (2018) 3771–3778. <https://doi.org/10.1007/s10562-018-2574-2>.
- [14] X. Wu, X. Han, X. Ma, W. Zhang, Y. Deng, C. Zhong, W. Hu, Morphology-controllable synthesis of Zn-Co-Mixed sulfide nanostructures on carbon fiber paper toward efficient rechargeable Zinc-Air batteries and water electrolysis, *ACS Appl. Mater. Interfaces.* 9 (2017) 12574–12583. <https://doi.org/10.1021/acsami.6b16602>.
- [15] E. Samuel, B. Joshi, M. W. Kim, M. T. Swihart, S. S. Yoon, Morphology engineering of photoelectrodes for efficient photoelectrochemical water splitting, *Nano Energy.* 72 (2020) 104648 (1-30). <https://doi.org/10.1016/j.nanoen.2020.104648>.
- [16] S. B. Kale, V. C. Lokhande, S. J. Marje, U. M. Patil, J. H. Kim, C. D. Lokhande, Chemically deposited Co_3S_4 thin film: morphology dependant electrocatalytic oxygen evolution reaction, *Appl. Phys. A Mater. Sci. Process.* 126 (2020) 206 (1-10). <https://doi.org/10.1007/s00339-020-3360-8>.
- [17] Q. Z. Xu, Y. Z. Su, H. Wu, H. Cheng, Y. P. Guo, N. L. and Z. Q. Liu, Effect of morphology of Co_3O_4 for oxygen evolution reaction in alkaline water electrolysis, *Curr. Nanosci.* 11 (2015) 107–112. <https://doi.org/http://dx.doi.org/10.2174/1573413710666140925200938>.
- [18] K. Tao, P. Li, L. Kang, X. Li, Q. Zhou, L. Dong, W. Liang, Facile and low-cost combustion-synthesized amorphous mesoporous NiO /carbon as high mass-loading pseudocapacitor materials, *J. Power Sources.* 293 (2015) 23–32. <https://doi.org/https://doi.org/10.1016/j.jpowsour.2015.05.004>.
- [19] S. Y. Lin, X. Zhang, Two-dimensional titanium carbide electrode with large mass loading for supercapacitor, *J. Power Sources.* 294 (2015) 354–359. <https://doi.org/https://doi.org/10.1016/j.jpowsour.2015.06.082>.
- [20] H. Wang, M. Xu, J. Xu, L. Yang, S. Zhou, Effects of annealing temperature and thickness on microstructure and properties of sol–gel derived multilayer Al-doped ZnO films, *J. Mater. Sci. Mater. Electron.* 21 (2010) 145–148. <https://doi.org/10.1007/s10854-009-9883-6>.
- [21] E. R. Shaaban, N. Afify, A. El-Taher, Effect of film thickness on microstructure parameters and optical constants of CdTe thin films, *J. Alloys Compd.* 482 (2009) 400–404. <https://doi.org/https://doi.org/10.1016/j.jallcom.2009.04.033>.
- [22] L. Y. Huang, L. Meng, Effects of film thickness on microstructure and electrical properties of the pyrite films, *Mater. Sci. Eng. B.* 137 (2007) 310–314. <https://doi.org/https://doi.org/10.1016/j.mseb.2006.11.029>.

- [23] S. J. Marje, P. K. Katkar, S. S. Pujari, S. A. Khalate, A. C. Lokhande, U. M. Patil, Regulated micro-leaf like nickel pyrophosphate as a cathode electrode for asymmetric supercapacitor, *Synth. Met.* 259 (2020) 116224 (1-11). <https://doi.org/10.1016/j.synthmet.2019.116224>.
- [24] H. M. Pathan, C. D. Lokhande, Deposition of metal chalcogenide thin films by successive ionic layer adsorption and reaction (SILAR) method, *Bull. Mater. Sci.* 27 (2004) 85–111. <https://doi.org/10.1007/BF02708491>.
- [25] M. M. Momeni, A. A. Mozafari, The effect of number of SILAR cycles on morphological, optical and photo catalytic properties of cadmium sulfide–titania films, *J. Mater. Sci. Mater. Electron.* 27 (2016) 10658–10666. <https://doi.org/10.1007/s10854-016-5163-4>.
- [26] C. C. L. McCrory, S. Jung, J. C. Peters, T. F. Jaramillo, Benchmarking heterogeneous electrocatalysts for the oxygen evolution reaction, *J. Am. Chem. Soc.* 135 (2013) 16977–16987. <https://doi.org/10.1021/ja407115p>.
- [27] C. Ray, S. C. Lee, K. V. Sankar, B. Jin, J. Lee, J. H. Park, S. C. Jun, Amorphous phosphorus-incorporated cobalt molybdenum sulfide on carbon cloth: An efficient and stable electrocatalyst for enhanced overall water splitting over Entire pH values, *ACS Appl. Mater. Interfaces.* 9 (2017) 37739–37749. <https://doi.org/10.1021/acsami.7b11192>.
- [28] R. Lin, T. Lin, J. Huang, X. Huang, Y. Liu, Hierarchical cobalt sulfide with vertical in-plane edge structure for enhanced electrocatalytic oxygen evolution reaction, *Electrochim. Acta.* 281 (2018) 348–356. <https://doi.org/https://doi.org/10.1016/j.electacta.2018.05.184>.
- [29] H. Liu, F. X. Ma, C. Y. Xu, L. Yang, Y. Du, P. P. Wang, S. Yang, L. Zhen, Sulfurizing-induced hollowing of Co₉S₈ microplates with nanosheet units for highly efficient water oxidation, *ACS Appl. Mater. Interfaces.* 9 (2017) 11634–11641. <https://doi.org/10.1021/acsami.7b00899>.
- [30] X. Feng, Q. Jiao, T. Liu, Q. Li, M. Yin, Y. Zhao, H. Li, C. Feng, W. Zhou, Facile synthesis of Co₉S₈ hollow spheres as a high-performance electrocatalyst for the oxygen evolution reaction, *ACS Sustain. Chem. Eng.* 6 (2018) 1863–1871. <https://doi.org/10.1021/acssuschemeng.7b03236>.

CHAPTER 4

Synthesis, characterization and electrocatalytic OER performance of manganese cobalt sulfide thin film electrode

Chapter 4: Synthesis, characterization and electrocatalytic OER
performance of manganese cobalt sulfide thin film electrode

4.1.	Introduction.....	89
4.2.	Experimental details.....	90
4.2.1.	<i>Chemicals</i>	90
4.2.2.	<i>Synthesis of manganese cobalt sulfide thin films</i>	90
4.3.	Results and discussion.....	92
4.3A.	Physicochemical characterizations.....	92
4.3A.1.	<i>XRD</i>	92
3.3A.2.	<i>Raman spectroscopy</i>	94
3.3A.3.	<i>XPS</i>	95
3.3A.4.	<i>FESEM</i>	97
3.3A.5.	<i>HR-TEM</i>	100
4.3B.	Electrochemical characterizations.....	101
4.3B.1.	<i>LSV and Tafel slope</i>	101
4.3B.2.	<i>ECSA</i>	103
4.3B.3.	<i>EIS and Stability</i>	105
4.4.	Conclusions.....	108
4.5	References.....	109

4.1. Introduction

As hydrogen is a potential alternative to fossil fuels, there is an urgent requirement for its large scale production in an environment-friendly way. In this scenario, electrochemical water splitting is considered the most favorable and practicable technology for the production of hydrogen [1,2]. However, high overpotential (η) and sluggish kinetics of anodic oxygen evolution reaction (OER) are the foremost causes that limit this technique from going commercialized [3,4]. However, the most effective electrocatalysts yet identified for OER are based on very precious and rare elements. Thus, it is well desirable to investigate and develop novel low-cost and efficient materials as alternative electrocatalysts for OER, which can realize large-scale water electrolysis.

From the literature survey of single metal sulfides for electrocatalytic OER reaction (given in chapter one) and from the previous chapter, cobalt sulfide is one of the widely studied materials. Good electrocatalytic performance is the main reason behind this. But it is also observed that binary metal sulfides show better electrochemical performance than single metal sulfides. Therefore, nowadays numerous publications are reported on multi metal sulfides [5-9]. Electronegativity of transition metals plays an important role in the intermediate reactions of OER [10]. Among the first-row transition metal elements, cobalt has slightly high electronegativity (~ 1.9). This results in much stronger binding between the metal atoms and intermediates, which is not favorable for a good electrocatalyst. Therefore, the partial substitution of Co with an element having relatively low electronegativity, such as Mn (~ 1.55) could tune the overall electronegativity and electronic structure of the material. Hence, stoichiometric tailoring of cobalt with manganese can give an optimum condition for intermediate reactions.

The SILAR is one of the useful methods for the deposition of metal chalcogenide thin films. There are few reports on the fabrication of thin films of individual cobalt sulfide [11] and manganese sulfide [12] by the SILAR method. However, by the best of our literature survey, there is no report available for manganese cobalt sulfide with the same method. Therefore, in the present chapter manganese cobalt sulfide thin films are deposited by SILAR method. To obtain the optimum electrochemical performance the amount of manganese and cobalt are varied. The origin of optimal performance was comprehensively scrutinized using detailed physio-chemical and electrochemical analyses. For this, the characterization techniques such as XRD, XPS, FESEM and HR-TEM are used. Electrochemical OER performance is tested in 1 M KOH electrolyte.

4.2. Experimental details

4.2.1. Chemicals

For the synthesis of manganese cobalt sulfide thin film electrodes chloride precursors of cobalt ($\text{CoCl}_2 \cdot 6\text{H}_2\text{O}$), manganese ($\text{MnCl}_2 \cdot 4\text{H}_2\text{O}$) and sulfide precursor (Na_2S) were purchased from Sigma Aldrich, USA and used as received. Stainless steel (SS) substrates of thickness 0.5 mm (purchased from a local supplier) were used for film deposition. Potassium hydroxide (KOH, Sigma Aldrich, USA) was used to prepare an aqueous electrolyte. Entire experiments were conducted with double distilled water (DDW).

4.2.2. Synthesis of manganese cobalt sulfide

Manganese cobalt sulfide thin film electrodes were synthesized by successive ionic layer adsorption and reaction (SILAR) method. The SS substrates were first

wiped with acetone and smoothened with sandpaper prior to an ultra-sonication in DDW (Detailed procedure of substrate cleaning is given in the previous chapter). A 0.1 M anionic solution (serving S^{2-} ions) was formulated by dissolving 0.3902 gm Na_2S flakes in 50 ml DDW. Similarly, 0.1 M cationic solution (serving Co^{2+} and Mn^{2+} ions) was prepared by dissolving stoichiometric amounts of $CoCl_2$ and $MnCl_2$ in 50 ml DDW. For the typical synthesis procedure, the precleaned SS substrate was consecutively dipped in the cationic and anionic solutions for 15s each. After each immersion, the substrate was rinsed through DDW for 10 s. These four immersion steps are regarded as one SILAR deposition cycle. At room temperature, such 100 cycles were repeated to get a uniform deposition of thin film. The adsorption, reaction, and rinsing time in this experiment are optimized by several trials to get uniform and adherent film. In the first beaker, the metal cations (Co^{2+} and Mn^{2+}) are adsorbed on the surface of the substrate and react with newly adsorbed anions (S^-) in the third beaker to form a solid thin film. To probe the compositional effects of electrocatalyst on the physio-chemical and electrochemical properties, the Co/Mn ratio was varied systematically and samples were named as $(Co_xMn_y)S$, where x and y illustrate the ratio of cobalt and manganese present in the precursor solution ($Co:Mn = x:y$) (as shown in table 4.1).

Table 4.1: Sample coding according to the Co/Mn ratio used.

Sample Code (Co_xMn_y)S	Co (x)	Mn (y)
$(Co_1Mn_0)S$	1	0
$(Co_4Mn_1)S$	4	1
$(Co_3Mn_2)S$	3	2
$(Co_2Mn_3)S$	2	3
$(Co_1Mn_4)S$	1	4
$(Co_0Mn_1)S$	0	1

4.3. Results and discussion

4.3A. Physicochemical Characterizations

4.3A.1. X-ray diffraction

The manganese cobalt sulfide thin film electrodes were characterized for the crystallinity and phase structure. The XRD patterns (Figure 4.1) for the entire range of electrodes indicate a single diffraction peak at about 43° , corresponding to crystalline SS substrate. Apart from that, a lack of diffraction peaks from entire electrodes suggests the amorphous nature of deposited material.

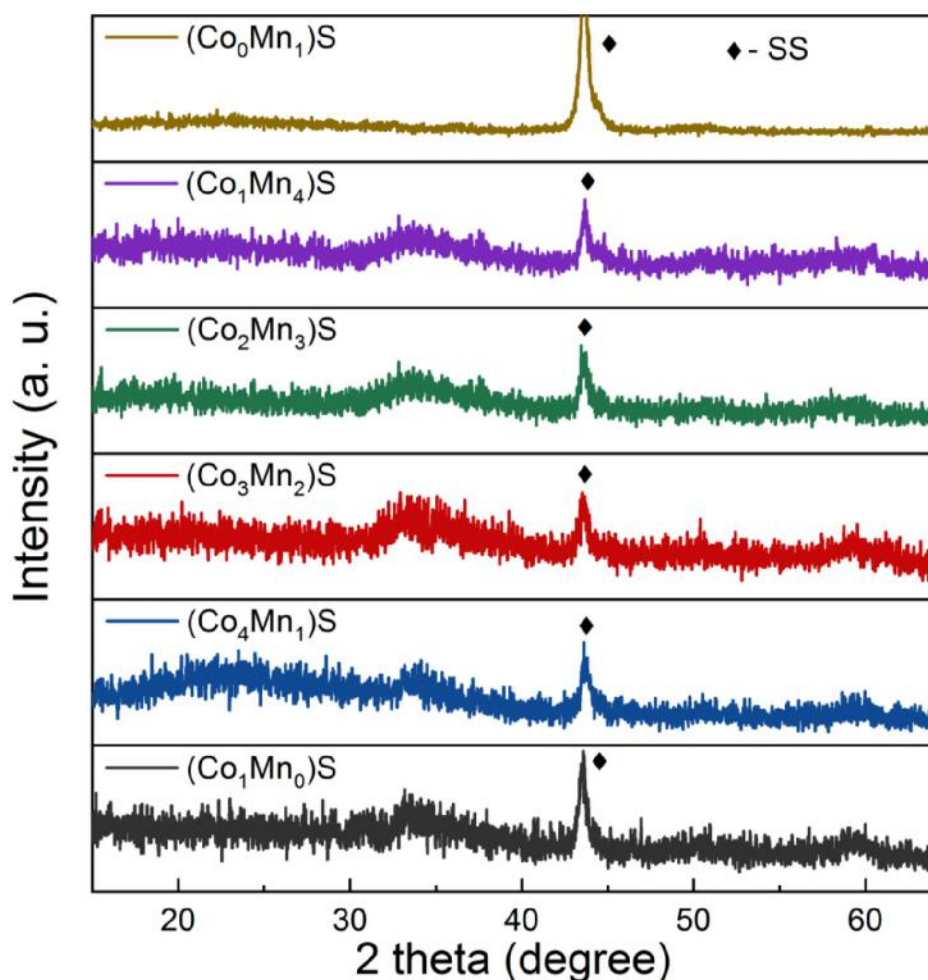


Figure 4.1: XRD patterns of manganese cobalt sulfide thin film electrodes with different Co/Mn ratios.

As aforementioned, the SILAR method is solely based on the adsorption of cations and their prompt reaction with secondly adsorbed anions. In such a deposition process at low temperatures, the adatoms usually do not hold enough mobility to form a crystalline structure. The adatoms of multiple transition metal elements (such as Co and Mn) nonuniformly adsorb on the substrate surface at the initial stage and react with the upcoming S^{2-} anions instantly. As the film growth proceeds, the movement of these atoms is highly restricted due to the limited mobility and absence of sufficient energy (due to low temperature) [13]. As a result, the manganese cobalt sulfide thin film electrodes were found to exhibit amorphous nature. The atomic randomness of electrocatalyst can provided abundant active sites for electrochemical reactions. The atomic composition of the amorphous $(Co_xMn_y)S$ electrocatalysts is measured by EDX spectroscopy. The atomic percentages of Co, Mn, and S for each electrode is represented in Table 4.2.

Table 4.2: Atomic percentage of Co, Mn and S in $(Co_xMn_y)S$ thin film electrodes with different Co/Mn ratios obtained from EDX spectroscopy.

Sample	Atomic percentage		
	S	Co	Mn
$(Co_1Mn_0)S$	67.31	32.69	-
$(Co_4Mn_1)S$	58.88	35.21	5.91
$(Co_3Mn_2)S$	57.30	35.29	7.41
$(Co_2Mn_3)S$	57.11	24.25	18.64
$(Co_1Mn_4)S$	39.33	9.32	51.35
$(Co_0Mn_1)S$	43.07	-	56.93

4.3A.2. Raman spectroscopy

To probe the chemical structure of the electrocatalyst materials, Raman spectroscopy is considered to be a useful tool. The typical Raman spectra for all electrocatalysts materials are shown in Figure 4.2. The most intense peak at 665 cm^{-1} in manganese-free $(\text{Co}_1\text{Mn}_0)\text{S}$ corresponds to Co-S vibrational mode [14]. While, the Raman bands observed at 515.2 cm^{-1} and 467.5 cm^{-1} could be accredited to F_{2g} and E_g bands of cobalt sulfide, respectively [15]. For cobalt-free electrocatalyst $(\text{Co}_0\text{Mn}_1)\text{S}$, the small broad peaks observed at 324.8 and 371 cm^{-1} are accredited to optical phonon modes of transverse and longitudinal vibrations of manganese sulfide, respectively.

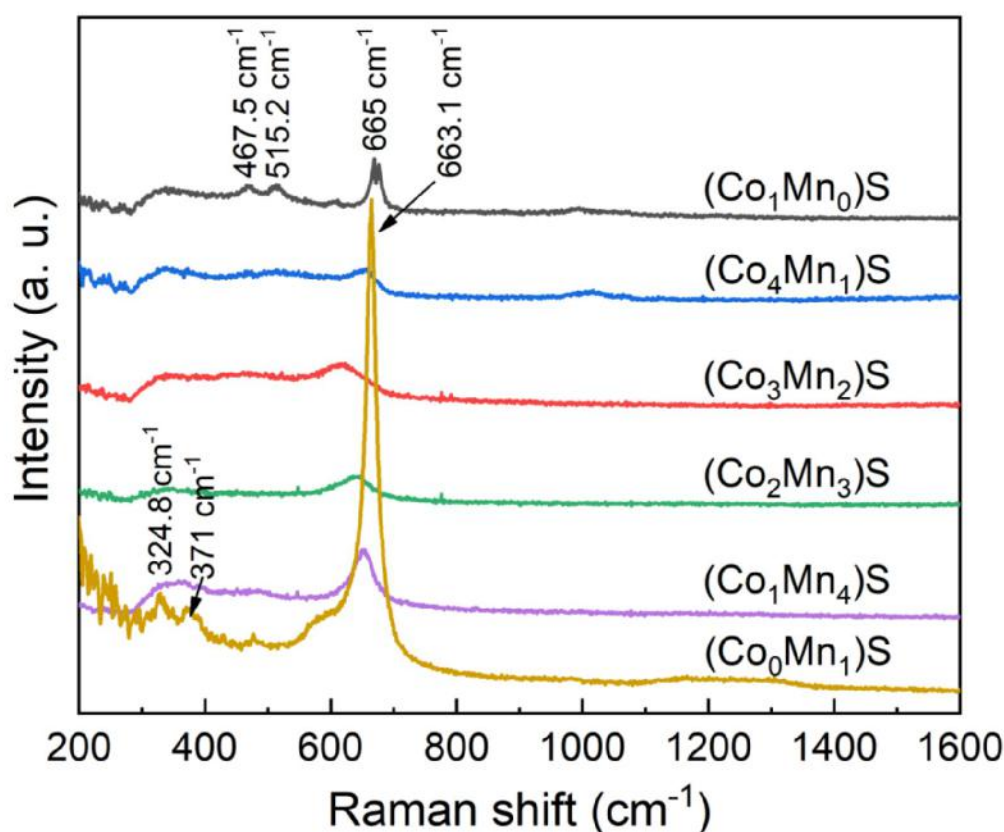


Figure 4.2: Raman spectra of $(\text{Co}_x\text{Mn}_y)\text{S}$ thin film electrodes with different Co/Mn ratios.

While the strong and intense resonance peak at 663.1 cm^{-1} corresponds to

photoluminescence [16].

The Raman spectra of both electrocatalysts with a single metal-atom (Co or Mn) are well-matched with the literature [14–16]. In contrast, the Raman spectra of electrocatalysts comprising dual metal-atoms (Co and Mn) are found to be significantly distinctive to that of the single metal-atom. Increasing the manganese with simultaneously decreasing cobalt concentration results in the shifting of intense peak (Co-S vibration mode) towards lower wavenumber. This shift of peak was found to persist until the concentration of cobalt reached below manganese (Co:Mn=3:2). A further increase in the concentration of manganese results in shifting of the peak towards higher wavenumber. This trend suggestively signifies a formation of a solid-solution of cobalt-manganese sulfide [17].

Along with the peak shifting, the broadening of the peak is also observed for different dual metal-atom (Co/Mn) compositions, which could be attributed to the increased disordering resulted from the random distribution of metal atoms in electrocatalyst and their effect on neighboring metal-sulfur (M-S) bond strength [18]. Also, the peak broadening and shifting indicate a delocalization of electrons induced from the electrocatalyst's compositional variation. Hence, tailoring the metal-ion composition have possibly modified the electronic structure of the electrocatalyst and could be an advantage for improving the electrocatalytic activity for OER

4.3A.3. X-ray photoelectron spectroscopy

The electrochemical activity of sulfide based electrocatalysts is closely controlled by the redox chemical properties and valence states of comprising transition metal atoms. Therefore, to investigate the oxidation states of elements present in amorphous manganese cobalt sulfide thin film electrodes, the XPS

measurement was conducted for $(\text{Co}_3\text{Mn}_2)\text{S}$ electrocatalyst and spectral results were analyzed using CasaXPS software. Figure 4.3(a) shows a survey spectrum that consists of the signals from predominant elements Co, Mn, and S. The broad spectrum of Co 2p exhibits a doublet separated by the binding energy of 16.1 eV owed by spin-orbit split (Figure 4.3(b)). The peak at binding energy ~ 780.8 eV with a shake-up satellite peak at slightly higher (~ 5.1 eV) binding energy (~ 785.9 eV) match with $2p_{3/2}$ level while the peak at ~ 796.9 eV accompanied by shake-up satellite (~ 802.8 eV) corresponds to $2p_{1/2}$ level [19,20].

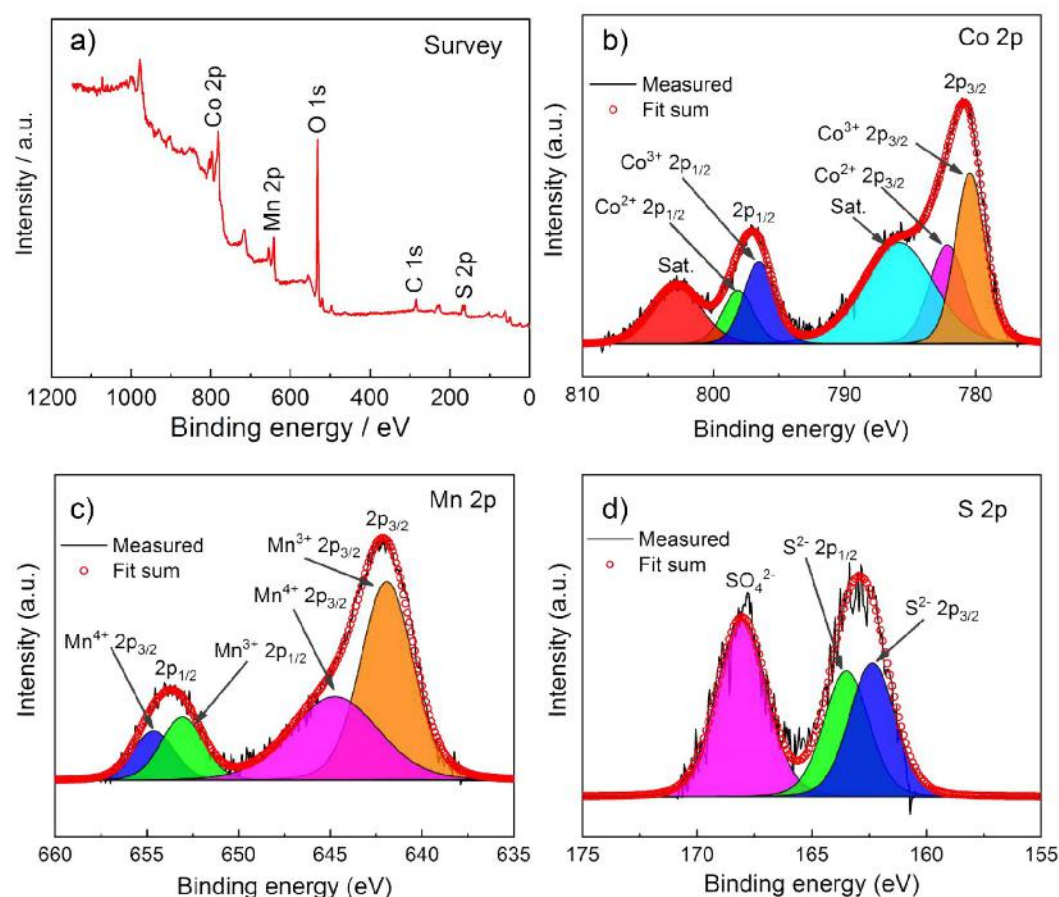


Figure 4.3: a) XPS survey spectrum of $(\text{Co}_3\text{Mn}_2)\text{S}$ thin film electrode. High resolution spectra of b) Co 2p, c) Mn 2p and d) S 2p.

Both the levels of Co 2p are composed of two components. The components at ~ 780.4 and ~ 796.5 eV are attributed to the 13 valence states of Co $2p_{3/2}$ and Co $2p_{1/2}$

configurations, respectively, while the components at ~ 782.2 and ~ 798.1 eV are accredited to the 2^+ valence state of Co $2p_{3/2}$ and Co $2p_{1/2}$ configurations, respectively [21].

The Mn 2p spectrum shown in Figure 4.3(c) also displays a pair of doublets matching with $2p_{3/2}$ and $2p_{1/2}$ levels of Mn at binding energies of ~ 643.2 and ~ 654.6 eV, respectively [22]. Especially for Mn 2p spectrum, satellite peaks are important and can be used as a fingerprint to identify the existence of multiple valence states. Several valence states such as $+2$, $+3$, and $+4$ are common for Mn from which $+2$ state shows satellite feature at slightly higher binding energy from main spin-orbit splitting levels (~ 5 eV) which is not present for either $+3$ or $+4$ states [23]. Therefore, the $2p_{3/2}$ and $2p_{1/2}$ levels of Mn deconvoluted into two peaks, each from which situated at ~ 641.9 and ~ 653.1 eV is assigned to $\text{Mn}^{3+} 2p_{3/2}$ and $\text{Mn}^{3+} 2p_{1/2}$ configurations. In contrast, ~ 644.7 and ~ 654.7 eV are assigned to $\text{Mn}^{4+} 2p_{3/2}$ and $\text{Mn}^{4+} 2p_{1/2}$ configurations, respectively [23–25]. High-resolution spectrum of S 2p (Figure 4.3(d)) displays two features at ~ 162.9 and ~ 168.0 eV matching with $\text{S}^{2-} 2p$ and SO_4^{2-} , respectively [20]. The appearance of the sulfate group could be accredited to the slight oxidation over the electrocatalysts surface [26]. After deconvolution, S 2p peak has closely spaced ($\Delta = \sim 1.15$ eV) spin-orbit components at ~ 162.3 and ~ 163.5 eV and matches with -2 valence states of S $2p_{3/2}$ and S $2p_{1/2}$, respectively. Therefore, it is confirmed that the multivalence states of Co and Mn are coexisting in amorphous $(\text{Co}_3\text{Mn}_2)\text{S}$ electrocatalyst, which could be helpful for the enhancement of its electrochemical activity for OER.

4.3A.4. Field emission scanning electron microscopy

For the heterogeneous catalysis (such as OER), the morphology of

electrocatalyst plays an important role, as it directly reflects the topological characteristics of material exposed to the electrolyte. Figure 4.4 represents the microstructure of amorphous manganese cobalt sulfide thin film electrodes with different cobalt and manganese ratios.

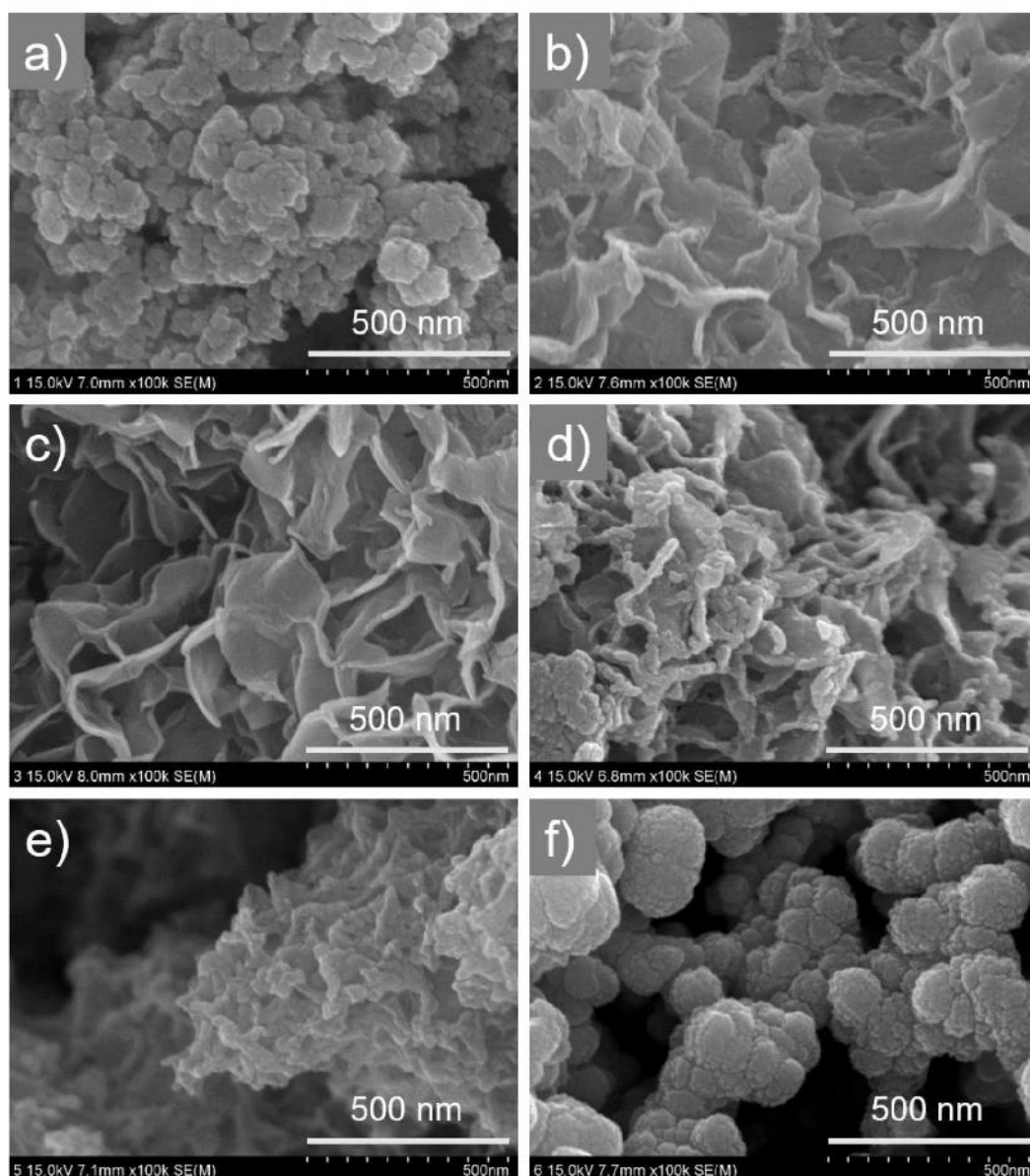


Figure 4.4: FESEM images of $(\text{Co}_x\text{Mn}_y)\text{S}$ thin film electrodes with different Co/Mn ratios, a) $(\text{Co}_1\text{Mn}_0)\text{S}$, b) $(\text{Co}_4\text{Mn}_1)\text{S}$, c) $(\text{Co}_3\text{Mn}_2)\text{S}$, d) $(\text{Co}_2\text{Mn}_3)\text{S}$, e) $(\text{Co}_1\text{Mn}_4)\text{S}$ and f) $(\text{Co}_0\text{Mn}_1)\text{S}$ at 100kX magnification.

In the absence of dual metal atoms, the $(\text{Co}_1\text{Mn}_0)\text{S}$ and $(\text{Co}_0\text{Mn}_1)\text{S}$ thin film electrodes display a compact microstructure (Figures 4.4(a) and 4.4(f)). As a small amount of manganese is added at the expense of cobalt ($(\text{Co}_4\text{Mn}_1)\text{S}$), the microstructure becomes slightly porous and exhibits a partial sheet-like morphology (Figure 4.4(b)). The formation of randomly oriented nanosheets takes place with a further increase in Mn concentration over Co in the ratio of 3:2 ($(\text{Co}_3\text{Mn}_2)\text{S}$). These randomly oriented nanosheets are interconnected in such a way that they construct a house-of-cards sort structure (Figure 4.4(c)). The further increase in the Co/Mn ratio ($(\text{Co}_2\text{Mn}_3)\text{S}$) results in the growth of secondary particles, which disturbs sheet-like structure and blocks the porous structure (Figure 4.4(d)). In $(\text{Co}_1\text{Mn}_4)\text{S}$, manganese dominates the morphology making it compact enough, and no trace of sheet-like structure is observed (Figure 4.4(e)).

Hence, the compositional variations of amorphous manganese cobalt sulfide electrodes not only affect the chemical structure but also modify the microstructure of thin films. Sheet-like morphology of $(\text{Co}_3\text{Mn}_2)\text{S}$ sample can provide considerably large catalytically active surface area and reaction sites for OER. The presence of different elements and their distribution in thin film electrodes are further confirmed by elemental mapping through the EDX technique. The comprising elements; S, Co, and Mn are found to be uniformly distributed in corresponding thin film electrodes (Figure 4.5).

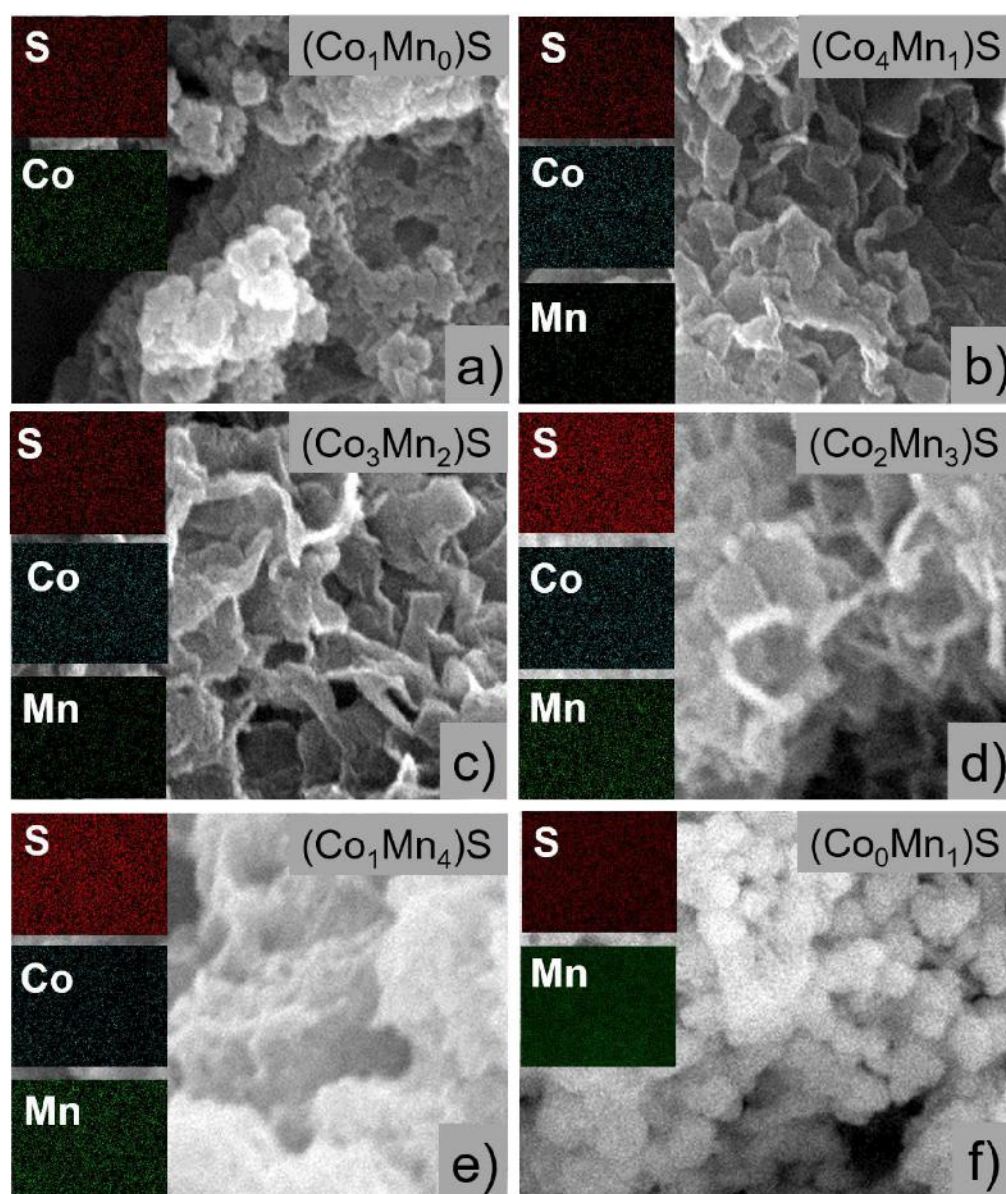


Figure 4.5: EDX elemental mapping of $(\text{Co}_x\text{Mn}_y)\text{S}$ thin film electrodes with different Co/Mn ratios, a) $(\text{Co}_1\text{Mn}_0)\text{S}$, b) $(\text{Co}_4\text{Mn}_1)\text{S}$, c) $(\text{Co}_3\text{Mn}_2)\text{S}$, d) $(\text{Co}_2\text{Mn}_3)\text{S}$, e) $(\text{Co}_1\text{Mn}_4)\text{S}$, and f) $(\text{Co}_0\text{Mn}_1)\text{S}$.

4.3A.5. High-resolution transmission electron microscopy

Figure 4.6(a) shows the HRTEM image of $(\text{Co}_3\text{Mn}_2)\text{S}$ thin film electrode. The non-apparent and disordered moiré-fringe pattern observed at the edge of the nanosheet depicts the lack of ordered arrangement of atoms in it. Also, in the reverse

space of the lattice planes, a weak and diffused SAED pattern (Figure 4.6(b)) is found.

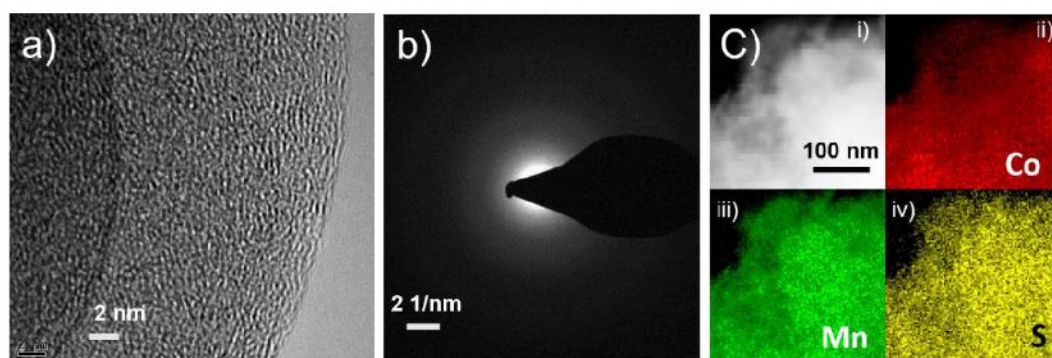


Figure 4.6: a) HR-TEM image, b) SAED pattern and c) (i) HAADF-STEM and (ii, iii iv) EDX elemental mapping of $(\text{Co}_3\text{Mn}_2)\text{S}$ thin film electrode.

The absence of lattice fringe at the thin film surface and diffused SAED pattern confirm that $(\text{Co}_3\text{Mn}_2)\text{S}$ thin film electrode is amorphous, with consistency to the XRD analysis. Figure 4.6 (c) (i) show HAADF-STEM image of a small area of $(\text{Co}_3\text{Mn}_2)\text{S}$. Energy-dispersive X-ray spectroscopy (EDX) elemental mappings of Co, Mn and S over the same area are shown in Figure 4.6 (c) (ii), (iii) and (iv), respectively. The elemental mapping over the HAADF-STEM image proves the uniform distribution of elements (Mn, Co, and S) in the nanosheet structure.

4.3B. Electrochemical characterizations

4.3B.1. Linear sweep voltammetry and Tafel slope

The catalytic activity of amorphous $(\text{Co}_x\text{Mn}_y)\text{S}$ thin film electrodes towards OER was evaluated in an alkaline electrolyte. As observed in polarization curves, Figure 4.7(a) shows LSV curves for $(\text{Co}_x\text{Mn}_y)\text{S}$ electrocatalysts with different Co/Mn ratios. The overpotential required to reach a current density of 10 mA cm^{-2} is calculated for all electrocatalysts using equation (2.5). Figure 4.7(b) shows the overpotential required for $(\text{Co}_x\text{Mn}_y)\text{S}$ thin film electrocatalysts prepared with different

Co/Mn ratios, from which the $(\text{Co}_3\text{Mn}_2)\text{S}$ was found to require 250 mV to reach 10 mA cm^{-2} , while $(\text{Co}_1\text{Mn}_0)\text{S}$, $(\text{Co}_4\text{Mn}_1)\text{S}$, $(\text{Co}_2\text{Mn}_3)\text{S}$, $(\text{Co}_1\text{Mn}_4)\text{S}$ and $(\text{Co}_0\text{Mn}_1)\text{S}$ require 280, 270, 263, 290 and 348 mV overpotential, respectively. Hence, $(\text{Co}_3\text{Mn}_2)\text{S}$ requires the lowest overpotential among all electrodes. Figure 4.7 (c) shows the Tafel plots for all electrocatalysts, extracted from corresponding LSV curves. The value of Tafel slope obtained for $(\text{Co}_1\text{Mn}_0)\text{S}$, $(\text{Co}_4\text{Mn}_1)\text{S}$, $(\text{Co}_3\text{Mn}_2)\text{S}$, $(\text{Co}_2\text{Mn}_3)\text{S}$, $(\text{Co}_1\text{Mn}_4)\text{S}$ and $(\text{Co}_0\text{Mn}_1)\text{S}$ electrocatalyst is 106, 99, 98, 99, 108 and 117 mV dec^{-1} .

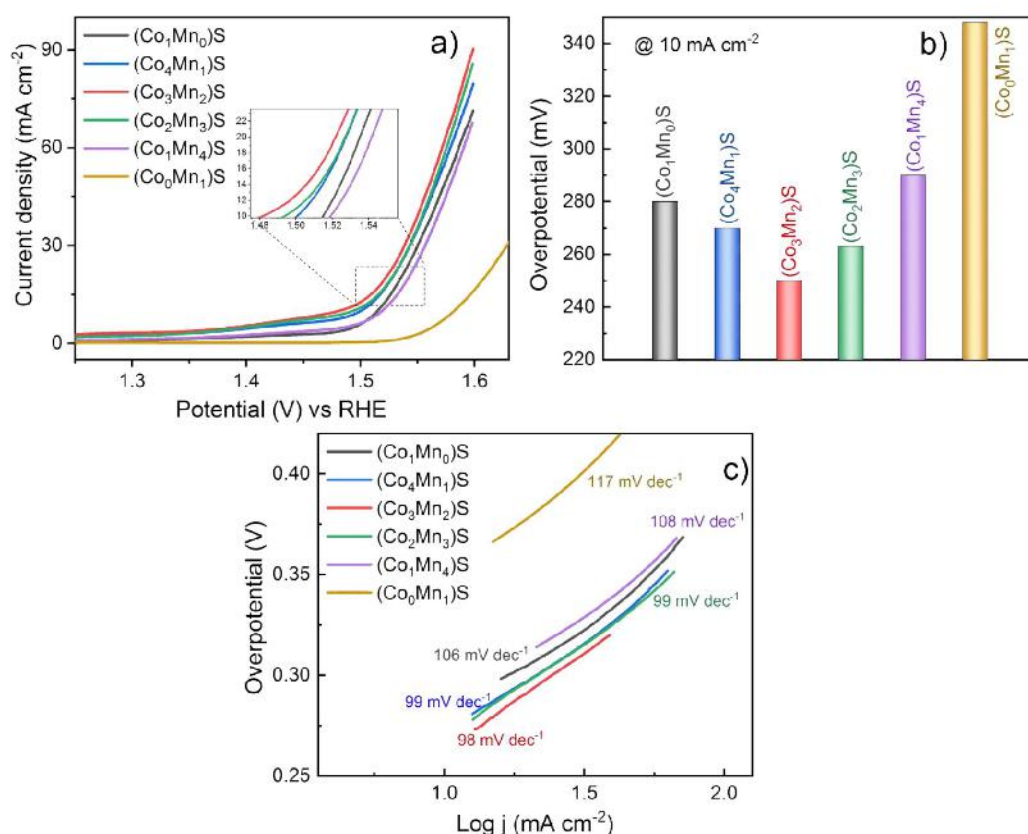


Figure 4.7: Electrochemical OER performance of $(\text{Co}_x\text{Mn}_y)\text{S}$ thin film electrocatalysts with different Co/Mn ratios, a) LSV curves with the magnified view shown inset, b) overpotential required to reach 10 mA cm^{-2} current density and c) Tafel slope.

The trend in OER activity for $(\text{Co}_x\text{Mn}_y)\text{S}$ thin film electrocatalysts with different Co/Mn ratios is in the order of $(\text{Co}_1\text{Mn}_0)\text{S} < (\text{Co}_4\text{Mn}_1)\text{S} < (\text{Co}_3\text{Mn}_2)\text{S} > (\text{Co}_2\text{Mn}_3)\text{S} >$

$(\text{Co}_1\text{Mn}_4)\text{S} > (\text{Co}_0\text{Mn}_1)\text{S}$. This indicates that tuning the chemical composition of the transition metal sulfide-based electrocatalysts could be one of the key-strategies towards developing an efficient electrocatalyst for water electrolysis application [27].

4.3B.2. Electrochemical active surface area

The electrochemically active surface area (ECSA) for $(\text{Co}_x\text{Mn}_y)\text{S}$ thin film electrocatalysts is estimated from the double layer capacitance (C_{dl}) of the electrode material. Thus, cyclic voltammograms (CVs) were recorded at numerous scanning rates ($10\text{--}100\text{ mV s}^{-2}$) in the non-faradaic region of potential (0.00 to $+0.15\text{ V vs SCE}$). Figures 4.8(a)-4.8(f) show CV curves of $(\text{Co}_x\text{Mn}_y)\text{S}$ thin film electrocatalysts with different Co/Mn ratios, in the potential range of 0.00 to $+0.15\text{ V vs. SCE}$. The inset of each figure shows the corresponding plot of current density measured at a fixed potential of $+0.12\text{ V vs scan rate (v)}$. The slope of linear fitting to the measured values represents the double layer capacitance (C_{dl}). Figure 4.9 shows the ECSA for $(\text{Co}_x\text{Mn}_y)\text{S}$ thin film electrocatalysts calculated from C_{dl} . The ECSA value obtained for $(\text{Co}_1\text{Mn}_0)\text{S}$, $(\text{Co}_4\text{Mn}_1)\text{S}$, $(\text{Co}_3\text{Mn}_2)\text{S}$, $(\text{Co}_2\text{Mn}_3)\text{S}$, $(\text{Co}_1\text{Mn}_4)\text{S}$ and $(\text{Co}_0\text{Mn}_1)\text{S}$ electrocatalysts is 88.5 , 165.5 , 280.1 , 195.3 , 153.2 , 52.7 cm^2 , respectively. Hence, $(\text{Co}_3\text{Mn}_2)\text{S}$ exhibits maximum ECSA than that of the other electrocatalysts. These results can be directly bridged to the microstructure of electrocatalysts observed in FESEM images. Nanosheets of $(\text{Co}_3\text{Mn}_2)\text{S}$ have provided a larger surface area which helps to uncover maximum active sites available in material to electrolyte and lead to higher ECSA.

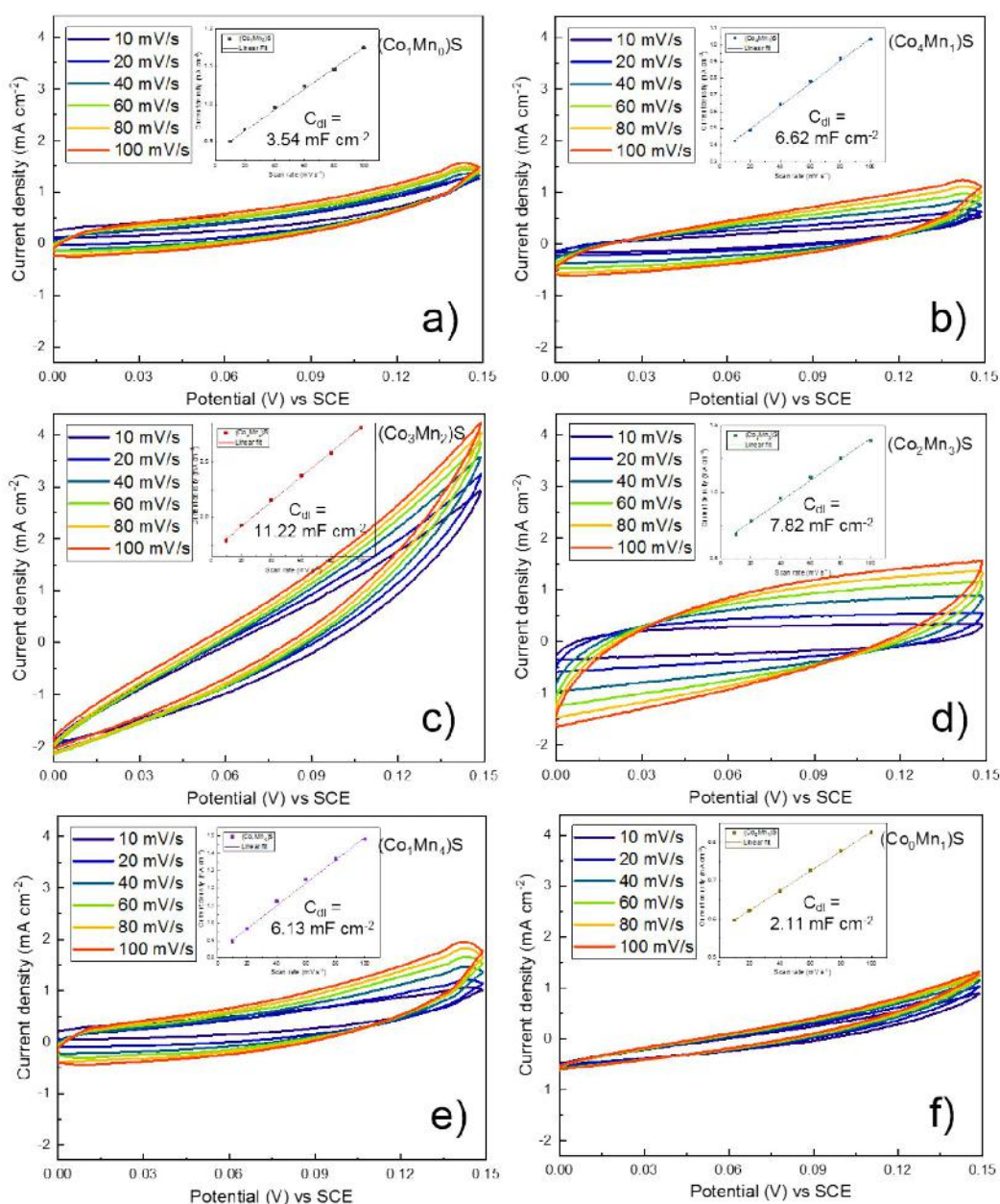


Figure 4.8: Cyclic voltammograms in the potential window of 0.00 to +0.15 V vs. SCE for a) $(\text{Co}_1\text{Mn}_0)\text{S}$, b) $(\text{Co}_4\text{Mn}_1)\text{S}$, c) $(\text{Co}_3\text{Mn}_2)\text{S}$, d) $(\text{Co}_2\text{Mn}_3)\text{S}$, e) $(\text{Co}_1\text{Mn}_4)\text{S}$, and f) $(\text{Co}_0\text{Mn}_5)\text{S}$ thin film electrocatalysts with corresponding current density (at +0.12 V vs. SCE) vs. scan rate plots shown in insets.

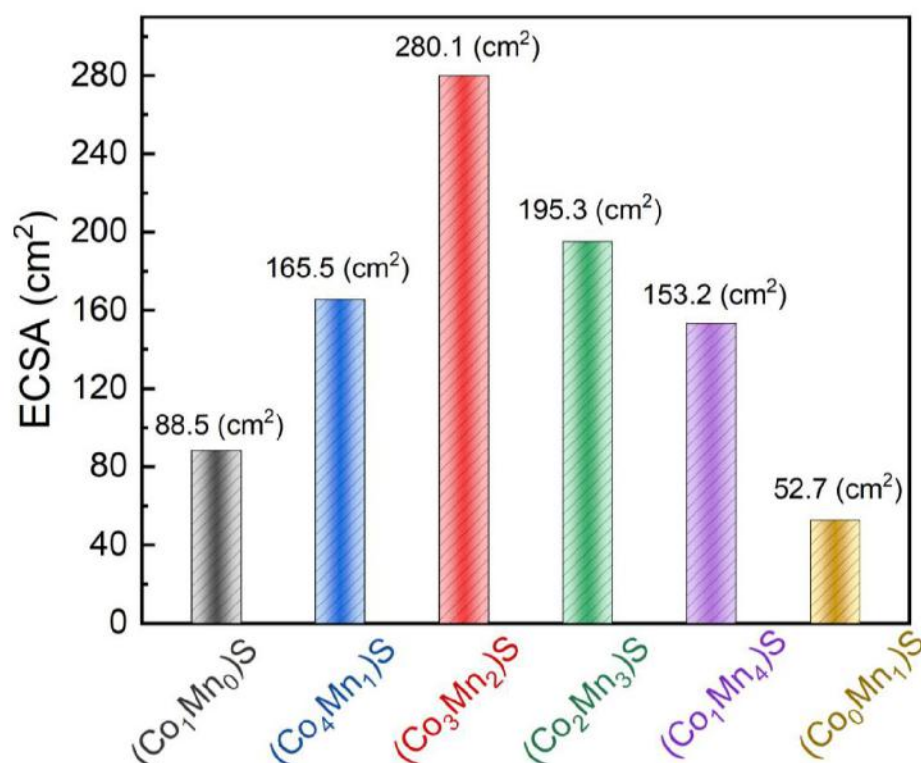


Figure 4.9: Electrochemical active surface area of $(\text{Co}_x\text{Mn}_y)\text{S}$ thin film electrocatalysts with different Co/Mn ratios.

4.3B.3. Electrochemical impedance spectroscopy and Stability

To evaluate different resistances of amorphous $(\text{Co}_x\text{Mn}_y)\text{S}$ thin film electrocatalysts, electrochemical impedance spectroscopy (EIS) was employed. The Nyquist plots for $(\text{Co}_x\text{Mn}_y)\text{S}$ thin film electrocatalysts are presented in Figure 4.10(a). For instance, the maximum and minimum impedance are observed for $(\text{Co}_0\text{Mn}_1)\text{S}$ and $(\text{Co}_3\text{Mn}_2)\text{S}$ electrocatalysts, respectively. Further to quantify the impedance parameters, the Nyquist plots were fitted with an appropriate equivalent circuit model (ECM), as shown in Figure 4.10(b), where the resistive components, R_s , R_f , and R_{ct} , represents the resistance associated with the electrolyte, thin film, and charge-transfer, respectively [28] W_s represents the diffusional component of the impedance. Also, C_f and C_{dl} represent the capacitance of the thin film and electrical double layer,

respectively.

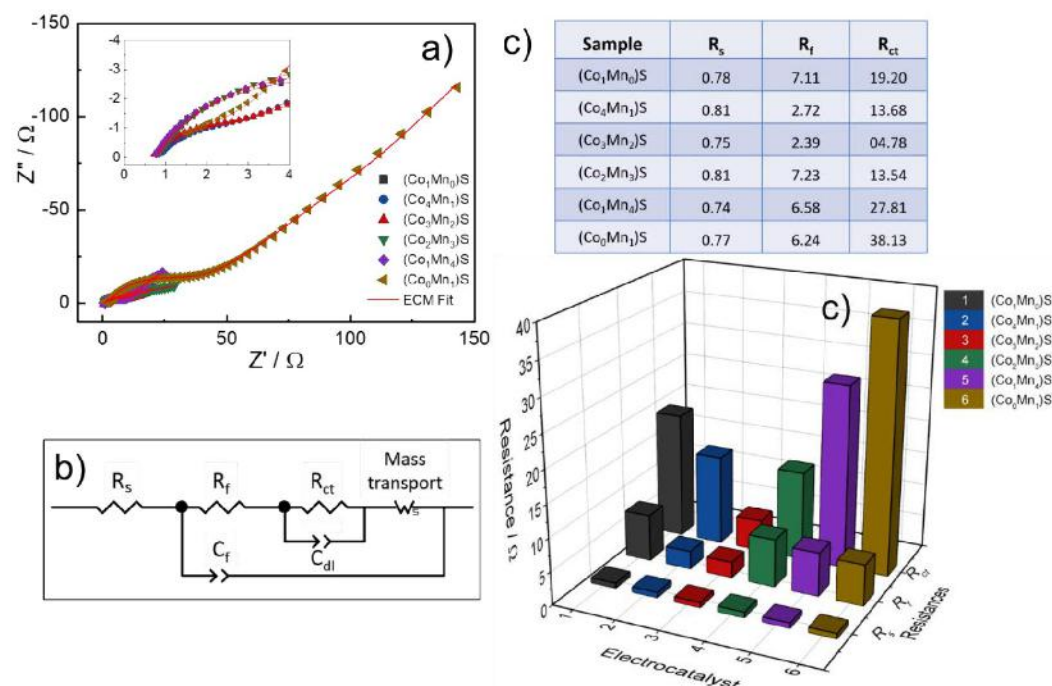


Figure 4.10: Electrochemical impedance spectroscopy study of (Co_xMn_y)S thin film electrocatalysts prepared at different Co/Mn ratios, a) Nyquist plots, b) equivalent circuit model (ECM), c) and d) values of different polarization resistances obtained by ECM fitting.

Various polarization resistances quantified for each of the electrocatalyst using the equivalent circuit model (ECM) fitting are shown in Figure 4.10(c and d). Since R_e is solely related to the electrolyte resistance, it was found independent of the composition of the electrocatalyst. The values of R_f and R_{ct} for (Co₁Mn₀)S, (Co₄Mn₁)S, (Co₃Mn₂)S, (Co₂Mn₃)S, (Co₁Mn₄)S and (Co₀Mn₁)S electrocatalysts are (7.11 and 19.20 Ω), (2.72 and 13.68 Ω), (2.39 and 04.78 Ω), (7.23 and 13.54 Ω), (6.58 and 27.81 Ω) and (6.24 and 38.13 Ω), respectively. Hence, the resistances associated with the thin film and charge transfer were greatly reduced with the substitution of Co for Mn, upto a ratio of 3:2, possibly attributed to the modulation of electronic structure in thin film electrocatalysts.

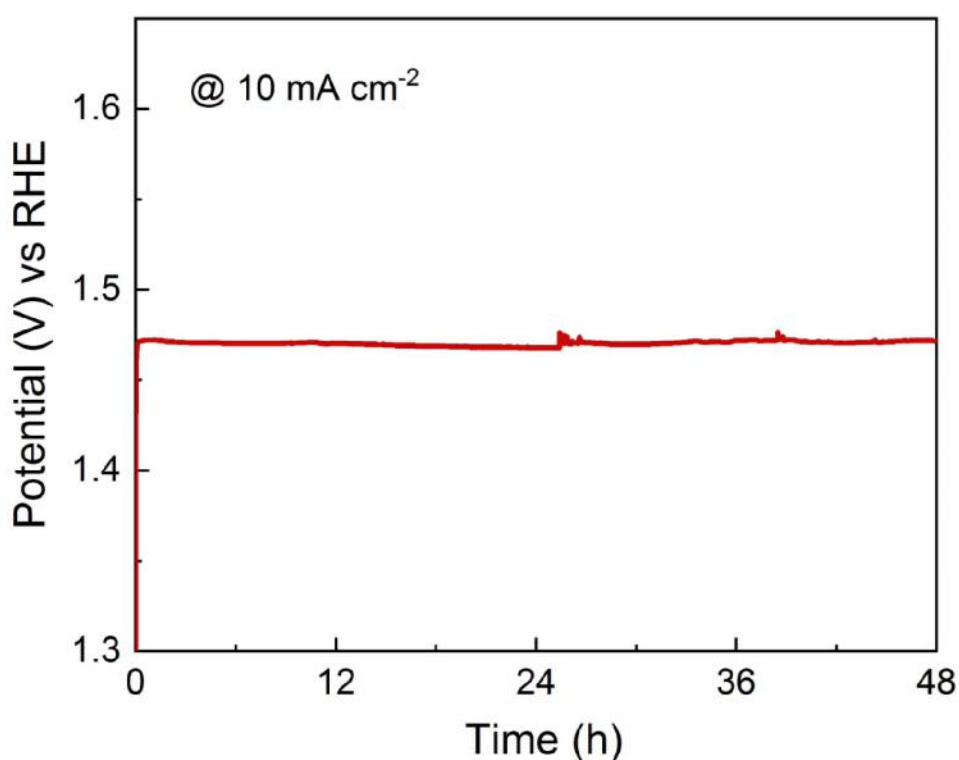


Figure 4.11: Long term durability performance of $(\text{Co}_3\text{Mn}_2)\text{S}$ thin film electrocatalyst at 10 mA cm^{-2} .

The stability of electrocatalyst is a critical parameter to evaluate its feasibility for practical application. Therefore, the stability of $(\text{Co}_3\text{Mn}_2)\text{S}$ thin film electrocatalyst under continuous OER operation was studied using chronopotentiometry measurements at 10 mA cm^{-2} (Figure 4.11). The potential needed was found to be precisely steady for over 48 h without any apparent drop, demonstrating excellent stability of the electrocatalyst material.

The amorphous manganese cobalt sulfide thin film electrocatalyst prepared by SILAR method in present study shows good performance ($250 \text{ mV @ } 10 \text{ mA cm}^{-2}$) than the MnCo_2S_4 nanowires ($300 \text{ mV @ } 10 \text{ mA cm}^{-2}$) prepared on Ti mesh by Zhang et. al. [9]. But when compared with the cobalt-manganese sulfide nanosheets ($298 \text{ mV @ } 100 \text{ mA cm}^{-2}$) prepared on Ni foam by Li et. al. [8], amorphous manganese

cobalt sulfide thin film electrocatalyst shows high overpotential and also doesn't reach to high current density of 100 mA cm^{-2} . The Ni foam possibly played an important role in high electrochemical performance of cobalt-manganese sulfide nanosheets prepared by Li et. al [8].

4.4. Conclusions

In summary, an amorphous solid solution of manganese cobalt sulfide thin film electrocatalysts were synthesized by a scalable and binder free SILAR method. The composition of transition metals is optimized, and the morphology of the electrocatalyst is tuned. Impressively, when used for water oxidation, the amorphous $(\text{Co}_3\text{Mn}_2)\text{S}$ thin film electrocatalyst exhibits superior performance with excellent stability for 48 hours in an alkaline medium. Indeed, the electrocatalyst $(\text{Co}_3\text{Mn}_2)\text{S}$ realized a benchmarking 10 mA cm^{-2} current density by an overpotential as low as 243 mV. While probing the origin of optimal performance, it was found that the stoichiometric tuning of composition has influenced the redox chemical properties of the electrocatalyst significantly and modified their bonding strengths with the intermediates. The atomic randomness of electrocatalyst provided abundant active sites tailored into sheet-like morphology and furnished with the multiple oxidation states of the transition metal atoms. As a result, maximum active sites are exposed to the electrolyte with improved electrocatalytic activity. Considering the simple and scalable approach of synthesis, and excellent OER performance, the amorphous manganese cobalt sulfide thin film electrocatalyst could be considered as a promising candidate for the widespread application of OER.

4.5 References

- [1] M. Chauhan, K. P. Reddy, C. S. Gopinath, S. Deka, Copper cobalt sulfide nanosheets realizing a promising electrocatalytic oxygen evolution reaction, *ACS Catal.* 7 (2017) 5871–5879. <https://doi.org/10.1021/acscatal.7b01831>.
- [2] L. Kuai, J. Geng, C. Chen, E. Kan, Y. Liu, Q. Wang, B. Geng, A reliable aerosol-spray-assisted approach to produce and optimize amorphous metal oxide catalysts for electrochemical water splitting, *Angew. Chem. - Int. Ed.* 53 (2014) 7547–7551. <https://doi.org/10.1002/anie.201404208>.
- [3] N. T. Suen, S. F. Hung, Q. Quan, N. Zhang, Y. J. Xu, H. M. Chen, Electrocatalysis for the oxygen evolution reaction: Recent development and future perspectives, *Chem. Soc. Rev.* 46 (2017) 337–365. <https://doi.org/10.1039/c6cs00328a>.
- [4] S. B. Kale, A. C. Lokhande, R. B. Pujari, C. D. Lokhande, Effect of pretreatment on catalytic activity of cobalt sulfide thin film for oxygen evolution reaction, *Mater. Lett.* 228 (2018) 418–420. <https://doi.org/10.1016/j.matlet.2018.06.035>.
- [5] Y. R. Hong, S. Mhin, K. M. Kim, W. S. Han, H. Choi, G. Ali, K. Y. Chung, H. J. Lee, S. I. Moon, S. Dutta, S. Sun, Y. G. Jung, T. Song, H. S. Han, Electrochemically activated cobalt nickel sulfide for an efficient oxygen evolution reaction: Partial amorphization and phase control, *J. Mater. Chem. A.* 7 (2019) 3592–3602. <https://doi.org/10.1039/c8ta10142f>.
- [6] V. Ganesan, P. Ramasamy, J. Kim, Hierarchical $\text{Ni}_{3.5}\text{Co}_{5.5}\text{S}_8$ nanosheet-assembled hollow nanocages: Superior electrocatalyst towards oxygen evolution reaction, *Int. J. Hydrogen Energy.* 42 (2017) 5985–5992. <https://doi.org/10.1016/j.ijhydene.2016.12.060>.
- [7] Z. Yu, Y. Bai, S. Zhang, Y. Liu, N. Zhang, K. Sun, MOF-directed templating synthesis of hollow nickel-cobalt sulfide with enhanced electrocatalytic activity for oxygen evolution, *Int. J. Hydrogen Energy.* 43 (2018) 8815–8823. <https://doi.org/10.1016/j.ijhydene.2018.03.154>.
- [8] J. Li, W. Xu, J. Luo, D. Zhou, D. Zhang, L. Wei, P. Xu, D. Yuan, Synthesis of 3D hexagram-like cobalt–manganese sulfides nanosheets grown on nickel foam: A bifunctional electrocatalyst for overall water splitting, *Nano-Micro Lett.* 10 (2017) 6 (1–10). <https://doi.org/10.1007/s40820-017-0160-6>.
- [9] X. Zhang, C. Si, X. Guo, R. Kong, F. Qu, A MnCo_2S_4 nanowire array as an earth-abundant electrocatalyst for an efficient oxygen evolution reaction under alkaline conditions, *J. Mater. Chem. A.* 5 (2017) 17211–17215. <https://doi.org/10.1039/c7ta04804a>.
- [10] S. Anantharaj, S. R. Ede, K. Sakthikumar, K. Karthick, S. Mishra, S. Kundu, Recent trends and perspectives in electrochemical water splitting with an emphasis on sulfide, selenide, and phosphide catalysts of Fe, Co, and Ni: A

- review, ACS Catal. 6 (2016) 8069–8097. <https://doi.org/10.1021/acscatal.6b02479>.
- [11] S. D. Sartale, C. D. Lokhande, Deposition of cobalt sulphide thin films by successive ionic layer adsorption and reaction (SILAR) method and their characterization, Indian J. Pure Appl. Phys. 38 (2000) 48–52.
- [12] S. J. Marje, P. K. Katkar, S. B. Kale, A. C. Lokhande, C. D. Lokhande, U. M. Patil, Effect of phosphate variation on morphology and electrocatalytic activity (OER) of hydrous nickel pyrophosphate thin films, J. Alloys Compd. 779 (2019) 49–58. <https://doi.org/10.1016/j.jallcom.2018.11.213>.
- [13] D. M. Mattox, Atomistic film growth and some growth-related film properties, in: D.M.B.T.-H. of P.V.D. (PVD) P. (Second E. Mattox (Ed.), Handb. Phys. Vap. Depos. Process., William Andrew Publishing, Boston, 2010: pp. 333–398. <https://doi.org/10.1016/b978-0-8155-2037-5.00010-1>.
- [14] X. Cai, X. Shen, L. Ma, Z. Ji, L. kong, Facile synthesis of nickel–cobalt sulfide/reduced graphene oxide hybrid with enhanced capacitive performance, RSC Adv. 5 (2015) 58777–58783. <https://doi.org/10.1039/c5ra09447j>.
- [15] C. Y. Chen, Z. Y. Shih, Z. Yang, H. T. Chang, Carbon nanotubes/cobalt sulfide composites as potential high-rate and high-efficiency supercapacitors, J. Power Sources. 215 (2012) 43–47. <https://doi.org/10.1016/j.jpowsour.2012.04.075>.
- [16] A. Anastassiadou, E. Liarokapis, E. Anastassakis, A Raman study of $Zn_{1-x}Mn_xS$ mixed crystals, Solid State Commun. 69 (1989) 137–142. [https://doi.org/10.1016/0038-1098\(89\)90378-5](https://doi.org/10.1016/0038-1098(89)90378-5).
- [17] C. D. Curran, L. Lu, C. J. Kiely, S. McIntosh, Ambient temperature aqueous synthesis of ultrasmall copper doped ceria nanocrystals for the water gas shift and carbon monoxide oxidation reactions, J. Mater. Chem. A. 6 (2017) 244–255. <https://doi.org/10.1039/c7ta07665g>.
- [18] N. Kornienko, J. Resasco, N. Becknell, C. M. Jiang, Y. S. Liu, K. Nie, X. Sun, J. Guo, S. R. Leone, P. Yang, Operando spectroscopic analysis of an amorphous cobalt sulfide hydrogen evolution electrocatalyst, J. Am. Chem. Soc. 137 (2015) 7448–7455. <https://doi.org/10.1021/jacs.5b03545>.
- [19] Z. Dai, H. Geng, J. Wang, Y. Luo, B. Li, Y. Zong, J. Yang, Y. Guo, Y. Zheng, X. Wang, Q. Yan, Hexagonal-phase cobalt monophosphosulfide for highly efficient overall water splitting, ACS Nano. 11 (2017) 11031–11040. <https://doi.org/10.1021/acsnano.7b05050>.
- [20] M. Al-Mamun, Y. Wang, P. Liu, Y. L. Zhong, H. Yin, X. Su, H. Zhang, H. Yang, D. Wang, Z. Tang, H. Zhao, One-step solid phase synthesis of a highly efficient and robust cobalt pentlandite electrocatalyst for the oxygen evolution reaction, J. Mater. Chem. A. 4 (2016) 18314–18321. <https://doi.org/10.1039/C6TA07962H>.
- [21] H. Li, S. Chen, Y. Zhang, Q. Zhang, Q. Zhang, X. Jia, L. Gu, X. Sun, L. Song, X. Wang, Systematic design of superaerophobic nanotube-array electrode

- comprised of transition-metal sulfides for overall water splitting, *Nat. Commun.* 9 (2018) 2452 (1–12). <https://doi.org/10.1038/s41467-018-04888-0>.
- [22] X. Wang, Q. Zhang, J. Sun, Z. Zhou, Q. Li, B. He, J. Zhao, W. Lu, C. P. Wong, Y. Yao, Facile synthesis of hierarchical porous manganese nickel cobalt sulfide nanotube arrays with enhanced electrochemical performance for ultrahigh energy density fiber-shaped asymmetric supercapacitors, *J. Mater. Chem. A* 6 (2018) 8030–8038. <https://doi.org/10.1039/c8ta01440j>.
- [23] M. C. Biesinger, B. P. Payne, A. P. Grosvenor, L. W. M. Lau, A. R. Gerson, R. S. C. Smart, Resolving surface chemical states in XPS analysis of first row transition metals, oxides and hydroxides: Cr, Mn, Fe, Co and Ni, *Appl. Surf. Sci.* 257 (2011) 2717–2730. <https://doi.org/10.1016/j.apsusc.2010.10.051>.
- [24] X. Zhang, P. Yu, H. Zhang, D. Zhang, X. Sun, Y. Ma, Rapid hydrothermal synthesis of hierarchical nanostructures assembled from ultrathin birnessite-type MnO_2 nanosheets for supercapacitor applications, *Electrochim. Acta* 89 (2013) 523–529. <https://doi.org/10.1016/j.electacta.2012.11.089>.
- [25] H. Chen, M. Q. Wang, Y. Yu, H. Liu, S. Y. Lu, S. J. Bao, M. Xu, Assembling hollow cobalt sulfide nanocages array on graphene-like manganese dioxide nanosheets for superior electrochemical capacitors, *ACS Appl. Mater. Interfaces* 9 (2017) 35040–35047. <https://doi.org/10.1021/acsami.7b12069>.
- [26] M. Cabán-Acevedo, M. L. Stone, J. R. Schmidt, J. G. Thomas, Q. Ding, H. C. Chang, M. L. Tsai, H. He, S. Jin, Efficient hydrogen evolution catalysis using ternary pyrite-type cobalt phosphosulphide, *Nat. Mater.* 14 (2015) 1245–1251. <https://doi.org/10.1038/nmat4410>.
- [27] H. Liu, Q. He, H. Jiang, Y. Lin, Y. Zhang, M. Habib, S. Chen, L. Song, Electronic structure reconfiguration toward pyrite NiS_2 via engineered heteroatom defect boosting overall water splitting, *ACS Nano* 11 (2017) 11574–11583. <https://doi.org/10.1021/acs.nano.7b06501>.
- [28] M. F. G. Lyons, M. P. Brandon, The significance of electrochemical impedance spectra recorded during active oxygen evolution for oxide covered Ni, Co and Fe electrodes in alkaline solution, *J. Electroanal. Chem.* 631 (2009) 62–70. <https://doi.org/10.1016/j.jelechem.2009.03.019>.

CHAPTER 5

Synthesis, characterization and electrocatalytic OER performance of nickel manganese cobalt sulfide /rGO thin film electrode

**Chapter 5: Synthesis, characterization and electrocatalytic OER performance
of nickel manganese cobalt sulfide/rGO composite thin film electrode**

5.1.	Introduction.....	113
------	-------------------	-----

Part A: Optimization of nickel manganese cobalt sulfide thin film electrode

5A.1.	Experimental details.....	114
5A.1.1.	<i>Chemicals</i>	114
5A.1.2.	<i>Synthesis of nickel manganese cobalt sulfide thin films...</i>	115
5A.2.	Results and discussion.....	115
5A.2A.	Physicochemical Characterizations.....	115
5A.2A.1.	<i>XRD and EDX</i>	115
5A.2A.2.	<i>XPS</i>	117
5A.2A.3.	<i>FESEM</i>	119
5A.2A.4.	<i>TEM</i>	120
5A.2B.	Electrochemical characterizations.....	121
5A.2B.1.	<i>LSV and Tafel slope</i>	121
5A.2B.2.	<i>EIS</i>	123

**Part B: Synthesis, characterization and electrocatalytic OER performance
of nickel manganese cobalt sulfide/rGO composite thin film electrode**

5B.1.	Experimental details.....	124
5B.1.1.	<i>Chemicals</i>	124
5B.1.2.	<i>Thermal reduction of graphene oxide</i>	124
5B.1.3.	<i>Synthesis of nickel manganese cobalt sulfide/rGO composite thin films</i>	125
5B.2.	Results and discussion.....	125

5B.2A.	Physicochemical Characterizations.....	125
5B.2A.1.	<i>XRD</i>	125
5B.2A.2.	<i>Raman spectroscopy</i>	128
5B.2A.3.	<i>XPS</i>	129
5B.2A.4.	<i>FESEM</i>	131
5B.2B.	Electrochemical characterizations.....	134
5B.2B.1.	<i>LSV and Tafel slope</i>	134
5B.2B.2.	<i>ECSA</i>	135
5B.2B.3.	<i>EIS and Stability</i>	136
5.2.	Conclusions.....	139
5.3	References.....	139

5.1. Introduction

The electrolysis of water provides a powerful pathway for the storage and conversion of clean and renewable energy. However, high overpotential (η) and sluggish kinetics of anodic half-reaction i.e. oxygen evolution reaction (OER) are the foremost causes that limit this technique from going commercialized [1,2]. Therefore, it is desirable to search for low-cost, highly abundant, and highly efficient catalyst material for the OER. Transition metal sulfides are considered to be very promising electrocatalyst materials due to their good electronic conductivity and various oxidation states [3,4]. Metallic cobalt has been found to have a low energy barrier for the adsorption of OER intermediates, which makes the Co-based catalyst more efficient and promising for OER [5]. Compared with single metal sulfide, binary metal sulfides display enhanced electrocatalytic performance (In the previous chapter manganese cobalt sulfide shows better performance than cobalt sulfide and manganese sulfide). Based on the fact that binary metal sulfides have a synergistic effect which helps to improve catalytic activity, the combination of three transition metals is expected to provide further improvement in it.

As given in the literature survey in chapter one, along with the cobalt sulfide nickel sulfide is also widely studied material for OER and it also shows good electrochemical performance [6]. Also, the transition metals such as Co, Mn and Ni have approximately similar atomic radii. Therefore, the addition of nickel in manganese cobalt sulfide (obtained in the previous chapter) could further improve the catalytic activity. To enhance the charge and mass transport efficiency, the coupling of transition metal sulfides with three dimensional conductive nanocarbon supports such as reduced graphene oxide (rGO) is a most efficient strategy [7]. The composites of transition metal sulfides and rGO show high electric conductivity, high surface area

and good mechanical strength [8]. Therefore, it is highly desirable to deposit thin films of a composite of nickel manganese cobalt sulfide and rGO. SILAR method is one of the simple and low cost methods to deposit composite thin films on conductive substrates.

Therefore, in the present chapter nickel-manganese-cobalt sulfide/rGO composite thin films are deposited by SILAR method. Prior to the synthesis of composite thin films, it is important to optimize the composition of transition metal sulfide. For this, the present chapter is divided into two parts, part A and part B. Part A includes optimization of the composition of nickel-manganese-cobalt sulfide and its physicochemical and electrochemical characterizations. While the synthesis, physicochemical and electrochemical characterizations of nickel-manganese-cobalt sulfide/rGO composite thin film are given into part B. The origin of optimal performance of composite electrocatalyst was comprehensively scrutinized using detailed physio-chemical and electrochemical analyses. For this, the characterization techniques such as XRD, Raman, XPS, FESEM and HR-TEM are used. Electrochemical OER performance is tested in 1 M KOH electrolyte.

Part A: Optimization of nickel manganese cobalt sulfide thin film electrode

5A.1. Experimental details

5A.1.1. Chemicals

For the synthesis of nickel-manganese-cobalt sulfide thin film electrodes, chloride precursors of cobalt ($\text{CoCl}_2 \cdot 6\text{H}_2\text{O}$), manganese ($\text{MnCl}_2 \cdot 4\text{H}_2\text{O}$), nickel ($\text{NiCl}_2 \cdot 6\text{H}_2\text{O}$) and sulfur precursor (Na_2S) were purchased from Sigma Aldrich, USA and used as received. Stainless steel (SS) substrates of thickness 0.5 mm (purchased from a local supplier) were used for film deposition. Potassium hydroxide

(KOH, Sigma Aldrich, USA) was used to prepare an electrolyte. Double distilled water (DDW) was used throughout the experiment.

5A.1.2. Synthesis of nickel-manganese-cobalt sulfide

The synthesis procedure of nickel-manganese-cobalt sulfide (NMC Sulfide) was similar to the previous chapter (synthesis of manganese cobalt sulfide). For this, 0.1 M solution of Na_2S was used as an anionic precursor. Stoichiometric amounts of CoCl_2 , MnCl_2 and NiCl_2 were used to prepare 0.1 M cationic solution. Adsorption, reaction and rinsing time were kept 15, 15 and 10 s, respectively. At room temperature, 100 SILAR deposition cycles were repeated to get a uniform deposition of thin film. To optimize the metallic composition, the amount of Ni, Mn and Co was varied systematically to obtain the ratio of Ni:Mn:Co as 3:1:1, 1:3:1, 1:1:3 and 2:2:1 and samples were named as NMC-311, NMC-131, NMC-113 and NMC-221.

5A.2. Results and discussion

5A.2A. Physicochemical Characterizations

5A.2A.1. X-ray diffraction and energy dispersive X-ray spectroscopy

The crystalline nature of NMC sulfide thin film electrodes was evaluated by the X-ray diffraction (XRD) analysis and the results are shown in Figure 5.1(a). Similar to the manganese-cobalt sulfide thin film electrode (prepared in the previous chapter), the XRD patterns of NMC sulfide thin film electrodes also exhibited an absence of any diffraction peak. Nonetheless, only the diffraction peaks corresponding to SS substrate were found. The absence of any diffraction peaks clearly indicates that the synthesized thin films confine to the amorphous nature. The absence of any long-range atomic ordering typically results in such amorphous nature

and this could be beneficial for the electrochemical oxygen evolution reaction.

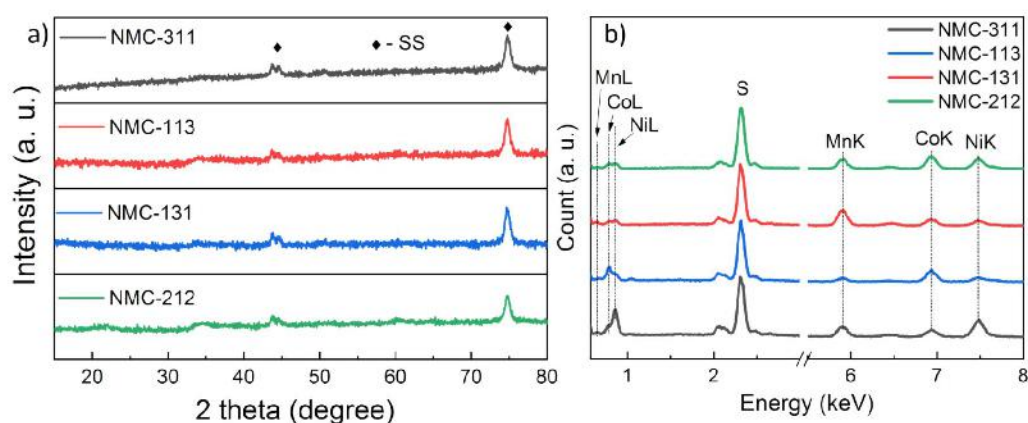


Figure 5.1: a) XRD patterns and b) EDX spectra of NMC sulfide thin film electrodes with different Ni:Mn:Co ratios.

To evaluate the atomic composition of NMC sulfide thin film electrodes, the energy dispersive X-ray spectroscopy (EDX) was employed. In Figure 5.1(b), the EDX spectra of NMC sulfide thin film electrodes exhibit the characteristic peaks of corresponding elements.

Table 5.1: Atomic percentage of NMC sulfide thin film electrodes with different Ni:Mn:Co ratios.

Element Sample Ni:Mn:Co ratio	Ni %	Mn %	Co %	S %
NMC-311 (3:1:1)	33.17	11.54	11.63	43.67
NMC-113 (1:1:3)	11.76	8.55	29.35	50.98
NMC-131 (1:3:1)	12.13	22	13.87	51.37
NMC-212 (2:1:2)	21.16	10.75	21.97	46.12

The peak intensities are also found to vary according to the atomic composition. The

atomic compositions determined through the EDX analysis are shown in Table 5.1. The ratio of atomic percentage of transition metals i.e. Ni, Mn and Co in thin film electrodes is approximately similar to the ratio of their precursors used to prepare cationic solution.

5A.2A.2. X-ray photoelectron spectroscopy

To determine the oxidation state of each element in NMC-212 electrocatalyst, X-ray photoelectron spectroscopy (XPS) was used. The survey spectrum (Figure 5.2(a)) revealed the presence of Ni, Mn, Co and S species in the material, consistent with EDX results. Figure 5.2(b) shows the high resolution XPS spectrum of Co 2p. The peaks at ~781.3 and ~797.1 eV binding energy match with 2p_{3/2} and 2p_{1/2} levels of Co [9,10]. The deconvoluted binding energy components of both the levels at ~780.8 and ~795.1 eV are attributed to -3 valence state while ~782.5 and ~798.1 eV are attributed to +2 valence state [11]. High resolution Mn 2p spectrum shown in Figure 5.2(c) also displays a pair of doublets matching with 2p_{3/2} and 2p_{1/2} levels of Mn at binding energies of ~643.1 and ~653.8 eV, respectively [12]. The deconvoluted peaks situated at ~641.9 and ~654.7 eV are assigned to Mn³⁺ 2p_{3/2} and Mn³⁺ 2p_{1/2} configurations, respectively. While peaks at ~644.7 and ~654.7 eV are assigned to Mn⁴⁺ 2p_{3/2} and Mn⁴⁺ 2p_{1/2} configurations, respectively [13–15]. The high-resolution Ni 2p XPS spectrum in Figure 5.2(d) possesses two spin-orbit doublets at ~855.9 and ~873.7 eV accompanied by two shakeup satellite peaks. The peaks due to spin-orbit doublet can be ascribed to Ni 2p_{3/2} and Ni 2p_{1/2} levels, respectively [16,17]. Deconvolution of both the peaks reveals two types of energy bands from which peaks at ~854.1 and ~871.8 eV correspond to +2 oxidation state while peaks at ~856.1 and ~873.8 eV correspond to +3 oxidation state of Ni [18,19].

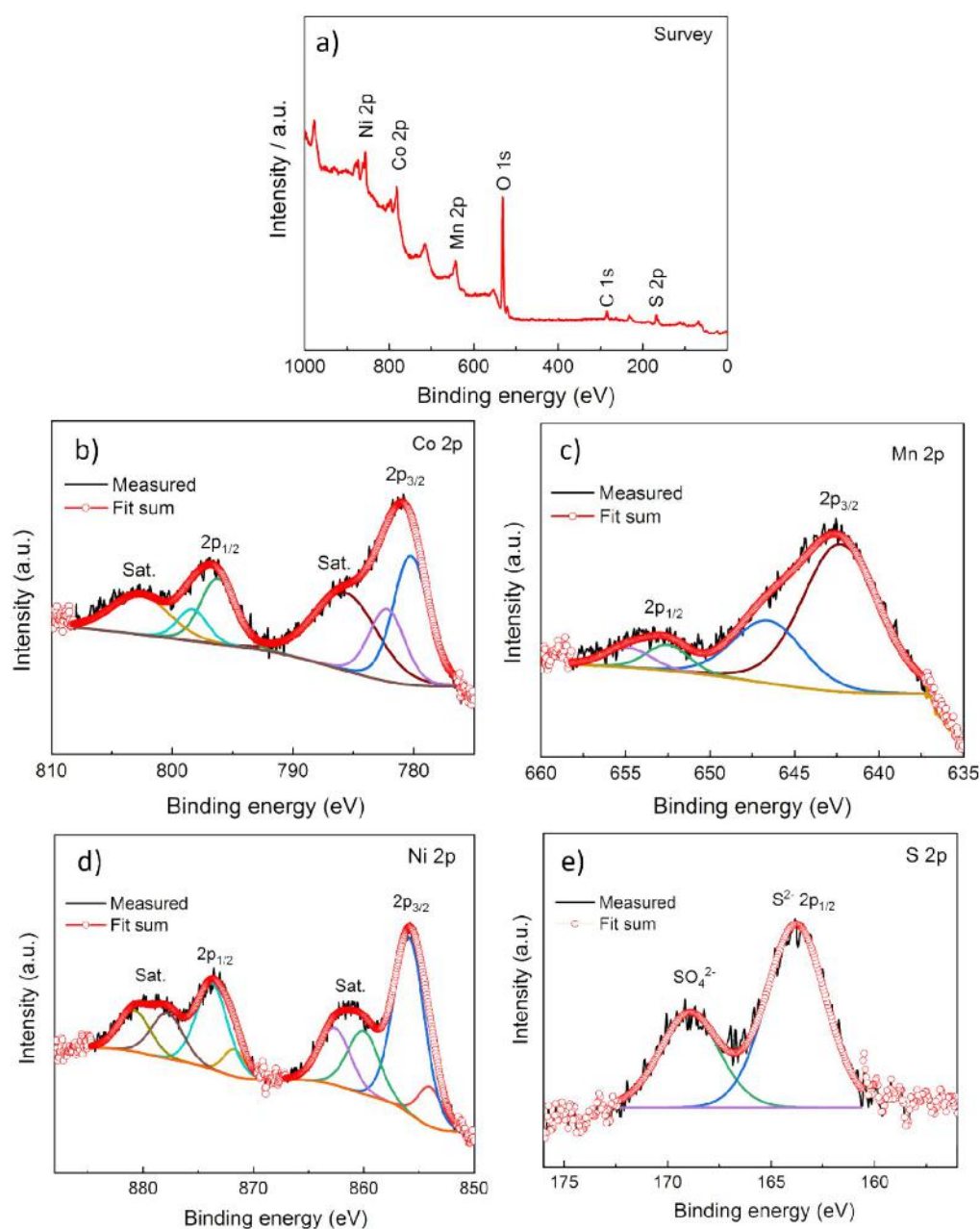


Figure 5.2: a) XPS survey spectrum of NMC-212. High resolution spectra of b) Co 2p, c) Mn 2p, d) Ni 2p and e) S 2p.

High-resolution spectrum of S 2p (Figure 5.2(e)) displays two features at ~162.9 and ~168.0 eV matching with S²⁻ 2p and SO₄²⁻, respectively [10]. Therefore, it is confirmed that the multivalence states of Co, Mn and Ni are coexisting in NMC-212, which could be helpful for the enhancement of its electrochemical activity for OER.

5A.2A.3. Field emission scanning electron microscopy

The field emission scanning electron microscope (FESEM) images of NMC sulfide thin film electrodes prepared with different Ni:Mn:Co ratios are shown in Figure 5.3 at three different magnifications (25, 50 and 70kX). In the samples NMC-311 (Figure 5.3(a-c)) and NMC-212 (Figure 5.3(j-l)), sheet-like morphology is observed.

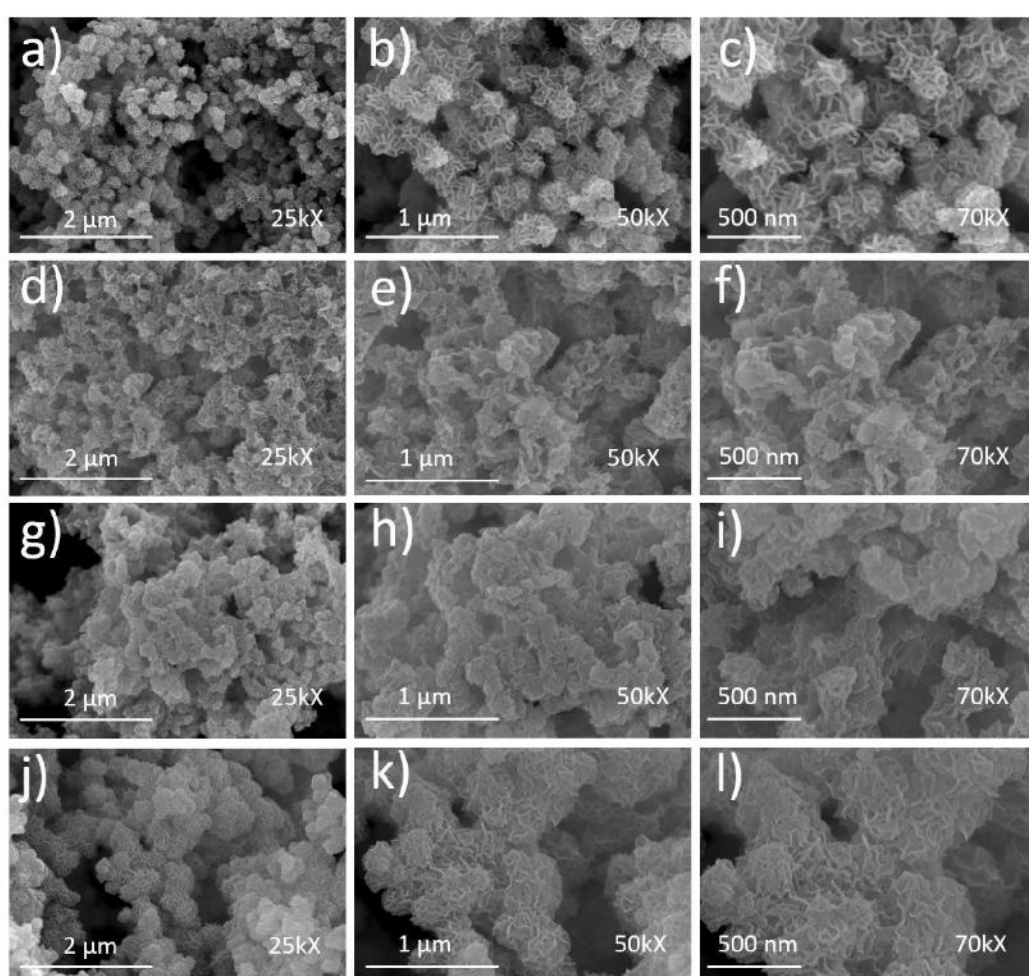


Figure 5.3: FESEM images of NMC sulfide thin film electrodes with different Ni:Mn:Co ratios, a-c) NMC-311, d-f) NMC-113, g-i) NMC-131 and j-l) NMC-212 at different magnifications of 25kX, 50kX and 70kX.

The sheets are unevenly connected with non-uniform spacing, eventually resulting in

the formation of a hierarchical porous interconnected network. But for samples NMC-113 (Figure 5.3(d-f)) and NMC-131 (Figure 5.3(g-i)) compact and dense microstructure is formed. The interconnected sheets like nanostructures for electrochemical applications have gained much interest due to their advantageous porosity and high surface area [20]. The presence of different elements and their distribution in NMC-212 sulfide thin film electrode is further confirmed by elemental mapping through the EDX technique. As seen in Figure 5.4, S, Co, Mn and Ni elements are found to be uniformly distributed.

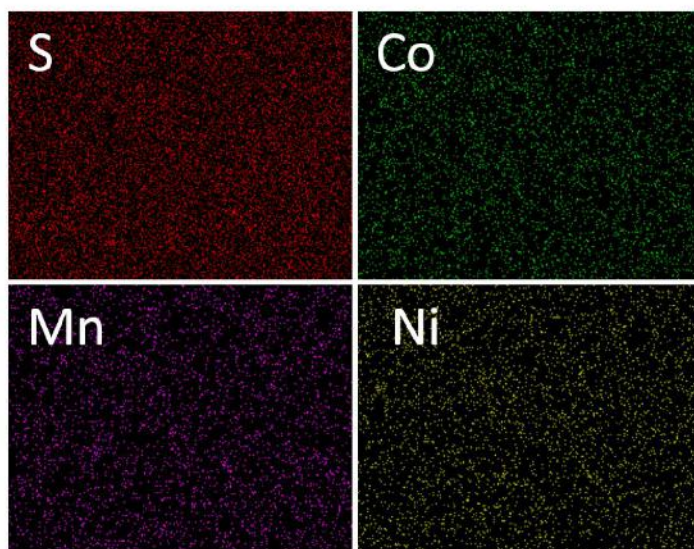


Figure 5.4: EDX elemental mapping of NMC-212 thin film electrode.

5A.2A.4. Transmission electron microscopy

Figure 5.5(a) shows the transmission electron microscopy (TEM) image of NMC-212 sample. The TEM image clearly shows the continuously interconnected sheets which form a web-like microstructure. Such a unique architecture promotes the intermediate reaction of OER by furnishing maximum surface area. The selective area electron diffraction (SAED) pattern image is shown in Figure 5.5(b). In the reverse space of the lattice planes, weak and diffused rings are observed. Hence it is

confirmed that NMC-212 is amorphous, which is consistent with XRD results.

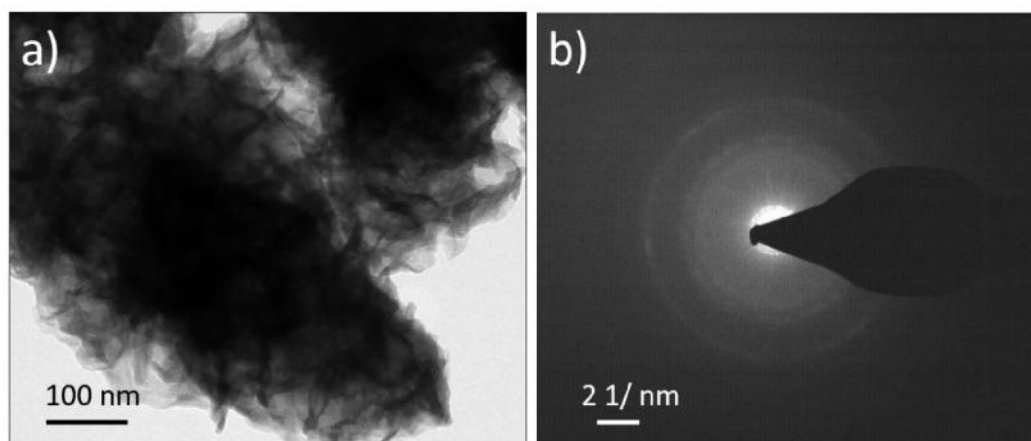


Figure 5.5: a) TEM image and b) SAED pattern of NMC-212 thin film electrode.

5A.2B. Electrochemical characterizations

5A.2B.1. Linear sweep voltammetry and Tafel slope

The electrocatalytic activity of nickel manganese cobalt (NMC) sulfide towards OER is evaluated in 1 M KOH electrolyte. The linear sweep voltammetry (LSV) is performed with a scan rate of 2 mV s^{-1} . Figure 5.6(a) shows the obtained LSV curves without iR-correction. As observed in the Figure, NMC-212 exhibits the best catalytic performance among all NMC sulfides with different Ni:Mn:Co ratios. To achieve the current density of 10 mA cm^{-2} , NMC-212 requires 235 mV overpotential, which is lower than NMC-311 (245 mV), NMC-113 (254 mV) and NMC-131 (261 mV) samples. Since the electrocatalytic reaction current is directly proportional to the oxygen yield, the higher current density of NMC-212 ($>200 \text{ mA cm}^{-2}$) indicates its prominent oxygen evolution behavior. The overpotentials required by NMC thin film electrocatalysts to reach different current densities (10, 50 and 100 mA cm^{-2}) are represented in the form of a bar diagram in Figure 5.6(b). NMC-212 electrocatalyst requires 235, 280 and 311 mV overpotential to reach 10, 50 and 100

mA cm^{-2} current density, respectively. The trend in OER reactivity for NMC sulfides with different Ni:Mn:Co ratios is in the order $\text{NMC-212} > \text{NMC-311} > \text{NMC-113} > \text{NMC-131}$. This indicates the metallic composition in NMC-212 electrocatalyst is optimal.

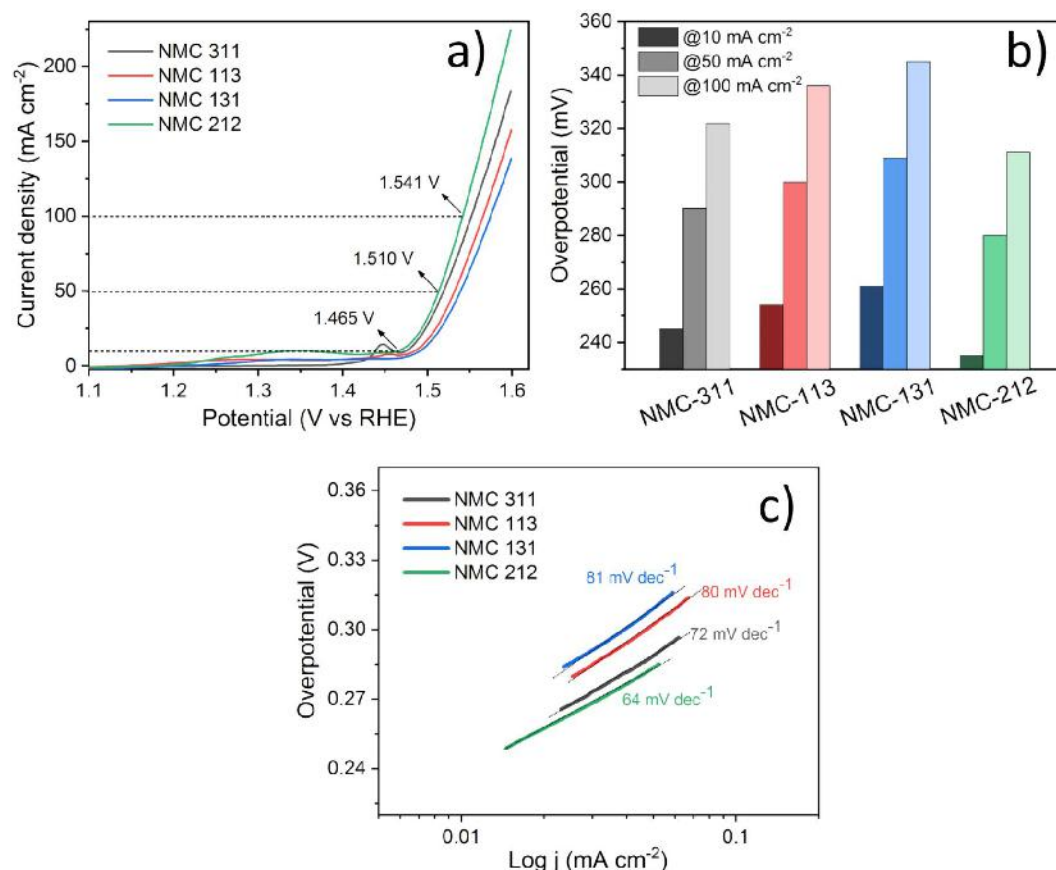


Figure 5.6: Electrochemical OER performance of NMC sulfide thin film electrocatalysts with different Ni:Mn:Co ratios, a) LSV curves, b) overpotential required to achieve 10, 50 and 100 mA cm^{-2} current density and c) Tafel slope.

The OER kinetics parameter of the above NMC electrocatalysts was investigated by Tafel plots. Tafel plots for electrocatalysts extracted from the corresponding LSV curves are shown in Figure 5.6(c). The Tafel slopes for NMC-311, NMC-113, NMC-131 and NMC-212 electrocatalysts are 72, 80, 81 and 64 mV dec^{-1} , respectively which indicate fast OER kinetics of NMC-212 electrocatalyst than others.

5A.2B.2. Electrochemical impedance spectroscopy

Electrochemical impedance spectroscopy (EIS) measurements were carried out under OER reaction conditions for insightful analysis. Figure 5.7 shows electrochemical impedance spectra of NMC sulfide electrocatalysts. The intercepts of impedance spectra to the real Z-axis in high frequency region are associated with solution resistance (R_s). As freshly prepared 1 M KOH electrolyte was used for the measurement of each electrocatalyst, the value of R_s for all electrocatalysts is similar and it is 0.58 Ω . While the intercept of impedance spectrum to real Z-axis in low frequency region is associated with charge transfer resistance (R_{ct}).

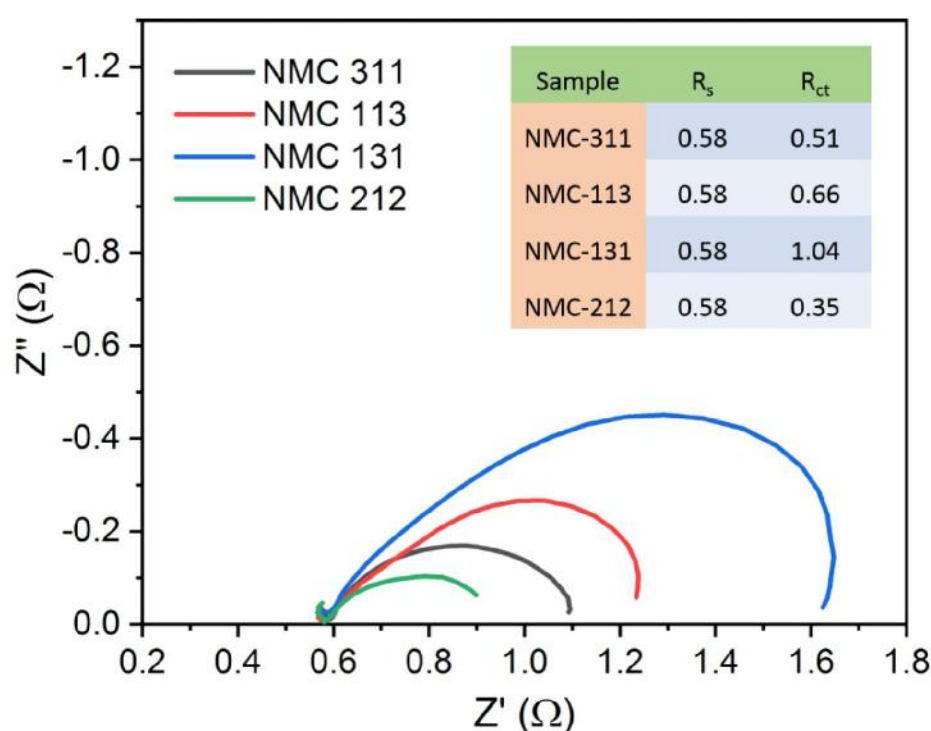


Figure 5.7: Electrochemical impedance spectra of NMC sulfide thin film electrocatalysts with different Ni:Mn:Co ratios. Inset shows obtained values of R_s and R_{ct} represented in tabular form.

From the impedance spectra, the R_{ct} of NMC sulfide electrocatalysts varies with

composition. NMC-212 possesses the lowest R_{ct} of $0.35\ \Omega$ while NMC-131 possesses the highest R_{ct} of $1.04\ \Omega$. This indicates fast charge transfer in NMC-212 electrocatalyst. The order of R_{ct} value for different compositions of NMC sulfide is $\text{NMC-212} < \text{NMC-311} < \text{NMC-113} < \text{NMC-131}$, which correlates well with the OER activity of each electrocatalyst.

Part B: Synthesis, characterization and electrocatalytic OER performance of nickel-manganese-cobalt sulfide/rGO composite thin film electrode

5B.1. Experimental details

5B.1.1. Chemicals

For the synthesis of nickel-manganese-cobalt sulfide/rGO composite thin film electrodes, chloride precursors of cobalt ($\text{CoCl}_2 \cdot 6\text{H}_2\text{O}$), manganese ($\text{MnCl}_2 \cdot 4\text{H}_2\text{O}$), nickel ($\text{NiCl}_2 \cdot 6\text{H}_2\text{O}$) and sulfide precursor (Na_2S) were purchased from Sigma Aldrich, USA and used as received. The aqueous dispersion of single-layer graphene oxide (GO) was purchased from Hangzhou Gaoxin Technology Co., Ltd., China. Stainless steel (SS) substrates of thickness 0.5 mm (SUS-304, Nilaco Corporation, Japan) were used for film deposition. Potassium hydroxide (KOH, Sigma Aldrich, USA) was used to prepare aqueous electrolyte. Entire experiments were conducted with double distilled water (DDW).

5B.1.2. Thermal reduction of graphene oxide

On the graphene oxide (GO) sheets large number of oxygen containing groups exist (eg. $-\text{OH}$, $-\text{OOH}$, $-\text{COOH}$), which makes it insulating and significantly restricts its applications in various fields [21]. Different properties of GO such as electrical and thermal conductivity, specific surface area and stability can be enhanced

by reducing the number of oxygen containing functional groups, hence obtaining reduced graphene oxide (rGO) [22]. Among various methods used for the reduction of graphene oxide (GO) into a purer form of graphene, the thermal reduction method is simpler, safer, and economic. A thermal reduction of GO causes significant weight loss and volume expansion of the material. Reduction temperature plays the most crucial role as it controls the quality of reduced graphene oxide (rGO). Sengupta et. al. [23] have studied the effect of temperature on the purity of rGO and achieved high-quality rGO at an optimum temperature of 350 °C. Referring to this report, the GO in the present study was heated at 350 °C in the Argon atmosphere for 3h to obtain rGO.

5B.1.2. Synthesis of nickel-manganese-cobalt sulfide/rGO composite (NMC/rGO)

The NMC/rGO composite was synthesized by SILAR method in which the optimized experimental conditions and chemical composition of NMC sulfide from part A was carry forwarded from the previous part. To prepare the rGO solution, 4 mg of rGO powder was dispersed in 50 ml DDW and sonicated for 30 min for uniform dispersion. The stainless steel substrate after completing one NMC sulfide cycle (as given in part A) was further dipped into the rGO solution. This total procedure was repeated for 100 cycles to get uniform deposition. The rGO loading was changed by varying the rGO immersion after 1, 20 and 40 NMC sulfide cycles and the samples were named NMC/rGO-1, NMC/rGO-20 and NMC/rGO-40, respectively.

5B.2. Results and discussion

5B.2A. Physicochemical Characterizations

5B.2A.1. X-ray diffraction

The crystalline structure of GO and rGO powder samples and NMC/rGO

composite thin film electrodes was studied by XRD and the obtained XRD patterns were shown in Figures 5.8 and 5.9, respectively. The diffraction peak present at $2\theta = 12.5^\circ$ in the XRD pattern of GO disappeared after the thermal treatment, as observed in the XRD pattern of rGO. A new peak at $2\theta = 24.1^\circ$ has emerged after thermal treatment indicating the successful reduction of GO using experimental conditions in the present study [24].

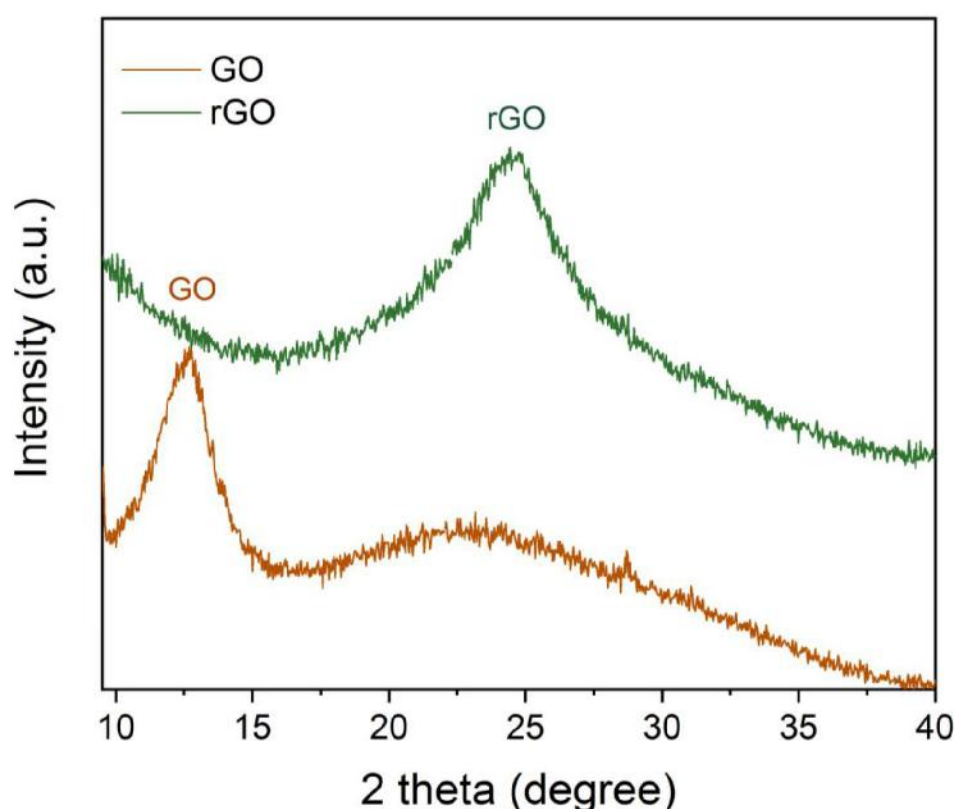


Figure 5.8: XRD patterns of GO and rGO.

The XRD patterns of NMC/rGO composite thin film electrodes prepared with the different number of rGO cycles are shown in Figure 5.9. The diffraction peak around 45° in all three samples arises due to the SS substrate (denoted by *). As seen in part A of the present chapter, NMC sulfide has amorphous nature, which is maintained in composite thin film electrodes also. As for NMC/rGO-1 composite, the

substrate was immersed in rGO solution after each NMC sulfide cycle, the rGO loading in the composite is higher than NMC/rGO-20 and NMC/rGO-40 where the substrate was immersed in rGO solution after 20 and 40 NMC sulfide cycles, respectively. Due to this, the diffraction peak from rGO is more intense in NMC/rGO-1 while it is not observable in NMC/rGO-40 electrocatalyst.

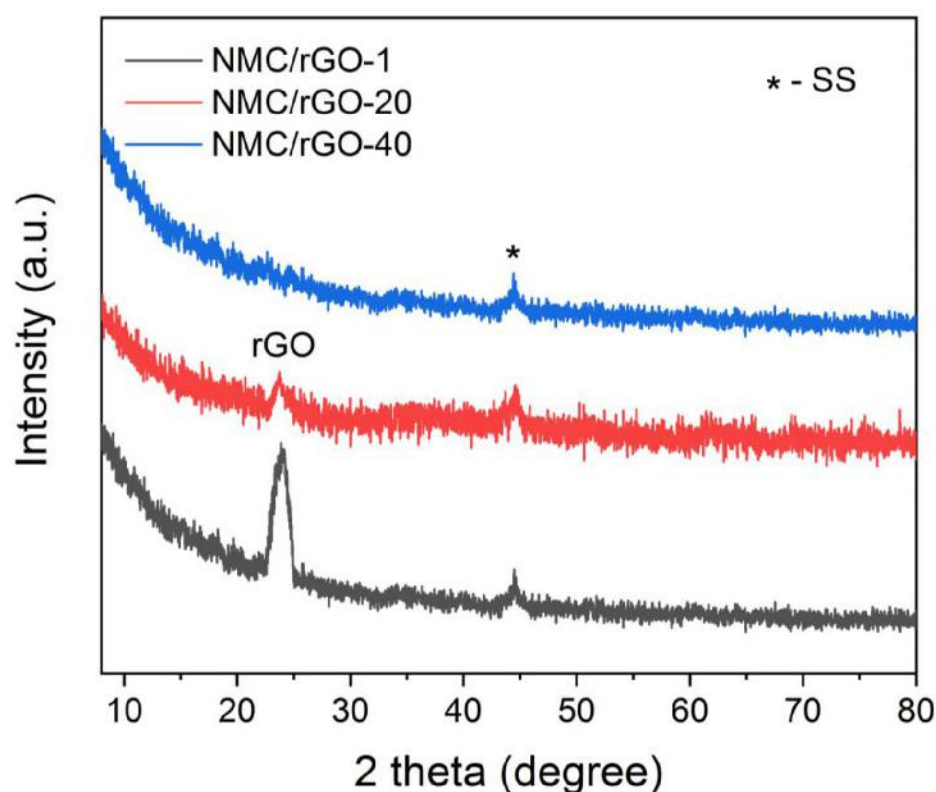


Figure 5.9: XRD patterns of NMC/rGO composite thin film electrodes with different rGO cycles.

The atomic compositions determined through the EDX analysis are shown in Table 5.2. As seen in the table, the Ni:Mn:Co ratio for all samples is maintained $\sim 2:1:2$ (as used to prepare cationic solution). The atomic percentage of carbon is maximum (56.3%) in sample NMC/rGO-1 while minimum (1.89%) in sample NMC/rGO-40. This supports XRD results.

Table 5.2: Atomic percentage of NMC/rGO thin film electrodes with different rGO cycles.

Elements Sample	Ni (%)	Mn (%)	Co (%)	S (%)	C (%)
NMC/rGO-1	9.26	4.11	9.2	21.13	56.3
NMC/rGO-20	20.21	9.06	19.16	41.08	10.49
NMC/rGO-40	21.16	10.75	20.97	45.23	1.89

5B.2A.2. Raman spectroscopy

Raman spectroscopy offers further insights into the structural changes in GO due to thermal treatment. Figure 5.10 shows the Raman spectra of GO and rGO samples. Both the spectra exhibit G and D bands. The G bands at $\sim 1590\text{ cm}^{-1}$ are characteristic of sp^2 hybridized carbon-carbon bonds in graphene while the D bands at $\sim 1350\text{ cm}^{-1}$ are characteristic of lattice distortions and sp^3 -like defects caused by the oxidation process [25]. The ratio of the intensity of these two bands (I_D/I_G) for each spectrum is included in the Figure. The GO sample shows a prominent D peak with I_D/I_G of 1.08 indicating significant structural disorder created due to the presence of oxygen functional groups. After the thermal treatment i.e. for rGO sample, the ration of I_D and I_G (I_D/I_G) slightly decreased than GO and become 0.92. This indicates that the graphitic sp^2 network of carbon has restored due to the removal of functional groups. The Raman results once again prove the successful reduction of graphene oxide.

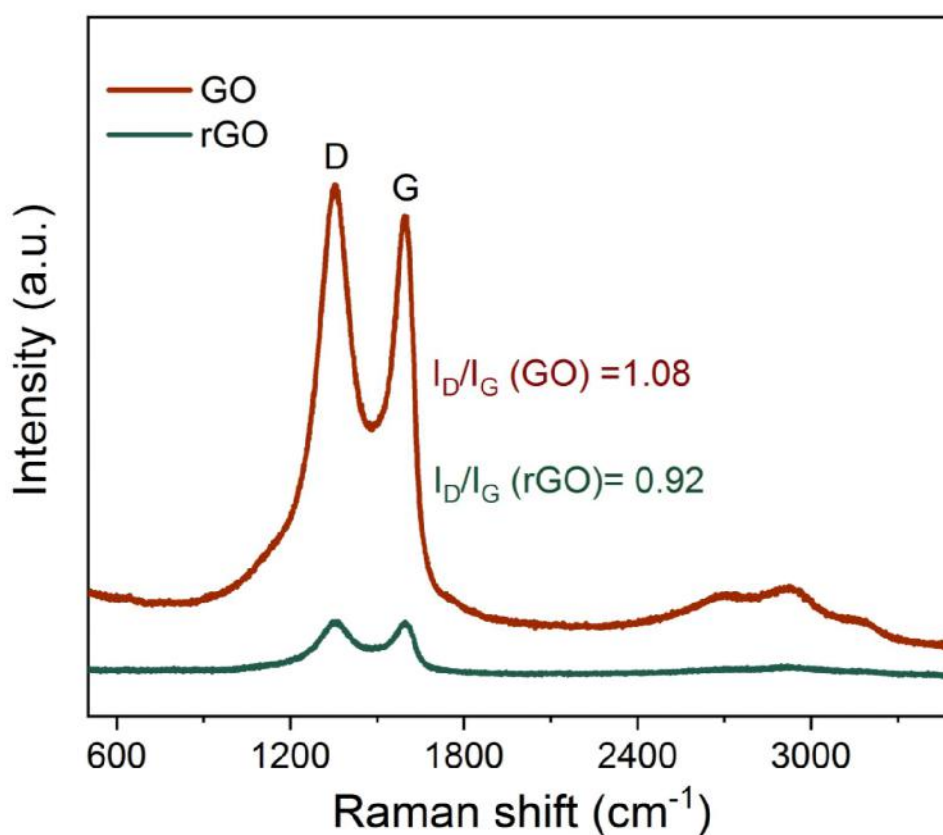


Figure 5.10: Raman spectra of GO and rGO.

5B.2A.3. X-ray photoelectron spectroscopy

The GO and rGO powders were characterized through X-ray photoelectron spectroscopy. Figure 5.11 (a) and (b) show the survey spectra of GO and rGO samples, respectively. It is observed that the intensity of O 1s peak is significantly decreased while the intensity of C 1s is increased after the thermal treatment as compared to the intensities of those peaks in GO sample. The percentage of reduction of GO after thermal treatment can be easily calculated using the peak area of O 1s peak before and after thermal treatment using the formula,

$$\text{Percentage of reduction} = \frac{\text{Peak area of O 1s before thermal treatment (rGO)}}{\text{Peak area of O 1s after thermal treatment (GO)}} \times 100 \quad (5.1)$$

In the present study, the GO is reduced by $\sim 45\%$. The high-resolution XPS

spectra of C 1s and O 1s were deconvoluted in order to study the oxygen speciation in the GO and rGO samples.

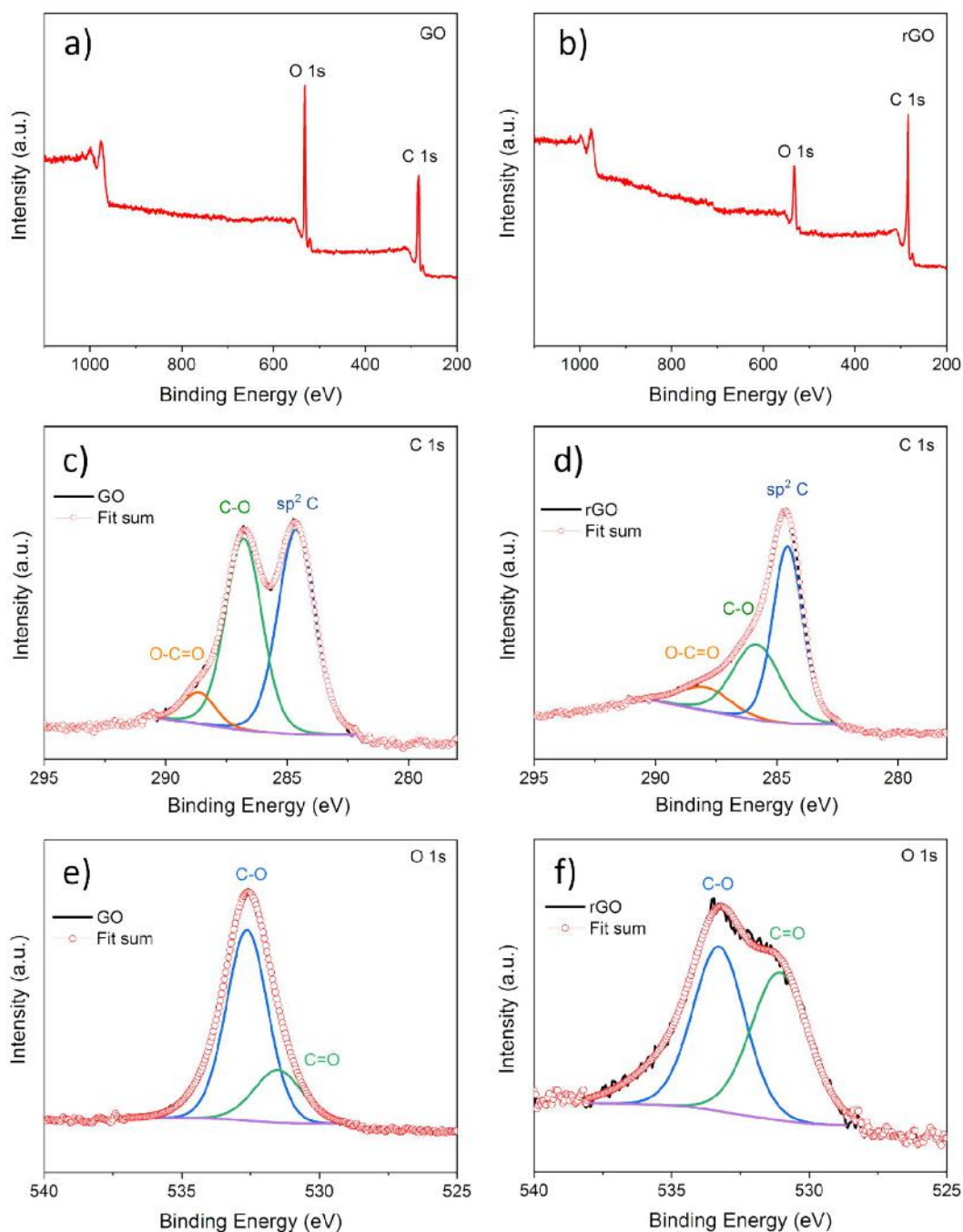


Figure 5.11: The XPS survey spectra of a) GO and b) rGO. XPS high-resolution spectra of C1s of c) GO, d) rGO and O1s of e) GO and f) rGO.

Figure 5.11 (c) and (d) show C 1s core-level spectra of GO and rGO, respectively. In

both the spectra, the peak at binding energy 284.6 eV is attributed to sp^2 hybridized carbon. While the peaks at 286.7 and 288.7 eV are attributed to hydroxyl and carboxyl functional groups, respectively [26]. When comparing both the spectra (GO and rGO), the intensity of peaks associated with oxygen-containing functional groups (hydroxyl and carboxyl) are sustainably decreased while the intensity of sp^2 hybridized carbon is increased. Similarly, in the O 1s core-level spectrum, two peaks are identified for both GO and rGO samples (Figure 5.11 (e) and (f)). The peaks at 531.6 and 532.7 eV binding energies are credited to double and single bonded oxygen to the carbon, respectively [27]. The decrease in the intensity of the peak at 532.7 eV in rGO sample compared with GO revealed that under the experimental conditions the single-bonded oxygen to carbon is preferentially removed.

5B.2A.4. Field emission scanning electron microscopy

The microstructure of GO and rGO powders and NMC/rGO composite thin film electrodes were analyzed by FESEM. Figure 5.12 shows FESEM images of GO and rGO powder samples.

Figures 5.12 (a) and (b) show FESEM images at lower magnification (30X) of GO and rGO, respectively. In the GO sample, carbon layers are stacked and become a single flake of size ~ 1.7 μm , while the broken flakes with smaller size are observed in rGO sample. As observed at higher (30kX) magnification, the carbon layers are stacked in GO sample (Figure 5.12 (b)), which are significantly exfoliated in rGO sample (due to the heat treatment) (Figure 5.12 (d)). Hence, rapid volumetric expansion may have taken place which results in the broadening of the gap between carbon layers. Due to this separation of carbon layers, there may be an increment in the specific surface area of rGO compare with GO.

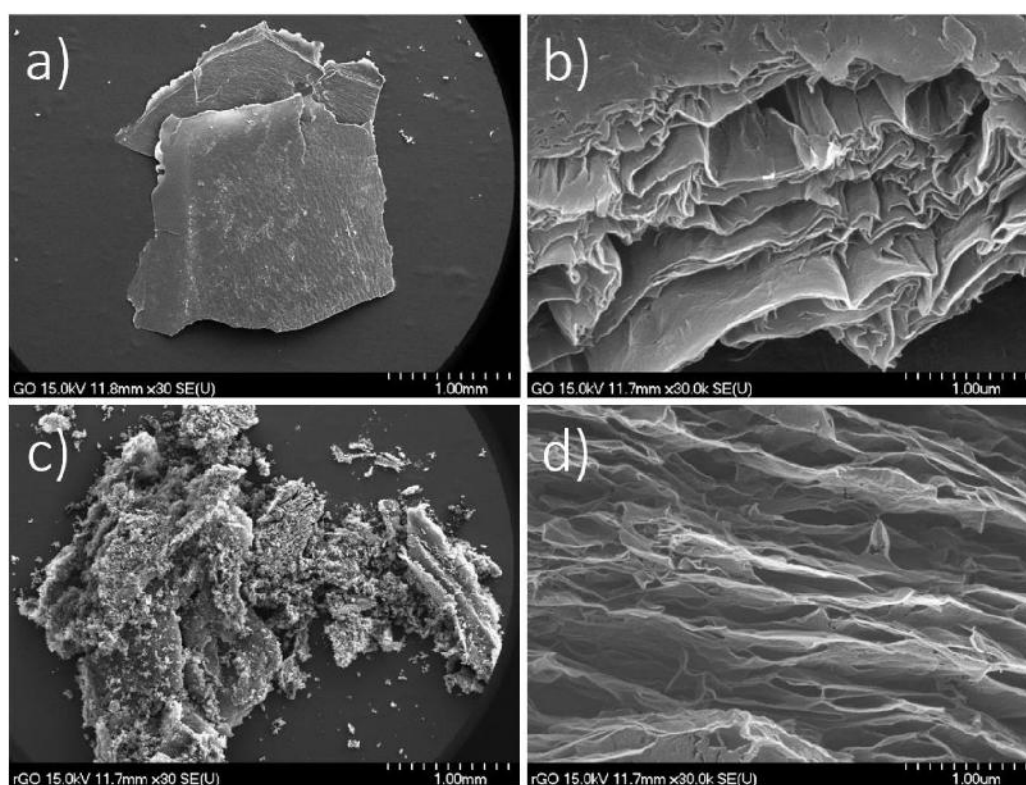


Figure 5.12: FESEM images of GO (a) at 30X and (b) at 30kX magnifications and rGO (c) at 30X and (d) at 30kX magnifications.

The FESEM images of NMC/rGO composite thin film electrodes are shown in Figure 5.13. In the present study, the quantity of rGO is controlled by varying the number of SILAR cycles of rGO. For sample NMC/rGO-1, the substrate was dipped into rGO solution after each NMC sulfide cycle. Similarly, for sample NMC/rGO-20 and NMC/rGO-40, the substrate was dipped after every 20 and 40 cycles of NMC sulfide respectively.

Due to the large quantity of rGO and also the lack of continuous cycles of NMC sulfide, a compact microstructure is formed in NMC/rGO-1 (Figure 5.13 (a, b)). For sample NMC/rGO-40 the substrate was dipped in rGO solution only two times, therefore possibly the negligible quantity of rGO is composited with NMC sulfide. Due to this, in Figure 5.13 (e, f) NMC/rGO-40 exhibited similar morphology that of

NMC sulfide (Figure 5.3 (j-l) in part A). While for sample NMC/rGO-20, where the substrate was dipped in rGO solution after 20 NMC sulfide cycles, the sheet-like structure of NMC sulfide is maintained upto some extent, as seen in Figure 5.13 (c, d). The synergy of the optimum amount of rGO sheets and sufficiently grown sheet-like structure of NMC sulfide on it results into the porous structure of the composite thin film.

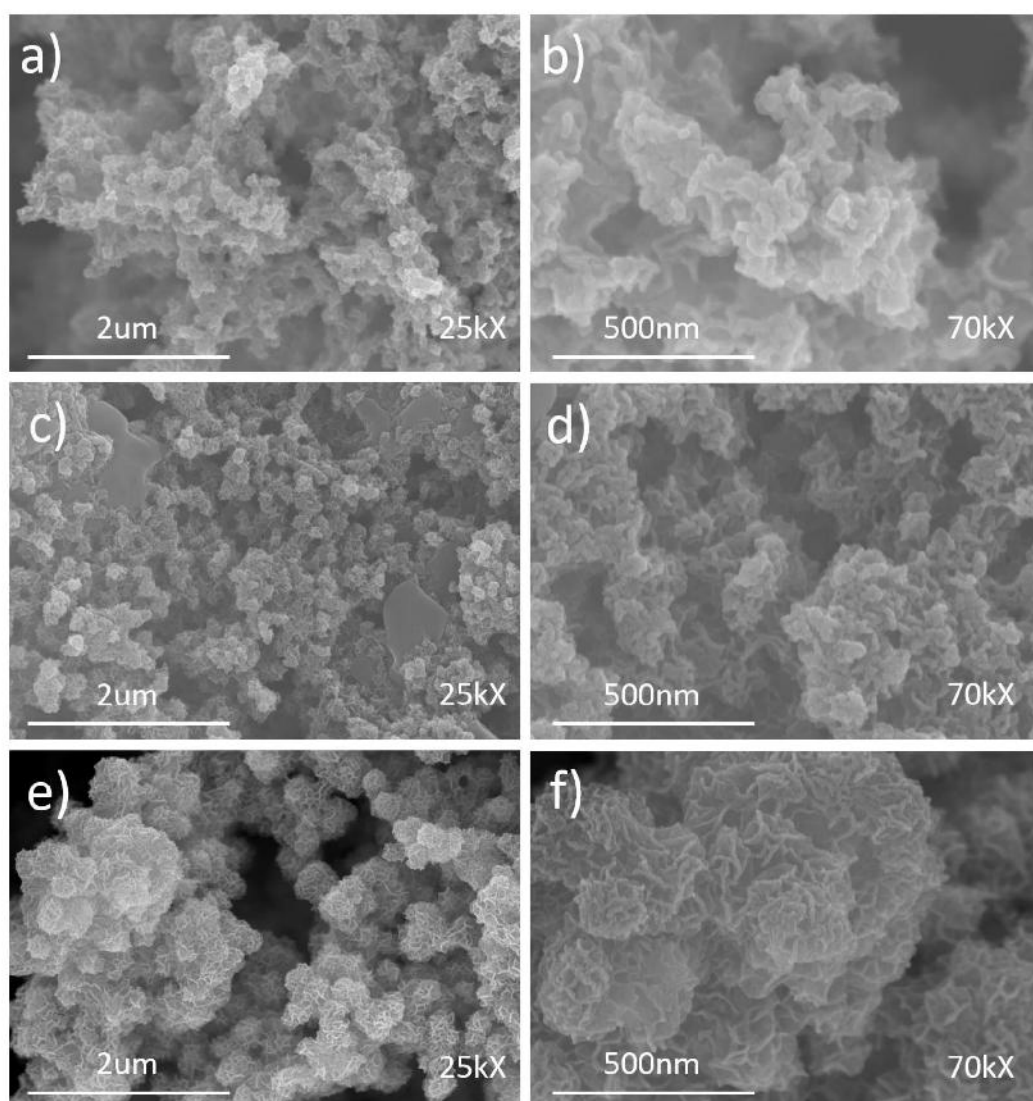


Figure 5.13: FESEM images of (a and b) NMC/rGO-1, (c and d) NMC/rGO-20 and (e and f) NMC/rGO-40 with 25kX and 70kX magnifications.

5B.2B. Electrochemical characterizations5B.2B.1. Linear sweep voltammetry and Tafel slope

To evaluate the OER performance of NMC/rGO composite thin film electrocatalysts, a conventional three-electrode system is used. Saturated calomel electrode (SCE) and platinum wire were used as reference and counter electrodes, respectively. The NMC/rGO composite thin film electrocatalysts deposited on SS substrates were used as a working electrode. All the electrochemical study was carried out in 1 M KOH electrolyte. Linear sweep voltammetry (LSV) was performed with a scan rate of 2 mV s^{-1} . The obtained polarization curves without iR correction are shown in Figure 5.14 (a). Among the three electrocatalysts, NMC/rGO-20 shows a low overpotential of 230 mV while the samples NMC/rGO-1 and NMC/rGO-40 show 235 and 255 mV, respectively to reach 10 mA cm^{-2} current density. Hence the quantity of rGO in composite plays an important role in electrochemical performance. When compared with NMC sulfide electrocatalyst optimized in part A of the present chapter, the NMC/rGO-20 composite electrocatalyst shows only 5 mV decrement in overpotential at 10 mA cm^{-2} current density but at the higher current density of 100 mA cm^{-2} this decrement is 20 mV. NMC/rGO-20 composite electrocatalyst requires 230, 268 and 291 mV overpotential to reach 10, 50 and 100 mA cm^{-2} current density, respectively. This difference in OER activity of these two electrocatalysts highlights the beneficial role of rGO for excellent electrocatalytic activity. The OER reaction kinetics of NMC/rGO composite electrocatalysts with different quantities of rGO was investigated by Tafel plots. Tafel plots were extracted from the corresponding LSV curves as shown in Figure 5.14 (b). The Tafel slopes for NMC/rGO-1, NMC/rGO-20 and NMC/rGO-40 composite electrocatalysts were found to be 90, 50 and 67 mV dec^{-1} , respectively. This indicates fast OER kinetics of NMC/rGO-20 electrocatalyst than

others.

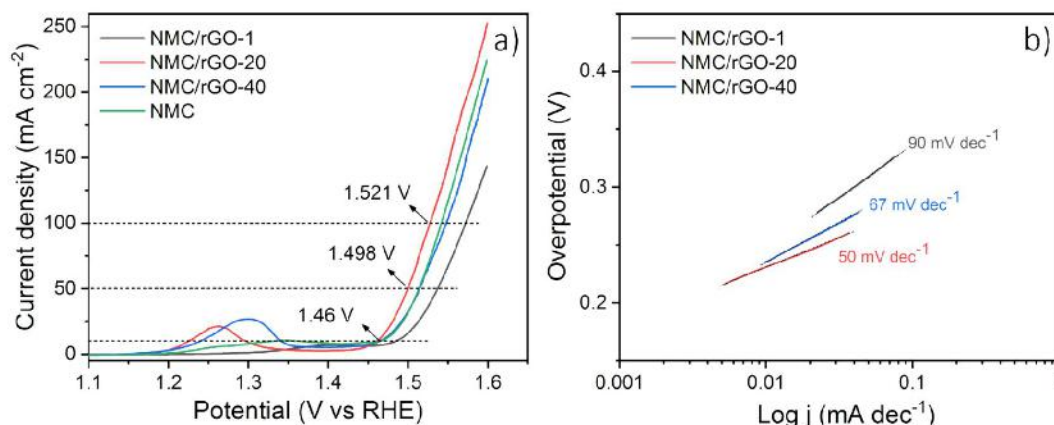


Figure 5.14: Electrochemical OER performance of NMC/rGO composite thin film electrocatalysts with different rGO cycles, a) LSV curves and b) Tafel slope.

5B.2B.2. Electrochemical active surface area

To give insight into the OER activity of NMC/rGO composite electrocatalysts with different rGO loading, electrochemical active surface area (ECSA) was calculated from double-layer capacitance (C_{dl}). For that cyclic voltammetry (CV) curves for each electrocatalyst were measured in the non-faradic potential region (+0.2 to +0.35 V vs. SCE) at scan rates from 1 to 5 mV s⁻¹ as shown in Figure 5.15 (a-c). The current density at a fixed potential of +0.275 V vs. SCE was measured for each scan rate. Figure 5.15 (d) shows the scan rate vs. current density curves for NMC/rGO composite electrocatalysts. The slope of these linear curves indicates the corresponding C_{dl} value.

The values of ECSA for each electrocatalyst were calculated by dividing the C_{dl} value by 0.04 mF cm⁻² as explained in previous chapters. The ECSA values of NMC/rGO composite electrocatalysts are obtained as 107.5, 350.0 and 220.0 cm² for NMC/rGO-1, NMC/rGO-20 and NMC/rGO-40, respectively. Hence, NMC/rGO-20 exhibits higher ECSA than other composite electrocatalysts which is directly related to their

different microstructures observed in FESEM images.

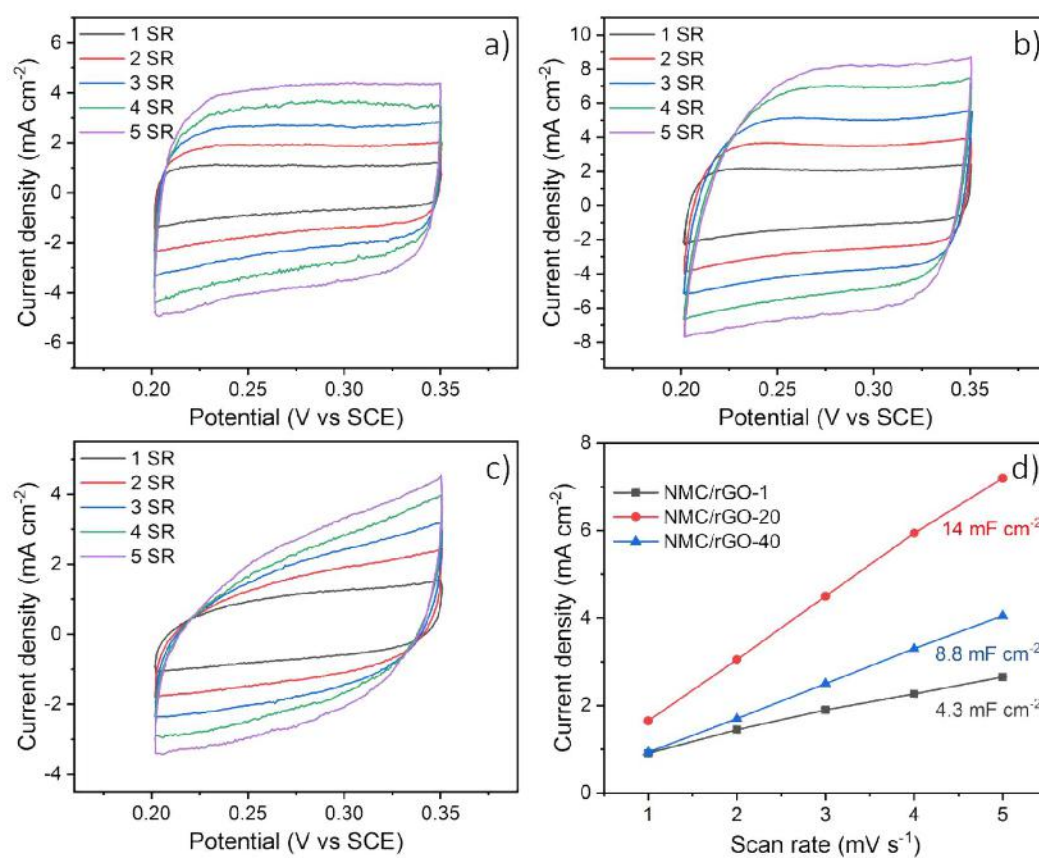


Figure 5.15: Cyclic voltammetry curves in non-faradic region for a) NMC/rGO-1, b) NMC/rGO-20 and c) NMC/rGO-40. d) Corresponding current density vs. scan rate plots for all electrocatalysts.

5B.2B.3. Electrochemical impedance spectroscopy and stability

Figure 5.16 (a) shows Nyquist plots of NMC/rGO composite electrocatalysts. The intercepts of impedance spectrum to the real Z-axis in high-frequency region are associated with solution resistance (R_s) and its value (0.5Ω) is almost similar for all the composite electrocatalysts.

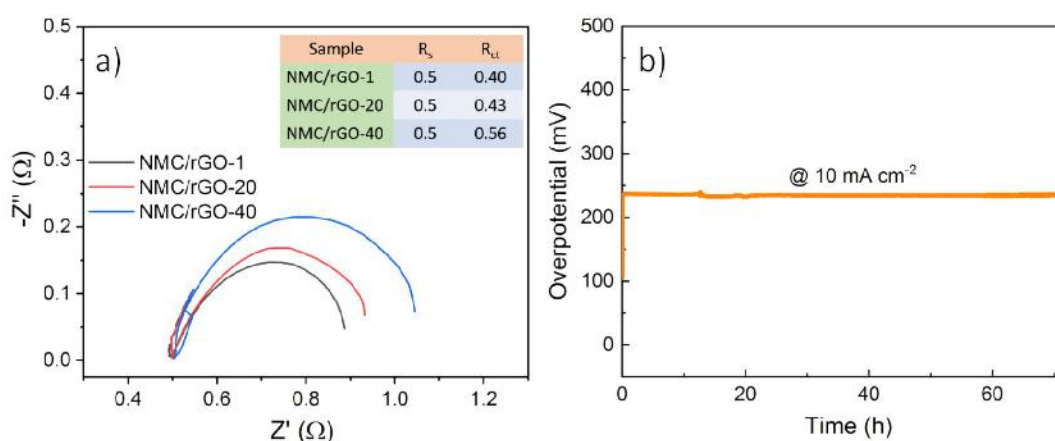


Figure 5.16: a) Nyquist plots obtained from electrochemical impedance spectroscopy of NMC/rGO composite electrocatalysts (Inset shows corresponding values of R_s and R_{ct}) and b) Long term durability of NMC/rGO-20 thin film electrocatalyst at 10 mA cm^{-2} constant current density.

The charge transfer resistance (R_{ct}) values for NMC/rGO-1, NMC/rGO-20 and NMC/rGO-40 were found 0.40, 0.43 and 0.56 Ω , respectively. The lowest value of R_{ct} of NMC/rGO-1 electrocatalysts may be due to the maximum loading of the rGO and as well as high electrical conductivity of rGO. As the NMC/rGO-40 electrocatalyst contains negligible rGO its R_{ct} value is high. While NMC/rGO-20 electrocatalyst shows moderate R_{ct} value.

The electrochemical stability of NMC/rGO-20 composite electrocatalyst towards OER is measured by chronopotentiometry mode at a constant current density of 10 mA cm^{-2} for 72 h (Figure 5.16 (b)). NMC/rGO-20 electrocatalyst shows the constant overpotential over 72 h demonstrating good stability. To get further insight into the physical changes, NMC/rGO-20 electrocatalyst is characterized by XRD after the 72 h constant OER. Figure 5.17 (a) shows LSV curves of NMC/rGO-20 electrocatalyst before and after stability indicating good stability towards OER.

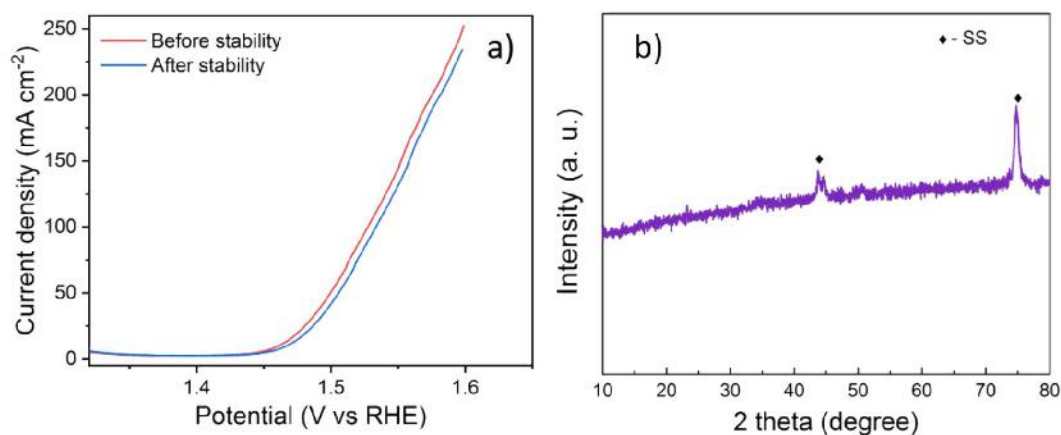


Figure 5.17: a) LSV curves before and after stability study and b) XRD spectrum of NMC/rGO-20 thin film electrocatalyst after stability test.

As observed in figure 5.17 (b), no additional diffraction peaks are raised; hence, NMC/rGO-20 electrocatalyst maintains its amorphous phase after long-term OER. This shows the nickel-manganese-cobalt sulfide/rGO composite electrocatalyst is stable over long term OER operation.

In summary, in the present study ternary metal sulfide – carbon composite i.e. nickel manganese cobalt sulfide/ rGO is deposited in the form of thin film on SS substrate using SILAR method, for the application of electrocatalytic OER. For that, first of all thin film of cobalt sulfide is deposited and the effect of mass loading on electrochemical performance is studied. After that, the effect of composition of transition metals is studied in binary metal sulfide i.e. manganese cobalt sulfide. From which it is concluded that the stoichiometric tuning of transition metals is very important for optimum performance. Therefore, before depositing composite thin films, stoichiometry of ternary metals is also optimized (i.e. for nickel manganese cobalt sulfide). The optimum composition of ternary metal sulfide is further used to deposit composite thin films. In the composite of nickel manganese cobalt sulfide and reduced graphene oxide, loading of reduced graphene oxide is optimized.

5.2. Conclusions

In the present chapter, first of all, amorphous nickel-manganese-cobalt sulfide thin film electrocatalysts were synthesized by SILAR method (part A). The compositions of Ni, Mn and Co were optimized. At the optimum composition (Ni:Mn:Co -2:1:2), NMC-212 electrocatalyst possess sheet-like morphology and also minimum charge transfer resistance (R_{ct}). NMC-212 electrocatalysts requires 235 mV overpotential to reach 10 mA cm^{-2} current density. In part B of this chapter, the composite thin films of nickel-manganese-cobalt sulfide and reduced graphene oxide were deposited by SILAR method. For this, the experimental conditions of previously optimized NMC-212 electrocatalyst was carry forwarded. In this part, the quantity of rGO in composite electrocatalysts was optimized by changing the number of rGO cycles. The NMC/rGO-20 composite electrocatalyst shows excellent electrocatalytic OER performance. It requires 230 mV overpotential to reach 10 mA cm^{-2} current density along with to reach a high current density of 100 mA cm^{-2} , it only requires 291 mV overpotential.

5.3 References

- [1] N. T. Suen, S. F. Hung, Q. Quan, N. Zhang, Y. J. Xu, H. M. Chen, Electrocatalysis for the oxygen evolution reaction: Recent development and future perspectives, *Chem. Soc. Rev.* 46 (2017) 337–365. <https://doi.org/10.1039/c6cs00328a>.
- [2] S. B. Kale, A. C. Lokhande, R. B. Pujari, C. D. Lokhande, Effect of pretreatment on catalytic activity of cobalt sulfide thin film for oxygen evolution reaction, *Mater. Lett.* 228 (2018) 418–420. <https://doi.org/10.1016/j.matlet.2018.06.035>.
- [3] B. Yu, G. Jiang, W. Xu, C. Cao, Y. Liu, N. Lei, U. Evariste, P. Ma, Construction of $\text{NiMoO}_4/\text{CoMoO}_4$ nanorod arrays wrapped by Ni-Co-S nanosheets on carbon cloth as high performance electrode for supercapacitor, *J. Alloys Compd.* 799 (2019) 415–424. <https://doi.org/https://doi.org/10.1016/j.jallcom.2019.05.353>.
- [4] S. Anantharaj, S. R. Ede, K. Sakthikumar, K. Karthick, S. Mishra, S. Kundu,

- Recent trends and perspectives in electrochemical water splitting with an emphasis on sulfide, selenide, and phosphide catalysts of Fe, Co, and Ni: A review, *ACS Catal.* **6** (2016) 8069–8097. <https://doi.org/10.1021/acscatal.6b02479>.
- [5] H. Jin, J. Wang, D. Su, Z. Wei, Z. Pang, Y. Wang, In situ cobalt–cobalt oxide/N-doped carbon hybrids as superior bifunctional electrocatalysts for hydrogen and oxygen evolution, *J. Am. Chem. Soc.* **137** (2015) 2688–2694. <https://doi.org/10.1021/ja5127165>.
- [6] H. Shi, G. Zhao, Water oxidation on spinel NiCo_2O_4 nanoneedles anode: microstructures, specific surface character, and the enhanced electrocatalytic performance, *J. Phys. Chem. C* **118** (2014) 25939–25946. <https://doi.org/10.1021/jp508977j>.
- [7] U. Evariste, G. Jiang, B. Yu, Y. Liu, P. Ma, Electrodeposition of manganese-nickel-cobalt sulfides on reduced graphene oxide/nickel foam for high-performance asymmetric supercapacitors, *J. Electron. Mater.* **49** (2020) 922–930. <https://doi.org/10.1007/s11664-019-07810-6>.
- [8] X. Ge, Y. Liu, F. W. T. Goh, T. S. A. Hor, Y. Zong, P. Xiao, Z. Zhang, S. H. Lim, B. Li, X. Wang, Z. Liu, Dual-phase spinel MnCo_2O_4 and spinel MnCo_2O_4 /nanocarbon hybrids for electrocatalytic oxygen reduction and evolution, *ACS Appl. Mater. Interfaces* **6** (2014) 12684–12691. <https://doi.org/10.1021/am502675c>.
- [9] Z. Dai, H. Geng, J. Wang, Y. Luo, B. Li, Y. Zong, J. Yang, Y. Guo, Y. Zheng, X. Wang, Q. Yan, Hexagonal-phase cobalt monophosphosulfide for highly efficient overall water splitting, *ACS Nano* **11** (2017) 11031–11040. <https://doi.org/10.1021/acsnano.7b05050>.
- [10] M. Al-Mamun, Y. Wang, P. Liu, Y.L. Zhong, H. Yin, X. Su, H. Zhang, H. Yang, D. Wang, Z. Tang, H. Zhao, One-step solid phase synthesis of a highly efficient and robust cobalt pentlandite electrocatalyst for the oxygen evolution reaction, *J. Mater. Chem. A* **4** (2016) 18314–18321. <https://doi.org/10.1039/C6TA07962H>.
- [11] H. Li, S. Chen, Y. Zhang, Q. Zhang, Q. Zhang, X. Jia, L. Gu, X. Sun, L. Song, X. Wang, Systematic design of superhydrophobic nanotube-array electrode comprised of transition-metal sulfides for overall water splitting, *Nat. Commun.* **9** (2018) 2452 (1–12). <https://doi.org/10.1038/s41467-018-04888-0>.
- [12] X. Wang, Q. Zhang, J. Sun, Z. Zhou, Q. Li, B. He, J. Zhao, W. Lu, C. P. Wong, Y. Yao, Facile synthesis of hierarchical porous manganese nickel cobalt sulfide nanotube arrays with enhanced electrochemical performance for ultrahigh energy density fiber-shaped asymmetric supercapacitors, *J. Mater. Chem. A* **6** (2018) 8030–8038. <https://doi.org/10.1039/c8ta01440j>.
- [13] M. C. Biesinger, B. P. Payne, A. P. Grosvenor, L. W. M. Lau, A. R. Gerson, R. S. C. Smart, Resolving surface chemical states in XPS analysis of first row transition metals, oxides and hydroxides: Cr, Mn, Fe, Co and Ni, *Appl. Surf.*
-

- Sci. 257 (2011) 2717–2730. <https://doi.org/10.1016/j.apsusc.2010.10.051>.
- [14] X. Zhang, P. Yu, H. Zhang, D. Zhang, X. Sun, Y. Ma, Rapid hydrothermal synthesis of hierarchical nanostructures assembled from ultrathin birnessite-type MnO_2 nanosheets for supercapacitor applications, *Electrochim. Acta.* 89 (2013) 523–529. <https://doi.org/10.1016/j.electacta.2012.11.089>.
- [15] H. Chen, M. Q. Wang, Y. Yu, H. Liu, S. Y. Lu, S. J. Bao, M. Xu, Assembling Hollow cobalt sulfide nanocages array on graphene-like manganese dioxide nanosheets for superior electrochemical capacitors, *ACS Appl. Mater. Interfaces.* 9 (2017) 35040–35047. <https://doi.org/10.1021/acsami.7b12069>.
- [16] Y. J. Wei, L. Y. Yan, C. Z. Wang, X. G. Xu, F. Wu, G. Chen, Effects of Ni doping on $[\text{MnO}_6]$ octahedron in LiMn_2O_4 , *J. Phys. Chem. B.* 108 (2004) 18547–18551. <https://doi.org/10.1021/jp0479522>.
- [17] J. Zhao, J. Chen, S. Xu, M. Shao, Q. Zhang, F. Wei, J. Ma, M. Wei, D. G. Evans, X. Duan, Hierarchical NiMn layered double hydroxide/carbon nanotubes architecture with superb energy density for flexible supercapacitors, *Adv. Funct. Mater.* 24 (2014) 2938–2946. <https://doi.org/10.1002/adfm.201303638>.
- [18] M. E. Spahr, Characterization of layered lithium nickel manganese oxides synthesized by a novel oxidative coprecipitation method and their electrochemical performance as lithium insertion electrode materials, *J. Electrochem. Soc.* 145 (1998) 1113 (1–10). <https://doi.org/10.1149/1.1838425>.
- [19] B. Li, C. Li, J. Cai, J. Zhao, Retracted Article: In situ nano-coating on $\text{Li}_{1.2}\text{Mn}_{0.52}\text{Ni}_{0.13}\text{Co}_{0.13}\text{O}_2$ with a layered@spinel@coating layer heterostructure for lithium-ion batteries, *J. Mater. Chem. A.* 3 (2015) 21290–21297. <https://doi.org/10.1039/C5TA06387F>.
- [20] X. W. Lou, L.A. Archer, Z. Yang, Hollow micro-/nanostructures: synthesis and applications, *Adv. Mater.* 20 (2008) 3987–4019. <https://doi.org/10.1002/adma.200800854>.
- [21] Y. L. Zhang, L. Guo, H. Xia, Q. D. Chen, J. Feng, H. B. Sun, Photoreduction of graphene oxides: methods, properties, and applications, *Adv. Opt. Mater.* 2 (2014) 10–28. <https://doi.org/10.1002/adom.201300317>.
- [22] Y. Si, E. T. Samulski, Synthesis of water soluble graphene, *Nano Lett.* 8 (2008) 1679–1682. <https://doi.org/10.1021/nl080604h>.
- [23] I. Sengupta, S. Chakraborty, M. Talukdar, S. K. Pal, S. Chakraborty, Thermal reduction of graphene oxide: How temperature influences purity, *J. Mater. Res.* 33 (2018) 4113–4122. <https://doi.org/DOI: 10.1557/jmr.2018.338>.
- [24] C. K. Chua, M. Pumera, Chemical reduction of graphene oxide: a synthetic chemistry viewpoint, *Chem. Soc. Rev.* 43 (2014) 291–312. <https://doi.org/10.1039/C3CS60303B>.
- [25] M. M. Lucchese, F. Stavale, E. H. M. Ferreira, C. Vilani, M. V. O. Moutinho, R.

- B. Capaz, C. A. Achete, A. Jorio, Quantifying ion-induced defects and Raman relaxation length in graphene, *Carbon* N. Y. 48 (2010) 1592–1597. <https://doi.org/https://doi.org/10.1016/j.carbon.2009.12.057>.
- [26] M. K. Rabchinskii, A. T. Dideikin, D. A. Kirilenko, M. V Baidakova, V. V Shnitov, F. Roth, S. V Konyakhin, N. A. Besedina, S. I. Pavlov, R. A. Kuricyn, N. M. Lebedeva, P. N. Brunkov, A. Y. Vul', Facile reduction of graphene oxide suspensions and films using glass wafers, *Sci. Rep.* 8 (2018) 14154 (1-11). <https://doi.org/10.1038/s41598-018-32488-x>.
- [27] Y. Deng, Y. Xie, K. Zou, X. Ji, Review on recent advances in nitrogen-doped carbons: preparations and applications in supercapacitors, *J. Mater. Chem. A*. 4 (2016) 1144–1173. <https://doi.org/10.1039/C5TA08620E>.

CHAPTER 6

Conclusions and future work

The electrochemical water splitting or electrolysis of water is the most feasible hydrogen production method at the time being. Among the hydrogen evolution reaction (HER) and oxygen evolution reaction (OER), OER is sluggish and complicated because it demands high overpotential which affects the overall water splitting. For this reason, the present study is focused upon the development and characterization of novel transition metal sulfide materials by successive ionic layer adsorption and reaction (SILAR) route for application as OER electrocatalyst in water splitting.

Herein, **Chapter 1** presents an introduction to electrochemical water splitting and a literature survey of transition metal-based (especially cobalt, manganese and nickel) materials that have been investigated earlier. There clearly existed a research gap indicating an immediate urge to investigate ternary metal sulfide materials and their composites with 3D carbon structures, specifically nickel manganese cobalt sulfide composited with reduced graphene oxides (rGO), for OER applications.

With this objective, **Chapter 2** presents the theoretical background and experimental details of the thin film synthesis using SILAR method. Among the liquid phase chemical deposition methods, SILAR is a simple yet scalable method for the deposition of chalcogenide thin films. In details, the SILAR method comprises four steps, namely: adsorption, 1st rinsing, reaction, and 2nd rinsing, which is collectively defined as one SILAR deposition cycle. In order to enlighten the various physical properties, synthesized thin films can be characterized by various physical characterization techniques. For a better understanding of results obtained from these techniques, their basic principles and working mechanisms have been studied in chapter 2. Similarly, the theory behind electrochemical techniques used to evaluate electrocatalytic OER performance was also studied in chapter 2.

Since the film thickness or mass loading of the electrocatalyst significantly affects the OER performance, optimization of film thickness or mass loading is necessary. The film thickness or mass loading of the deposited material in SILAR method can be varied by simply changing the number of deposition cycles.

In this regard, **Chapter 3** presents the study of the effect of mass loading on the physicochemical properties and OER performance of cobalt sulfide electrocatalyst. The mass loading of active material was found to significantly change with the number of SILAR deposition cycles and influenced the surface morphology of the thin film. As an impact of change in morphology, CS-80 (deposited at 80 SILAR cycles) with mass loading 3.71 mg cm^{-2} , exhibited an efficient OER performance with 275 mV overpotential at 10 mA cm^{-2} and Tafel slope 53 mV dec^{-1} . The porous surface is evidenced as the main reasons for high ECSA (1750 cm^2) and low R_{ct} values (1.52Ω) which possibly enhanced the OER performance. This chapter highlights the importance of optimization of mass loading in the field of electrocatalytic OER. Yet, there existed the possibility for further improving the OER performance of the cobalt sulfide thin films by the partial substitution of cobalt with manganese to tune the overall electronegativity and electronic structure of the material favorable to OER.

Chapter 4 demonstrates the compositional tuning of manganese cobalt sulfide thin film electrocatalysts. Impressively, when used for water oxidation, the amorphous $(\text{Co}_3\text{Mn}_2)\text{S}$ thin film electrocatalyst exhibited superior performance with excellent stability for 48 hours in an alkaline medium. Indeed, the electrocatalyst reached a benchmarking 10 mA cm^{-2} current density with an overpotential as low as 243 mV. While probing the origin of optimal performance, it was found that the stoichiometric tuning of composition has possibly influenced the redox chemical properties of the electrocatalyst significantly and modified their bonding strengths

with the intermediates. The atomic randomness of electrocatalyst provided abundant active sites tailored into sheet-like morphology and furnished with the multiple oxidation states of the transition metal atoms. As a result, maximum active sites are exposed to the electrolyte with an improved electrocatalytic activity that uplifted the overall performance.

Moreover, the investigation indicated an opportunity to further enhance the OER performance of the material by incorporating another transition metal atom, e.g., nickel to improve the electrocatalytic activity as a result of the synergistic and cumulative effect of multi-metals. Therefore, **Chapter 5 (Part A)** presents the synthesis and compositional optimizations of nickel manganese cobalt sulfide thin film electrocatalysts. At the optimum composition i.e. NMC-212 (ratio of Ni:Mn:Co = 2:1:2), the electrocatalyst presented a sheet-like morphology and also a minimum charge transfer resistance ($R_{ct} = 0.35 \Omega$). Given this, the electrocatalysts required an overpotential of 235 mV to reach a current density of 10 mA cm^{-2} .

To enhance the charge and mass transport efficiency, the coupling of transition metal sulfides with three dimensional conductive nanocarbon supports such as reduced graphene oxide (rGO) is a most efficient strategy. Therefore, in **Chapter 5 (Part B)**, the composite thin films of nickel manganese cobalt sulfide and reduced graphene oxide (rGO) were synthesized. For this, the experimental conditions of previously optimized NMC-212 electrocatalyst were carry forwarded and the quantity of rGO in composite electrocatalysts was optimized by changing the number of rGO cycles. Impressively, the NMC/rGO-20 composite electrocatalyst showed excellent electrocatalytic OER performance. It required a notably low, 230 mV overpotential to reach 10 mA cm^{-2} current density and demonstrated a Tafel slope as low as 50 mV dec^{-1} . Additionally, the electrocatalyst exhibited high current density (over 250 mA

cm^{-2}) at a potential of 1.6 V (vs. RHE). The significantly high OER performance was found to be facilitated by the optimum atomic stoichiometry, high electrochemically active surface area, improved electronic structures and better electronic conductivity. This part highlights the importance of controlling the amount of rGO during the synthesis of composite materials.

Nickel manganese cobalt sulfide/ rGO composite thin film electrocatalyst requires low overpotential to reach 10 mA cm^{-2} current density as compared to single and binary Ni, Mn and Co containing sulfides as seen in Figure 6.1.

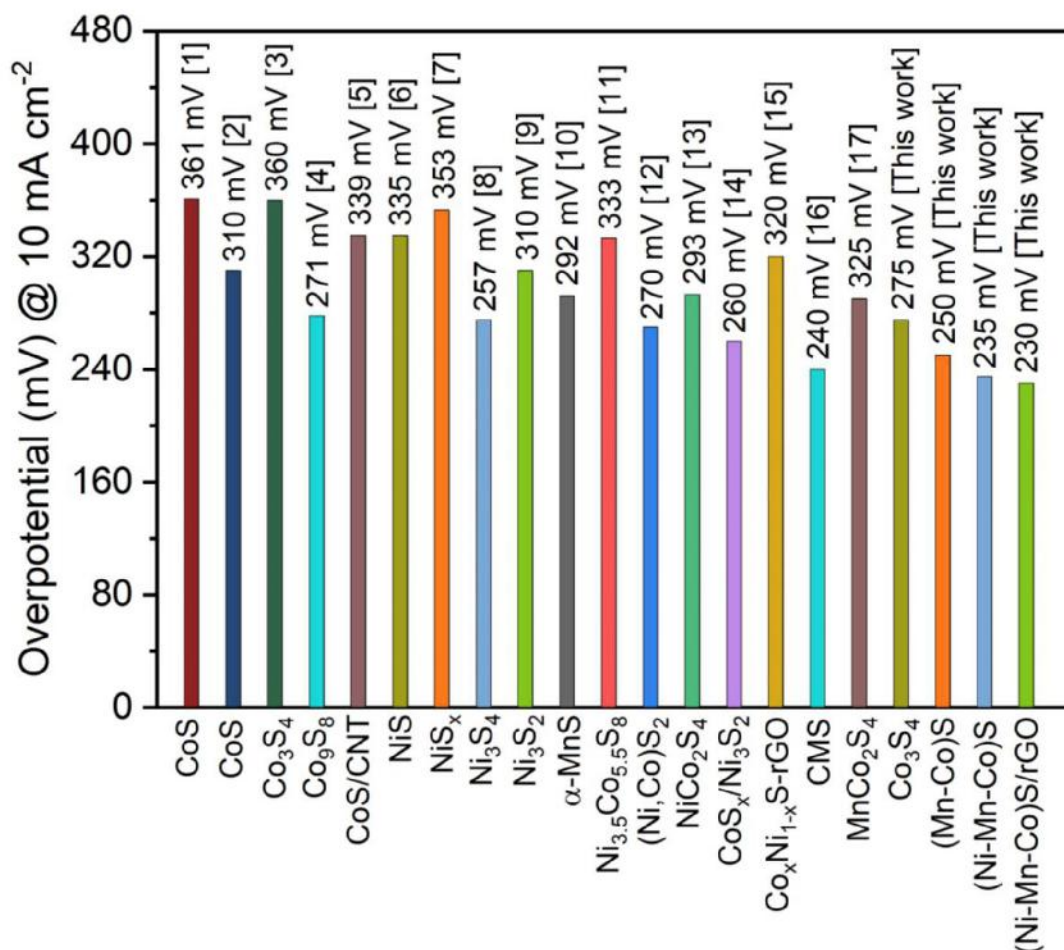


Figure 6.1: Comparison of the overpotential of thin film electrocatalysts obtained in the present study with overpotentials of cobalt, nickel and manganese containing single, binary and ternary sulfides reported in the literature.

The Comparative summary of thin film electrodes deposited by SILAR method for the application of electrocatalytic OER in the present study is given in table 6.1.

Table 6.1: Comparative summary of thin film electrodes deposited by SILAR method for the application of electrocatalytic OER in the present study.

Sample	Class of Material	Nature of Material	Overpotential (η) (mV) @10 mA cm ⁻²	Remark
Cobalt sulfide	Single metal sulfide	Crystalline	275	<ul style="list-style-type: none"> Effect of mass loading on electrochemical performance is studied. Mass loading is varied by changing number of SILAR cycles.
Manganese cobalt sulfide	Binary metal sulfide	Amorphous	250	<ul style="list-style-type: none"> Effect of the stoichiometry of transition metals on electrochemical performance is studied. Optimum performance is obtained at optimum stoichiometry.
Nickel manganese cobalt sulfide	Ternary metal sulfide	Amorphous	235	<ul style="list-style-type: none"> With reference to binary metal sulfide, stoichiometry is optimized to get optimum performance.
			280*	
			311 [‡]	
Nickel manganese cobalt sulfide / reduced graphene oxide	Ternary metal sulfide – Carbon composite	Amorphous	230	<ul style="list-style-type: none"> Previously optimized composition of ternary metal sulfide is used to deposit composite thin film. Graphene oxide is thermally reduced Effect of the amount of reduced graphene oxide on electrochemical performance is studied.
			268*	
			291 [‡]	

* - @ 50 mA cm⁻²; ‡ - @ 100 mA cm⁻²

The possible reasons for good electrochemical performance of nickel manganese cobalt sulfide/rGO composite thin films are as follow:

- 1) Amorphous nature of catalyst provides abundant defects that act as active catalytic sites.
- 2) Self-supported architecture in the form of thin film deposited on conducting backbone avoids the resistance due to the binding agents used while casting a powder catalyst on a substrate.

3) Composite of transition metal sulfides with reduced graphene oxide gives a synergistic effect of enhanced electronic conductivity.

4) The metal atoms in the transition metal sulfide based electrocatalysts usually present the active catalytic sites, therefore, the coupling of more than one transition metal in the present electrocatalyst has possibly enhanced the electrochemical performance.

In the present study, a system of ternary transition metal sulfide and its composite with a highly conducting carbon structure (rGO) was systematically optimized for electrocatalytic OER by controlled experiments. Despite this work, there is a lot of work one can do to further improve the OER performance as well as to enlighten the various aspects of electrocatalysts. Heteroatoms such as S and N doped rGO can be used instead of rGO. Also, zero-dimensional (0D) fullerene or one-dimensional (1D) carbon nanotubes (CNT) can be used instead of two-dimensional (2D) rGO sheets to enhance the performance of ternary transition metal sulfide. In the present study and also in other numerous reports the basis of OER performance of electrocatalysts is evaluated/concluded based on their physical properties such as phase, microstructures, hydrophilicity, etc. These properties are also important but at this point, extensive theoretical studies are also required. Particularly, one can uncover the original OER reaction mechanism and reaction rate using density functional theory (DFT) which is one of the effective ways to predict the molecular level theory of electrocatalysis. Along with theoretical studies, electrocatalyst can be characterized through high-end characterization techniques such as X-ray absorption fine structure (XAFS) and X-ray absorption near edge structure (XANES) to measure active sites.

References

- [1] T. Liu, Y. Liang, Q. Liu, X. Sun, Y. He, A. M. Asiri, Electrodeposition of cobalt-sulfide nanosheets film as an efficient electrocatalyst for oxygen evolution reaction, *Electrochem. Commun.* 60 (2015) 92–96. <https://doi.org/10.1016/j.elecom.2015.08.011>.
- [2] K. Nan, H. Du, L. Su, C.M. Li, Directly electrodeposited cobalt sulfide nanosheets as advanced catalyst for oxygen evolution reaction, *Chemistry Select.* 3 (2018) 7081–7088. <https://doi.org/10.1002/slct.201801482>.
- [3] M. Zhu, Z. Zhang, H. Zhang, H. Zhang, X. Zhang, L. Zhang, S. Wang, Hydrophilic cobalt sulfide nanosheets as a bifunctional catalyst for oxygen and hydrogen evolution in electrolysis of alkaline aqueous solution, *J. Colloid Interface Sci.* 509 (2018) 522–528. <https://doi.org/10.1016/j.jcis.2017.09.076>.
- [4] H. Liu, F. X. Ma, C. Y. Xu, L. Yang, Y. Du, P. P. Wang, S. Yang, L. Zhen, Sulfurizing-induced hollowing of Co₉S₈ microplates with nanosheet units for highly efficient water oxidation, *ACS Appl. Mater. Interfaces.* 9 (2017) 11634–11641. <https://doi.org/10.1021/acsami.7b00899>.
- [5] K. Prabakaran, M. Lokanathan, B. Kakade, Three dimensional flower like cobalt sulfide (CoS)/functionalized MWCNT composite catalyst for efficient oxygen evolution reactions, *Appl. Surf. Sci.* 466 (2019) 830–836. <https://doi.org/https://doi.org/10.1016/j.apsusc.2018.10.015>.
- [6] W. Zhu, X. Yue, W. Zhang, S. Yu, Y. Zhang, J. Wang, J. Wang, Nickel sulfide microsphere film on Ni foam as an efficient bifunctional electrocatalyst for overall water splitting, *Chem. Commun.* 52 (2016) 1486–1489. <https://doi.org/10.1039/C5CC08064A>.
- [7] H. Li, Y. Shao, Y. Su, Y. Gao, X. Wang, Vapor-phase atomic layer deposition of nickel sulfide and its application for efficient oxygen-evolution electrocatalysis, *Chem. Mater.* 28 (2016) 1155–1164. <https://doi.org/10.1021/acs.chemmater.5b04645>.
- [8] K. Wan, J. Luo, C. Zhou, T. Zhang, J. Arbiol, X. Lu, B. W. Mao, X. Zhang, J. Fransaer, Hierarchical porous Ni₃S₄ with enriched high-valence Ni sites as a robust electrocatalyst for efficient oxygen evolution reaction, *Adv. Funct. Mater.* 29 (2019) 1900315 (1–8). <https://doi.org/10.1002/adfm.201900315>.
- [9] N. K. Chaudhari, A. Oh, Y. J. Sa, H. Jin, H. Baik, S. G. Kim, S. J. Lee, S. H. Joo, K. Lee, Morphology controlled synthesis of 2-D Ni–Ni₃S₂ and Ni₃S₂ nanostructures on Ni foam towards oxygen evolution reaction, *Nano Converg.* 4 (2017) 7 (1–9). <https://doi.org/10.1186/s40580-017-0101-6>.
- [10] R. B. Pujari, G. S. Gund, S. J. Patil, H. S. Park, D. W. Lee, Anion-exchange phase control of manganese sulfide for oxygen evolution reaction, *J. Mater. Chem. A.* 8 (2020) 3901–3909. <https://doi.org/10.1039/c9ta10553k>.
- [11] V. Ganesan, P. Ramasamy, J. Kim, Hierarchical Ni_{3.5}Co_{0.5}S₈ nanosheet-

- assembled hollow nanocages: Superior electrocatalyst towards oxygen evolution reaction, *Int. J. Hydrogen Energy*. 42 (2017) 5985–5992. <https://doi.org/https://doi.org/10.1016/j.ijhydene.2016.12.060>.
- [12] J. Zhang, X. Bai, T. Wang, W. Xiao, P. Xi, J. Wang, D. Gao, J. Wang, Bimetallic nickel cobalt sulfide as efficient electrocatalyst for Zn–air battery and water splitting, *Nano-Micro Lett.* 11 (2019) 2 (1–13). <https://doi.org/10.1007/s40820-018-0232-2>.
- [13] C. Zecquinc, S. Bhoyate, K. Siam, P. K. Kahol, N. Kostoglou, C. Mitterer, S. J. Hinder, M. A. Baker, G. Constantinides, C. Rebholz, G. Gupta, X. Li, R. K. Gupta, Needle grass array of nanostructured nickel cobalt sulfide electrode for clean energy generation, *Surf. Coatings Technol.* 354 (2018) 306–312. <https://doi.org/https://doi.org/10.1016/j.surfcoat.2018.09.045>.
- [14] S. Shit, S. Chhetri, W. Jang, N. C. Murmu, H. Koo, P. Samanta, T. Kuila, Cobalt sulfide/nickel sulfide heterostructure directly grown on nickel foam: an efficient and durable electrocatalyst for overall water splitting application, *ACS Appl. Mater. Interfaces*. 10 (2018) 27712–27722. <https://doi.org/10.1021/acsami.8b04223>.
- [15] Y. R. Hong, S. Mhin, K. M. Kim, W. S. Han, H. Choi, G. Ali, K. Y. Chung, H. J. Lee, S. I. Moon, S. Dutta, S. Sun, Y. G. Jung, T. Song, H. S. Han, Electrochemically activated cobalt nickel sulfide for an efficient oxygen evolution reaction: Partial amorphization and phase control, *J. Mater. Chem. A*. 7 (2019) 3592–3602. <https://doi.org/10.1039/c8ta10142f>.
- [16] J. Li, W. Xu, J. Luo, D. Zhou, D. Zhang, L. Wei, P. Xu, D. Yuan, Synthesis of 3D hexagram-like cobalt–manganese sulfides nanosheets grown on nickel foam: A bifunctional electrocatalyst for overall water splitting, *Nano-Micro Lett.* 10 (2017) 6 (1–10). <https://doi.org/10.1007/s40820-017-0160-6>.
- [17] X. Zhang, C. Si, X. Guo, R. Kong, F. Qu, A MnCo_2S_4 nanowire array as an earth-abundant electrocatalyst for an efficient oxygen evolution reaction under alkaline conditions, *J. Mater. Chem. A*. 5 (2017) 17211–17215. <https://doi.org/10.1039/c7ta04804a>.